



universität
wien

MAGISTERARBEIT

Titel der Magisterarbeit

„Herschel Imaging Photometry of Carbon Stars“

Verfasser

Bakk.rer.nat. Marko Mečina

angestrebter akademischer Grad

Magister der Naturwissenschaften (Mag.rer.nat.)

Wien, 2012

Studienkennzahl lt. Studienblatt:

A 066 861

Studienrichtung lt. Studienblatt:

Astronomie

Betreuer:

ao. Univ.-Prof. Dr. Franz Kerschbaum

Zusammenfassung

Sterne mit geringen bis mittleren Massen ($\sim 0.8\text{--}8 M_{\odot}$) finden sich früher oder später am *Asymptotischen Riesenast* (AGB – Asymptotic Giant Branch) im *Hertzsprung-Russell Diagramm* ein. Charakteristisch für Sterne in diesem Entwicklungsabschnitt ist ein kontrahierender Kern, bestehend aus Kohlenstoff und Sauerstoff, umhüllt von Helium und Wasserstoff verbrennenden Schalen. Aufgrund des, im Vergleich zur Hauptreihe, stark vergrößerten Radius (bis zu mehrere hundert Sonnenradien) und somit einer enormen Oberfläche ist auch die Leuchtkraft immens – einige $10^4 L_{\odot}$ können erreicht werden. Durch die Expansion kühlt der Stern auch ab, was ihm seine prägnante rötliche Färbung verleiht.

Während der Entwicklung auf dem Asymptotischen Riesenast werden die äußeren Schichten instabil und thermische Pulsationen setzen ein. Durch konvektive Ströme können Produkte der Nukleosynthese (Fusion und s-Prozess) aus tieferen Schichten in die Atmosphäre gelangen. Die Anreicherung schwererer Elemente an der Oberfläche, mit ^{12}C als wichtigster Komponente, kann, unter entsprechenden Rahmenbedingungen, einen ursprünglich sauerstoffreichen M-Stern zuerst in einen S-Stern und schließlich einen kohlenstoffreichen C-Stern verwandeln.

Die vergleichsweise niedrigen Temperaturen in der Sternatmosphäre erlauben die Bildung von Molekülen – abhängig vom Spektraltyp können unterschiedliche Zusammensetzungen beobachtet werden. Während sich in M-Sternen in erster Linie Metalloxide formieren, sind in C-Sternen diverse Kohlenstoffverbindungen zu finden. In S-Klasse Objekten wiederum treten, wegen der wenigen frei verfügbaren O und C Atome, Bindungen seltenerer Elemente, wie z.B. Zirkonium, in den Vordergrund. In den äußeren, kühlen Regionen können die Moleküle schließlich zu makroskopischen Partikeln – Staub – kondensieren. Entsprechend der vorherrschenden chemischen Verhältnisse bildet sich eine Hülle aus Silikaten oder diversen Formen von Kohlenstoff (z.B. amorph, Graphit). In Anbetracht der Tatsache, dass Sterne, die die AGB Phase durchleben, schließlich als Weiße Zwerge mit Massen von typischerweise $0.5\text{--}0.8 M_{\odot}$ enden, ist ersichtlich, dass diese Objekte einen Großteil der Materie im Laufe ihres Entwicklungsweges verlieren müssen. Der bei weitem überwiegende Teil dieses Verlusts findet am AGB statt. Der dafür notwendige stellare Wind wird durch den Staub, der sehr effektiv an das Strahlungsfeld koppelt, getrieben. Da über 90 % aller Sterne die AGB Phase durchleben, trägt der Massenverlust dieser Objekte beträchtlich zur Anreicherung des interstellaren Mediums mit schweren Elementen bei. Für ein umfassendes Bild des kosmischen Materiekreislaufs ist daher detailliertes Wissen um die Eigenschaften des Massenverlustes wesentlich.

Der kalte zirkumstellare Staub, der im Fokus dieser Magisterarbeit steht, wird auf Grund seines Emissionsmaximums im fernen infraroten Spektralbereich primär mit Weltraumsatelliten beobachtet. Bisherige erfolgreiche Missionen waren u.a. *IRAS*, *ISO* und *Spitzer*. Als neuestes und bisher größtes Weltraumteleskop versieht derzeit *Herschel* seinen Dienst. Im Rahmen des internationalen Projektes *MESS* (Mass-loss of Evolved

StarS) wurden unter anderem zahlreiche Sterne im AGB Stadium sowohl photometrisch als auch spektroskopisch beobachtet. Aus diesem Sample wurden im Rahmen der vorliegenden Arbeit photometrische Daten der beiden Kohlenstoffsterne TT Cygni und UX Draconis – aufgenommen vom Instrument *PACS* (Photodetector Array Camera and Spectrometer) bei $70\ \mu\text{m}$ und $160\ \mu\text{m}$ Wellenlänge – analysiert und interpretiert. Zusätzlich wurden mit dem Fortran-Code *DUSTY* Modelle aus Strahlungstransportrechnungen erstellt und mit den Beobachtungsdaten verglichen, um Eigenschaften des Massenverlustprozesses abzuschätzen.

Rund um TT Cyg wurde eine geometrisch dünne, zu einem hohen Grad sphärisch symmetrische Hülle aus kaltem Staub detektiert, die räumlich gut mit Beobachtungen der Gaskomponente im (Sub)millimeter- und Radiobereich übereinstimmt. Im Gegensatz dazu enthüllen die Daten von UX Dra eine unregelmäßige, bisher unbekannte Struktur aus Staub, ohne Pendant in anderen Spektralbereichen.

Abstract

For low to intermediate-mass stars ($\sim 0.8\text{--}8 M_{\odot}$) the time they spend on the *asymptotic giant branch* (AGB) in the *Hertzsprung-Russell Diagram*, although it is very short compared to the rest of their life-time, is one of dramatic changes. After ascending the red giant branch and passing the horizontal branch, the stellar core consists of carbon and oxygen, while hydrogen and helium are burnt in shells. The luminosity in this phase is enormous, reaching up to some $10^4 L_{\odot}$, due to the drastically increased radius (some hundreds of solar radii) and hence huge surface. Another consequence of the expansion is the decreased temperature and thus a characteristic reddish colour.

As an AGB star progresses on its evolutionary path the layers above the burning shell become thermally unstable and pulses occur. During this phase heavier elements produced by nucleosynthesis (fusion and slow neutron capture) are dredged up to the surface by convective cells. As a consequence, the chemical composition of the stellar atmosphere is altered, with ^{12}C being the most important component. A star that was initially of spectral type M, evolves (in a certain mass range) into an S-type star first, and eventually becomes a C-star.

Due to the relatively low temperatures in an AGB star's atmosphere molecules can form. Depending on the spectral type, different bonds can be observed. In M-stars metal oxides are dominant, whereas in C-stars carbonaceous species are found. In S-type stars most of the oxygen and carbon is bound in CO molecules, hence molecules bearing less abundant elements (e.g. zirconium) are then prominently visible in spectra. Eventually, in the cool outer layers of the stellar atmosphere, the temperature and density allow the molecules to condense to solid particles out of the gas phase. Corresponding to the prevailing chemistry, either silicates or carbon grains (e.g. amorphous structure, graphitic grains) are formed. Given the fact that AGB stars end up as white dwarfs with masses in the range of $0.5\text{--}0.8 M_{\odot}$, they have to lose major fractions of their matter. Most of this mass-loss takes place in the late stages of the AGB phase. Dust plays a crucial role in this process, as it acts as a driver that picks up momentum from the stellar radiation field and transfers it to the gas, which is the dominant state of the matter.

Since more than 90 % of the stars become AGB objects, their dusty winds contribute significantly to the enrichment of the interstellar medium with processed heavy elements. Thus, it is of great importance for the understanding of the cosmic matter cycle to comprehend the mechanisms at work in these objects.

This thesis focuses on the cold circumstellar dust that is ejected by the slow winds. Since its emission peaks in the far infrared, observations of this component are restricted to space-borne telescopes. Past missions were, for example, *IRAS*, *ISO* and *Spitzer*. Currently, the *Herschel* satellite is delivering data with unprecedented spatial resolution and sensitivity. In the course of the *MESS* (Mass-loss of Evolved StarS) program a representative sample of AGB objects was observed, both spectroscopically and photometrically. For this thesis photometric data of the two carbon stars TT Cygni and

UX Draconis, obtained with the Photodetector Array Camera and Spectrometer (*PACS*) at wavelengths of $70\ \mu\text{m}$ and $160\ \mu\text{m}$, were investigated. The photometric measurements were used to derive basic parameters of the circumstellar structures. Additionally, radiative transfer calculations were carried out using the radiative transfer code *DUSTY*, in order to estimate properties of the mass-loss process.

For TT Cyg a geometrically thin and remarkably spherically symmetric detached dust shell was detected. A co-spatial gas equivalent was already found in previous sub-mm observations. Around UX Dra a previously unobserved structure was identified – its formation scenario, however, remains unclear.

Contents

1	AGB Stars	9
1.1	The Role of AGB Stars	9
1.1.1	AGB Stars in the Cosmic Matter Cycle	9
1.1.2	AGB Stars in Stellar Systems	10
1.2	Physics of AGB Stars	12
1.2.1	Stellar Evolution to and on the AGB	12
1.2.2	Carbon Stars	19
1.2.3	Dust in Circumstellar Environments	21
1.2.4	Mass-loss through Stellar Winds	22
1.2.5	Circumstellar Envelopes (CSEs)	25
1.3	Observing Dusty Objects	26
2	The MESS Project	29
2.1	MESS	29
2.2	The Herschel Space Observatory	30
2.3	The Photodetector Array Camera and Spectrometer (PACS)	32
2.3.1	Instrument Setup	32
2.3.2	Observing Modes	34
2.3.3	Photometer Performance	35
2.4	From Raw Data to the Final Map	38
2.4.1	Calibration of the Dataset	39
2.4.2	Mapping Techniques	45
3	Analysis & Modelling	55
3.1	Measuring CSEs	55
3.1.1	Profiles – Condensed Information	55
3.1.2	Basic Shell Figures	58
3.1.3	Photometry	61
3.2	Modelling Circumstellar Shells – The DUSTY Code	63
3.2.1	Input Parameters	65
3.2.2	Modelling Output	68
3.2.3	Models & Observations	74
4	Dust Shells Around Evolved Stars	79
4.1	TT Cygni & UX Draconis – A Well Known and a New One	79
4.1.1	TT Cygni	79
4.1.2	UX Draconis	86
4.2	Conclusion & Prospects	92

Bibliography	93
A HIPE & Python Scripts	99
A.1 Adapted PACS Pipeline	99
A.2 Create a Radial Profile	101
A.3 Compare DUSTY Model to Observation	106

Chapter 1

AGB Stars

It must have been in the earliest times of stargazing when AGB stars, back then without knowledge about the complex physical background, of course, were recognised as peculiar among the vast number of visible stars on the night sky. Their typical reddish colour sets them apart from the majority of main sequence objects and is in strong contrast to the blueish ones. In the late nineteenth century, it became clear that the different colours are tied to the stellar temperature, eventually with Max Planck formulating the correct quantitative description. Another phenomenon – variability – drew attention on a star, today known as *Mira*. In 1596 the astronomer Fabricius observed its disappearance, whereupon 42 years later Dutchman Holwarda noticed that it had reappeared and consequently recognised a reoccurring pattern. Peculiarities in the spectra of several stars were found by Father Secchi at the Vatican Observatory in the 19th century (Secchi 1868) – the discovery of carbon stars.

In modern astronomy a consistent description of AGB stars was, and in detail still is, a puzzling piece of work. One of the first milestones was a paper by Iben & Renzini (1983), which constitutes a first consensus about the processes taking place in AGB stars. Despite the fact it was published almost three decades ago, most of it still remains valid. Further prominent work was done by Vassiliadis & Wood (1993), who present evolutionary models and Habing (1996), who focuses his review on the properties of the circumstellar environment. Considering more current work, a very comprehensive overview of the field of AGB star research is given by Habing & Olofsson (2004), where several authors recapitulate the state of the art in their respective area of expertise. In another recent review by Herwig (2005) AGB star evolution is discussed. Based upon these landmark publications (if not cited otherwise), this introductory chapter presents some fundamental aspects of the nature of AGB stars.

1.1 The Role of AGB Stars

1.1.1 AGB Stars in the Cosmic Matter Cycle

Compared to the whole lifetime of low to intermediate mass stars the AGB phase is very short. Typically, the timespan they spend on the AGB is less than 1% of that on the main sequence for the lower mass stars, or slightly above for the more massive ones (see model predictions in Vassiliadis & Wood 1993). Also, there is a slight dependence on the metallicity. Nevertheless we can observe quite a number of objects during this evolutionary stage. This can be explained by the fact that the vast majority of all stars experiences the AGB phase at some point. Considering the distribution of stellar masses

in a system, described by the initial mass function (IMF) according to Salpeter (1955):

$$n(M) \propto M^{-2.35},$$

this is the case for more than 90% of the stars leaving the main sequence.

Moving onward the evolutionary track, after going through the post-AGB phase and in many cases becoming a colourful planetary nebula, the stars' evolution comes to an end at the white dwarf stage, where the final masses of the stellar remains are about $0.5\text{--}0.8 M_{\odot}$. Given the initial mass range of $\sim 0.8\text{--}8 M_{\odot}$, this means that these stars – especially the more massive ones – eject a large fraction of their matter, returning it to the interstellar medium as part of the cosmic matter cycle. Consequently, AGB stars contribute significantly to the chemical enrichment of the ISM by injecting carbon and heavier elements from nuclear processing and particularly molecules (CO, H₂O, etc.) and dust grains (silicates and amorphous carbon) formed in the atmosphere and outer layers of the circumstellar environment. As shown in Fig. 1.1 AGB stars of the different spectral classes (M, S and C) are the most “productive” sources of interstellar gas and dust. While the fractional input of gas is already large, their role concerning the dust contribution is even more important. Hence it is essential to comprehend the processes occurring on the AGB in order to understand not only the chemical evolution of galaxies but also the cosmic cycle of matter as a whole.

1.1.2 AGB Stars in Stellar Systems

AGB stars are also of special interest if one is examining stellar systems, both in the Milky Way (e.g. globular clusters) and the extragalactic realm. This is because of several reasons. Particularly in extragalactic studies their enormous luminosity is advantageous, reaching up to $30\,000 L_{\odot}$ (Habing & Olofsson 2004), which is almost ten times the brightness of the tip of the red giant branch (RGB). This makes them the most luminous objects in their stellar aggregation, except for the even brighter, very rare supergiants. Thus they can be studied rather well throughout the Milky Way and can also be detected individually even in remote extragalactic environments.

As already mentioned the time stars spend on the AGB is short ($10^6\text{--}10^7$ years), depending on their mass. They have a well defined age and can serve as good tracers of the intermediate-age population (1–10 Gyr) and help reconstructing the star formation history of a stellar system. The ages can be estimated by looking at the most luminous AGB stars: the brighter (i.e. more massive) the stars on the AGB are, the younger the population. While their scarce occurrence can be cumbersome when studying stellar populations, it comes in handy when examining high density environments such as cores of globular clusters. Due to their rareness and pronounced IR emission crowding is not an issue when observing at appropriate wavelengths. Moreover, the fact that AGB stars emit their light mostly in the near-IR, means that observations do not suffer severely from interstellar extinction. Hence with their help sites can be probed, where main sequence stars are dimmed below recognition.

Stars on the asymptotic giant branch also exhibit distinct photometric variability (especially in the visible) and can usually be classified as long period variables (LPVs) of either Mira or semiregular type (SRa, SRb). Particularly Miras show an articulate

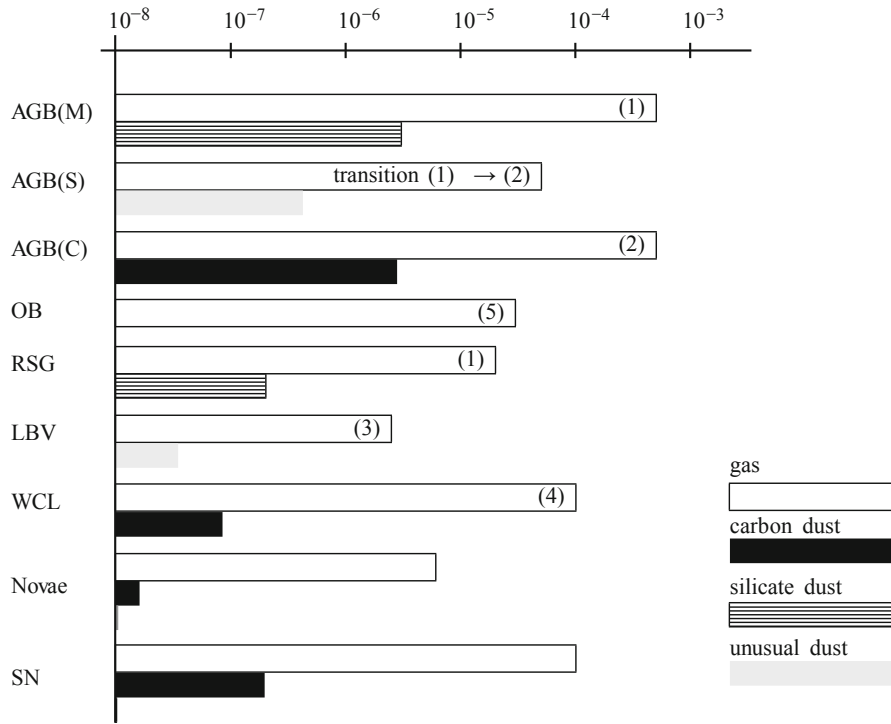


Figure 1.1: Return rates ($M_{\odot} \text{ kpc}^{-2} \text{ a}^{-1}$) of gas and dust to the interstellar medium by the various types of stars. The produced dust is mainly of either carbonaceous or silicate type. In some cases (primarily S-type AGBs) iron or iron alloys and material consisting of less abundant elements are formed. The used abbreviations are: AGB = asymptotic giant branch stars (of M, S and C spectral type), OB = massive stars on the upper main sequence, RSG = red supergiants, LBV = luminous blue variables, WCL = Wolf-Rayet stars of spectral type WC8-11, SN = supernovae. Plot taken from Gail (2010).

period-luminosity relation, thus being a useful tool for distance estimates. AGB stars can be discerned at large distances, their observable influence, however, does not end where they cannot be individually resolved anymore. For example, there are molecular signatures in the spectra of star clusters that can be ascribed to them. Also, spectral energy distributions (SEDs) are considerably affected by the contribution of dusty envelopes, commonly found around AGB stars, causing a far-IR excess.

In conclusion, these manifold implications certainly justify a comprehensive study of AGB stars and further demonstrate that efforts for a better understanding of the mechanisms at work in these objects are not mere “l’art pour l’art”.

1.2 Physics of AGB Stars

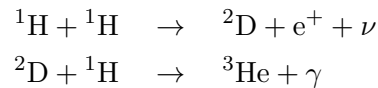
Over their lifetime, low to intermediate mass stars experience a number of phenomena with a wealth of sometimes rather complex astrophysical processes taking place. Knowledge from many fields such as radiation driven hydrodynamics, solid state physics, molecular chemistry or radiative transfer is necessary to draw a clear picture, particularly of the late stages of evolution. This section gives a summary of the important aspects of a stellar voyage through the AGB phase, focusing on the circumstellar environments of carbon stars.

1.2.1 Stellar Evolution to and on the AGB

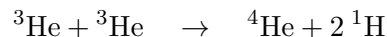
Pre-AGB Evolution

Stars eventually going through the AGB phase span a wide range of zero age main sequence masses. Depending on whether an object starts at the lower or upper end of the $\sim 0.8\text{--}8 M_{\odot}$ interval, the evolutionary track in the Hertzsprung-Russel diagram (HRD) will vary. Thus stars of different mass do not experience their time on the AGB the same way and certain processes will or will not happen, influenced also by the metallicity. In Fig. 1.2 the paths of a low mass ($1 M_{\odot}$) and an intermediate mass ($5 M_{\odot}$) star are sketched.

As for all main sequence stars, the energy is supplied by Hydrogen burning in the core. Out of all fusion processes it is the one providing the highest energy output per converted mass ($E_{\text{H}} = 6 \times 10^{14} \text{ J kg}^{-1}$). In a low mass star (e.g. $1 M_{\odot}$) the proton-proton reaction or *pp-chain* is the dominant process. It runs at temperatures of about 5 to $15 \times 10^6 \text{ K}$. The by far most probable reaction branch is

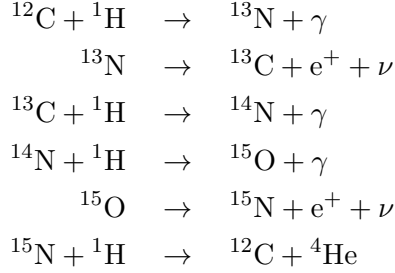


and after this has occurred twice, the reaction



yields the helium. The fusion rate and thus the energy output strongly depends on temperature: $\varepsilon_{\text{pp}} \propto T^4$. In the case of more massive stars, where the core temperature gets as high as 1.5 to $3 \times 10^7 \text{ K}$, the so-called *CNO-cycle* or *Bethe-Weizsäcker-cycle*

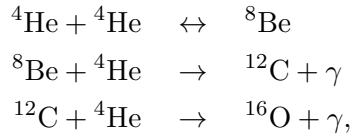
(after Hans Bethe and Carl von Weizsäcker, who independently proposed this reaction) becomes dominant. In the main cycle



carbon, nitrogen and oxygen act as catalysts, where the critical (i.e. slowest) reaction is the one of ${}^{14}\text{N}$ with ${}^1\text{H}$. The temperature dependence of the energy output is much higher than in the pp-chain, $\varepsilon_{\text{CNO}} \propto T^{12}$ to $\varepsilon_{\text{CNO}} \propto T^{18}$, also causing the core to become convective.

When the hydrogen in the core is exhausted the star leaves the main sequence and crosses the *Hertzsprung Gap*. In the case of the $1 M_{\odot}$ star the He core becomes electron degenerate. The H burning continues in a surrounding shell, with the fusion products adding more mass to the core, which, because of its degeneracy, contracts as matter is added. At the same time the star starts to expand and its outer layers become convective, until this runaway stops at the *Hayashi limit*. At this point the convective zone reaches the deep layers where H fusion has taken place and can bring processed material up to the surface, a phenomenon called *first dredge-up*. As a consequence the abundances at the surface will change. Typically, ${}^{14}\text{N}$ and ${}^3\text{He}$ increase, while Li and ${}^{12}\text{C}$ decrease and the oxygen abundance remains constant.

Continuing the steep path on the RGB, the luminosity of the star is almost exclusively provided by the H burning shell. The burning rate, however, is determined by the size and mass of the core. When the core temperature reaches 10^8 K, He burning starts via the *triple-alpha* reaction:



which is extremely sensitive to changes in temperature. The relation is $\varepsilon_{3\alpha} \propto T^{\nu}$, where typically $\nu = 30 - 40$. The ${}^8\text{Be}$ core is unstable and decays after only 10^{-16} s, hence very high densities are required to enable the reaction to stable ${}^{12}\text{C}$ in time. In a less probable reaction, also ${}^{20}\text{Ne}$ can be created from ${}^{16}\text{O}$. Because of the degenerated core, where temperature and density are basically decoupled, the helium ignition is very harsh, also known as the *helium core flash*. Such a sudden ignition only occurs in stars of masses below $\sim 2.25 M_{\odot}$. However, most of the produced energy does not reach the surface, thus such an event is not directly observable.

From their highest point on the RGB the low mass, low metallicity stars then quickly move to the *Horizontal Branch*, whereas the metal rich ones find themselves in the *Red Clump*. Here the core helium burning becomes quiescent while hydrogen is still burned in a shell. Eventually, the AGB phase sets in when the central He is exhausted and

the C-O core again becomes degenerate, while the energy is supplied by the He and H burning shells, separated by the intershell region. In this state the mass is extremely concentrated in the centre. Considering the model of an $1 M_{\odot}$ star, about 56% of the stellar matter are packed in the core and the surrounding H & He burning shells. While the convective envelope extends to $225 R_{\odot}$, the dense interior is just about the size of a *White Dwarf* ($0.035 R_{\odot}$)(see Habing & Olofsson 2004, p.32).

For the more massive objects the He burning runs comparatively calm, due to the non-degenerate conditions in the core. In the HRD the tracks take *blue loops*, whose appearance is determined by the two energy sources – He fusion in the core and the H burning shell. Subsequently, after the He burning in the core has ceased and moved to a shell, also the intermediate mass stars begin to ascend up the AGB.

Evolution on the AGB

The asymptotic giant branch can be divided into two parts. An early phase (E-AGB), where the inner structure is established, qualitatively regardless of stellar mass, and the thermally-pulsing period (TP-AGB) with thermal instabilities determining the evolution.

On the E-AGB all objects share the degenerate C-O core, where cooling by neutrino emission ensures that no further carbon burning takes place. This criterion also sets the upper mass boundary for AGB stars to $8 M_{\odot}$. Meanwhile, the establishment of a He burning shell (which at this time provides most of the energy) leads to a strong expansion, extinguishing the shell H fusion. Thus the “thermal barrier” vanishes and the convective envelope can reach inwards. In intermediate mass stars the convection zone can reach to the deeper layers containing elements processed in the CNO-cycle. Mixing them up to the surface, again the element abundances are changed, especially ${}^4\text{He}$, ${}^{12}\text{C}$ and ${}^{14}\text{N}$ are altered. This event is commonly referred to as the *second dredge-up*, which, however, only takes place in stars that are above the $4 M_{\odot}$ limit. On the other hand the mixing enriches the inner regions with hydrogen from the surface which eventually leads to a re-ignition of the H shell. Soon the He burning layer becomes unstable and the star enters the TP-AGB.

A reason for the thermal pulses (TPs) is the sensitivity of the energy production in the triple alpha process to temperature changes, i.e. $\varepsilon_{3\alpha} \propto T^{30-40}$, thus a small T-perturbation can cause a thermal runaway, if certain boundary conditions are fulfilled (Schwarzschild & Härm 1965). Each pulse or *shell flash* generates large luminosities up to $\sim 10^8 L_{\odot}$. The deposited energy can, however, not be entirely radiated outwards, hence the intershell region becomes convective for a few hundred years. The heating additionally causes this convective zone to expand drastically, pushing the H burning shell to cooler outside regions. There the nuclear burning is extinguished, which leads to a drop of the star’s surface luminosity after a short peak owned to the He shell flash. Following the pulse the luminosity contributed by the He burning begins to decrease again. Meanwhile the dormant H shell allows the convective outer layers to extend deeper inside once again, mixing up heavier elements. In the case the envelope can penetrate into the region of the former intershell, elements such as ${}^{12}\text{C}$ and other products of He burning, as well as heavy elements built up by slow neutron capture, are brought to the surface. Keeping the terminology, this is designated as the *third dredge-up* (TDU).

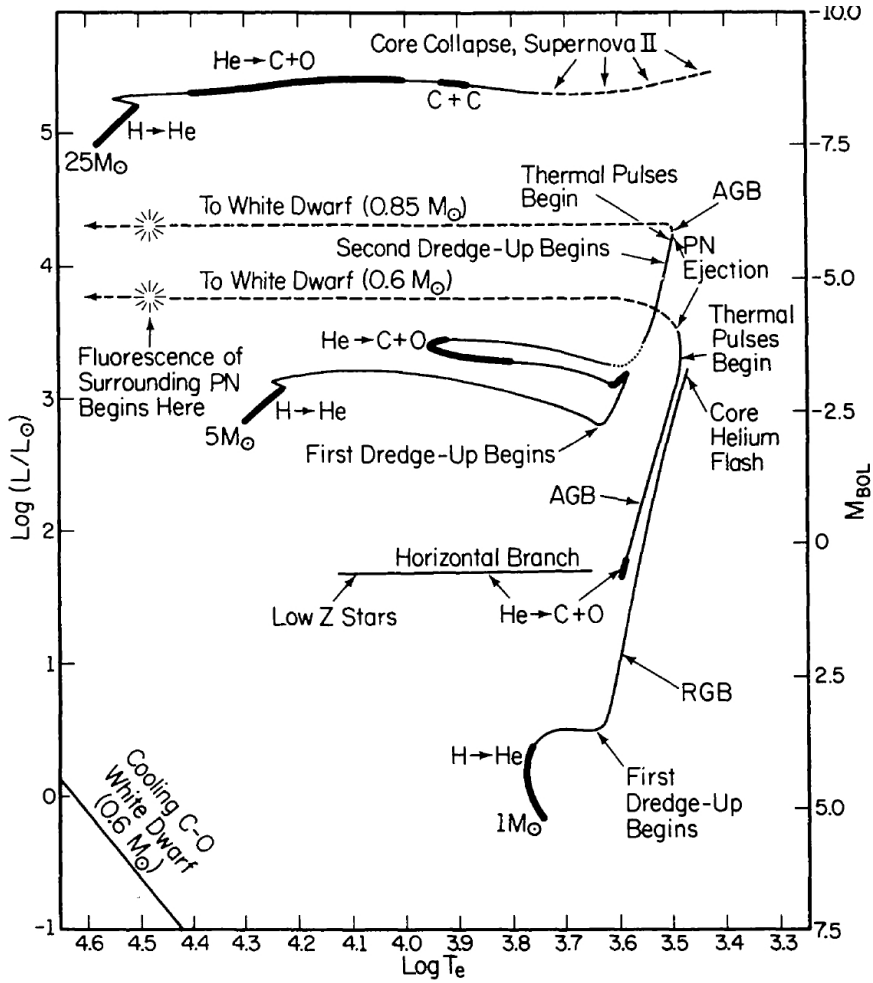


Figure 1.2: Evolutionary tracks in the Hertzsprung-Russell diagram for stars of different masses. A star having an initial mass of $1 M_{\odot}$ has a very pronounced RGB phase, compared to a $5 M_{\odot}$ star. It also experiences a rather sudden core helium flash, taking it to the horizontal branch (or, depending on metallicity, the red clump), whereas for more massive stars (above $\sim 2.25 M_{\odot}$) the He-burning sets in more smoothly. The maximum luminosity a star can reach at the top of the AGB again depends on its mass. Here one can also see from where the term *asymptotic giant branch* originates – while going through the AGB phase the evolutionary track *asymptotically* approaches the red giant branch. Eventually, after the post-AGB and planetary nebula phase the final white dwarfs remain. Compared to the mass ranges at the turn-off point from the main sequence, their masses lie in a much narrower band in the end. Figure taken from Iben (1985).

From an observational point of view such a process explains the existence and frequency of carbon rich stars (see also Sect. 1.2.2), isotope ratios (e.g. $^{12}\text{C}/^{13}\text{C}$) and abundances of s-process elements. Regarding the latter, the radioactive element technetium (Tc) is a particularly interesting case, as it has no stable isotopes. The half life of the most important one, ^{99}Tc , is 210 000 years. This property makes it an ideal tracer for recent dredge-ups, since a detection means that a star must have experienced a thermal pulse within the last few 10^5 yr.

The efficiency of the TDU can be roughly quantified by the so-called dredge-up parameter λ , defined as $\lambda = \Delta M_{\text{dredge}}/\Delta M_c$. Here M_{dredge} is the dredged-up mass in one thermal pulse and ΔM_c the amount of mass through which the H burning shell has proceeded before the next shell flash. Evolutionary calculations show a dependence of λ on the stellar mass. For early flashes and low envelope masses $\lambda = 0$, whereas for lower mass stars ($\lesssim 2.5 M_\odot$) $\lambda \lesssim 0.3$ and for more massive stars ($\gtrsim 5 M_\odot$) $\lambda \lesssim 1.0$ (Habing & Olofsson 2004, p.41).

Following the third dredge-up the star contracts and the H ignites again. Soon it is the dominant contribution to the surface brightness again, which also starts to raise again, until the next thermal pulse. During the lifetime on the AGB – typically 10^6 yr, but considerably varying with mass – a star can undergo many pulse-TDU-interpulse cycles, until most of its envelope is ejected by a heavy mass-loss (see Sect. 1.2.4). Unsurprisingly, several stellar parameters (pulsation period, effective temperature, etc.) are affected by the repeating variations of the star’s inner structure, displaying periodic development themselves, as can be seen in Fig. 1.3. Roughly speaking, a cycle lasts about 10^5 yr, but Paczynski (1975) also found a linear relation between the interpulse period and the core mass M_c in the case of well established pulses:

$$\log \tau_{\text{ip}} (\text{yr}) = 3.05 - 4.5 (M_c - 1.0),$$

suggesting a higher frequency of TPs with growing core mass. In the following, more extensive calculations showed an additional dependence of the relation on metallicity, with τ_{ip} increasing for lower metallicities (Wagenhuber & Groenewegen 1998).

Another simple relation given by Paczyński (1970) connects the luminosity L to the core mass:

$$L = 59250 (M_c - 0.522).$$

Looking at the HRD, this relation reflects a star’s ascend up the AGB, as more nuclearly processed material is added to the core with time. This relation, however, breaks down for objects with large envelope masses. Therefore, improved, more complex relationships were proposed over the years, taking into account element abundances, for example (e.g. Boothroyd & Sackmann 1988).

Variability

One property almost all (TP-)AGB stars have in common is their variability. While some display distinct and strictly periodic oscillations in their light curves (obtained for example in surveys such as MACHO (Alcock et al. 1995) and OGLE (Udalski et al. 1993)), for others a clear pulsation period is hard to determine. Depending on the amplitude and shape of the light curve giant stars are classified in a scheme of three

main visual variability types, all belonging to the long period variable (LPV) class (e.g. as in the *General Catalogue of Variable Stars* (GCVS) Samus et al. 2009):

- *Miras* typically show late-type emission spectra (Me, Ce, Se) and have light amplitudes greater than 2.5 mag in the V-band, getting as high as 11 mag. The periods lie between 80 and 1000 days and are well pronounced. On the contrary, the variations of the bolometric magnitude, m_{bol} , and in the infrared (since most of the light is emitted there) are far less dramatic, usually below 2.5 mag, or even ≤ 0.9 mag in the K-band. One reason for the drastic visual changes in brightness is the TiO molecule. Its opacity (in the visual) is very sensitive to temperature, hence even small variations in T can cause significant changes in luminosity over one pulsation cycle (Nowotny et al. 2010, 2011). Furthermore, there is also a lag in phase between the visual and infrared light curve maxima of 0.1 to 0.2.
- *Semiregular variables* (SR) are split into 4 subcategories, SRa, SRb, SRc, and SRd. Thereof, only the first two are of concern for AGB stars, since SRc's have supergiant spectra and SRd stars are of earlier type than M0 (Kerschbaum & Hron 1992). SRa stars are similar to Mira variables in the sense that they also display distinct regular periodicity, although having smaller amplitudes, $\Delta V \leq 2.5$ mag by definition. The periods are in the range of 35–1200 days, with most of the stars having $P \leq 450$ days.
SRb stars exhibit an even larger period range ($20 \leq P \leq 2300$ days), but the periodicity is poorly defined in comparison. Usually, a mean cycle length is assigned, though slow irregular behaviour or episodes of constant brightness can be prominent features in the light curves. Sometimes even multiperiodicity can be observed (Lebzelter et al. 1995).
- *Irregular variables* (LB): stars of this class show no apparent regular variations in their light curves. However, objects are often categorised as irregular because of insufficient study (Lebzelter & Obbrugger 2009).

In the case of very evolved AGB stars, circumstellar dust formed from ejected material (see also Sect. 1.2.3) obscures the emitted stellar light. Such objects are hard to detect in the visual, which is why they are not found in the GCVS. This class of *infrared variables* was discovered by observing the 1612 MHz OH maser emission on one hand (e.g. Herman & Habing 1985), and by infrared surveys on the other hand. Compared to the objects listed in the GCVS these stars show longer periods and larger amplitudes ($\Delta K \leq 3$ mag).

Considering physical parameters, the pulsation period depends on the stellar radius and mass, i.e. the density ($P \propto 1/\sqrt{\rho}$ in hydrostatic equilibrium). Given the relation $P \propto R^\alpha M^{-\beta}$ Fox & Wood (1982) and Wood (1990) find $\alpha \approx 1.5 - 2.5$ and $\beta \approx 0.5 - 1.0$, respectively, from more elaborate modelling. Thus, as these properties change roughly periodically between shell flashes, also the pulsation period exhibits long-term modulations. In addition, the decreasing stellar mass due to the wind causes the pulsation period to increase in the long run (cf. Fig. 1.3). Consistently, the long periods found for the aforementioned dust-enshrouded sources agree with such model predictions.

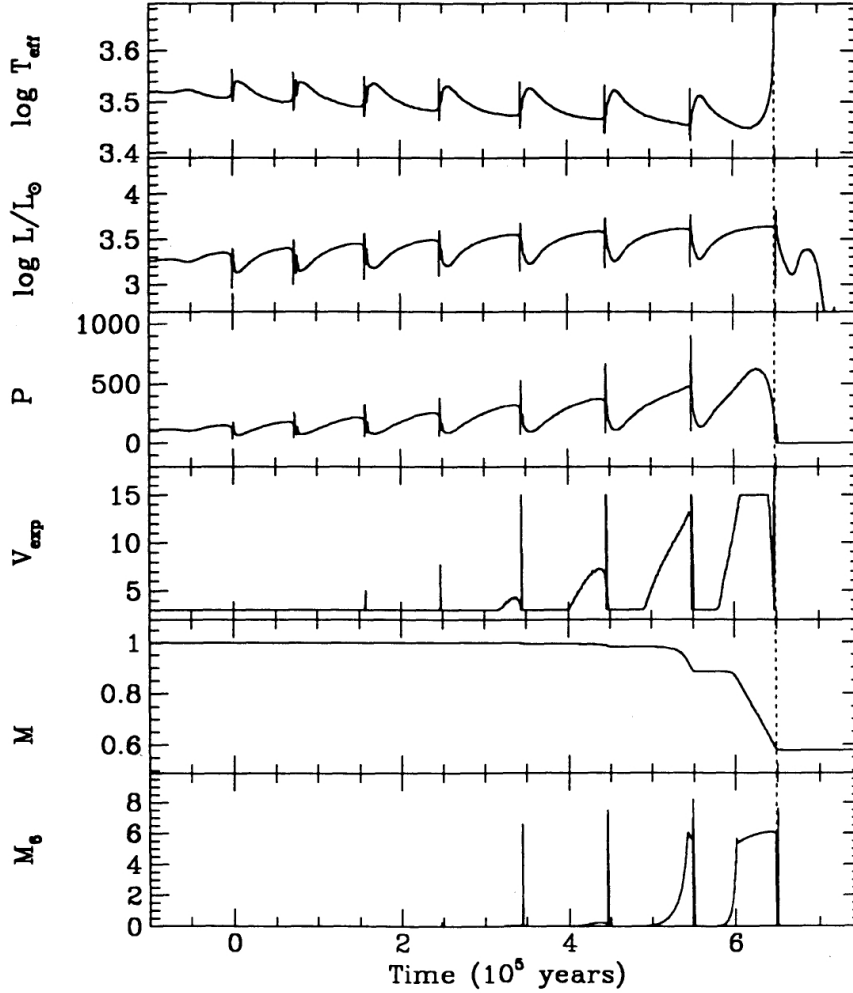


Figure 1.3: Evolution of different stellar quantities during the TP-AGB phase. The time axis' zero point is set after the first major thermal pulse has occurred. Top to bottom: Effective temperature in K, luminosity in solar units, pulsation period in days, expansion velocity in km s^{-1} , stellar mass in solar units and mass-loss rate in units of $10^{-6} M_{\odot} \text{yr}^{-1}$. The dotted vertical line designates the termination of the AGB phase, i.e. when the star has ejected its entire envelope. Results are from model calculations of a one solar mass star with metallicity $(Y,Z)=(0.25,0.008)$ in Vassiliadis & Wood (1993).

Similar to other variable types such as Cepheids, also the pulsation periods of AGB stars show a correlation with luminosity. Especially Miras are found to have a pronounced period-luminosity ($P-L$) relation (see e.g. Feast et al. 1989). Interrelations of properties of SR variables have also been studied in depth (Kerschbaum & Hron 1992, 1994; Kerschbaum et al. 1996), and $P-L$ relationships for this variability class were derived as well (e.g. Groenewegen & Whitelock 1996; Knapp et al. 2003). Establishing a quantitative description of these correlations is far from being easy. First, most AGB stars are far away, thus having too small parallaxes to be reliably determined. Second, due to the nature of TP-AGB stars – e.g. the extended structure, asymmetries on the surface, variability – parallax measurements of objects that are close enough are usually deteriorated and thus calibration distances are only available with limited certainty (Bastian & Hefele 2005). Hence $P-L$ relations are commonly obtained by using samples at rather well known, not greatly differing distances, such as objects in the Magellanic Clouds (e.g. Wood et al. 1999). Once derived, $P-L$ relationships can give a good additional constraint on distance, particularly in the case of solitary field stars.

1.2.2 Carbon Stars

The C-O Dichotomy

Although AGB stars share many aspects during their evolution, there are nevertheless distinct differences that can be the cause of qualitatively different behaviour. According to their spectral emission and absorption features they are grouped into three chemical classes: M-, S- and C-type stars. M-types are also referred to as *oxygen rich* stars, since the most abundant molecules in their atmosphere bear this element. In C stars on the other hand carbonaceous species are observable (Tab. 1.1), whereas S-type stars show features of more peculiar element mixtures. The rather strict separation into an either carbon or oxygen environment can be explained by one single molecule – carbon monoxide (CO). Except for hydrogen and helium, carbon and oxygen are the most abundant elements in an AGB star. However, due to the high bond energy of the CO molecule (11.09 eV) most of the carbon and oxygen is locked up in such an energetically favourable state. Consequently, only the more abundant element remains available for the formation of more complex compounds, starting with e.g. SiO and MgO or C₂H₂ and SiC in M and C stars, respectively. A discussion of the dominant role of CO is given in Dominik et al. (1993), for example. From an observational point of view the fact that, after H₂, CO is the most common molecule in AGB atmospheres and its resistance against dissociation are of great importance.

Given the cosmic element abundances, compared to carbon, oxygen is the more abundant element (Burbidge et al. 1957). Therefore, all AGB stars start off as oxygen rich or M-type stars, where one could measure $C/O < 1$. In the course of reoccurring thermal pulses and subsequent dredge-up events the surface element composition is altered with time, i.e. C and other heavy atoms are brought up, changing the C/O ratio to $C/O > 1$. Thus, C stars can be seen as evolutionary descendants of M-type stars. Of course this transformation happens only to objects that undergo a TDU at all or don't lose their envelope before the surface chemistry has been sufficiently enriched by carbon. This criterion sets the (observationally determined) lower mass limit for C

stars to $M_{\text{MS}} \gtrsim 1.5 M_{\odot}$, where M_{MS} is the main sequence mass (Wallerstein & Knapp 1998). In the case that $\text{C/O} \approx 1$ most of the carbon and oxygen is tied together in CO, which gives less abundant elements a crucial role in the molecular composition (e.g. Zr, Ti). Such stars are designated as S-type.

Looking at very luminous (and thus massive) stars it appears that there are no carbon rich among them (part of the *carbon star mystery*, see Iben 1981), although one would expect C to be mixed up by TDU in such objects. The process responsible for this phenomenon is called *hot bottom burning* (HBB). In intermediate mass stars ($4-5 M_{\odot} < M < 8 M_{\odot}$) the convective envelope can extend inwards to the H burning region. There the already or to-be dredged-up elements are further processed before they are brought up to the surface. For example, carbon is transformed into ^{14}N by the CNO cycle that is active in the H shell, leading to a decrease in ^{12}C and an increase in ^{14}N abundance. In fact, HBB is considered as one of the most important sources of nitrogen. It can alter the surface composition dramatically, given the typical turn-over time of ~ 1 year for the convective envelope (Karakas 2011), the whole envelope material is processed numerous times during an interpulse cycle (i.e. before the next TDU occurs).

Species	$f(\mathbf{X})$
H ₂	1
CO	1.6×10^{-3}
C ₂ H ₂	2.2×10^{-4}
C ₂ H	1.1×10^{-4}
N ₂	9.5×10^{-5}
HCN	8.5×10^{-5}
CS	2.3×10^{-5}
SiS	9.8×10^{-6}
C ₃ H	9.5×10^{-6}
CN	1.6×10^{-6}
SH	7.0×10^{-7}
SiH	6.7×10^{-7}
SiC ₂	3.7×10^{-7}
HCl	3.4×10^{-7}
CH ₃	2.6×10^{-7}
CH	1.6×10^{-7}
C ₂	6.2×10^{-8}
NP	5.5×10^{-8}
SiO	4.8×10^{-8}
H ₂ S	4.4×10^{-8}

Table 1.1: The 20 most abundant molecules produced in a C-rich atmosphere. Given are the fractional abundances $f(X)$ of the species X relative to the most common molecule, H₂. Numbers are taken from LTE calculations for $\text{C/O}=1.5$ and $T_{\text{eff}}=2300$ K, representative of the carbon star IRC+10216 (Olofsson 2004).

1.2.3 Dust in Circumstellar Environments

Dust Formation

The major part of matter in the atmosphere and the vicinity of an AGB star is in the gaseous state, whereas only a small fraction is found in small solid particles, sloppily referred to as dust ($M_{\text{gas}}/M_{\text{dust}} \approx 200$). Despite this mass disparity dust is of utter importance during the evolution on the AGB, for instance when it comes to stellar winds and hence mass-loss (see Sect. 1.2.4). The formation processes responsible for the growth from atoms and molecules to macroscopic structures are complex and depend on a large set of not always easily determinable parameters. Numerous publications are dealing with the different theoretical approaches to a quantitative description of grain formation and the consequences of various environmental conditions (e.g. Gail 2010; Molster et al. 2010; Ferrarotti & Gail 2006; Sedlmayr 1994, and references therein). In short, the two critical quantities that fundamentally govern the dust formation process are temperature and density. For a material to condense from the gas phase to solid particle seeds the temperature in the atmosphere must lie below the respective dust condensation temperature T_d . Approximately, the values are in the range between 500 K (magnetite, Fe_3O_4) and 1800 K (corundum, Al_2O_3) (Millar 2004, p.261). The condensation radius r_c , at which this requirement is fulfilled, in units of the stellar radius R_\star can be given as

$$\frac{r_c}{R_\star} = \frac{1}{2} \left(\frac{T_c}{T_\star} \right)^{-\frac{4+p}{2}},$$

where T_\star and T_c are the stellar temperature and the condensation temperature of the dust species, respectively. The parameter p accounts for the characteristic wavelength dependent opacity κ_λ of the respective dust grains, which, for the critical region around the flux maximum, can be approximated by a power law of the form $\kappa_\lambda \propto \lambda^{-p}$. As an example, Höfner (2007) get $r_c/R_\star \approx 3$, adopting $T_c \approx 1500$ K, $T_\star \approx 3000$ K and $p \approx 1$ for amorphous carbon grains, being consistent with detailed modelling results.

Secondly, the density of the considered species must be high enough to allow for efficient growth. The stellar atmosphere is not static, and as the matter moves outwards from the condensation radius the decreasing temperature favours an increased condensation rate. Simultaneously, however, the density also decreases ($\rho \propto r^{-2}$ in the case of a constant velocity wind, in a more realistic scenario the gradient will be steeper, since the wind is accelerated to some point) slowing down the rate at which further atoms and molecules can be adsorbed. Simple estimates by Gustafsson & Höfner (2004, pp.180) show that during the typical growth timescale of a dust grain $t_{\text{growth}} = 2 \times 10^7$ s the density of the surrounding gas phase decreases by a factor of 2, resulting in a significantly reduced growth rate. As a consequence, grain growth can stop due to dilution before the condensible material is entirely depleted.

Additionally, the pulsations of an AGB star complicate the thermodynamic conditions. On the one hand changes in both the effective temperature and luminosity during a pulsation cycle affect the circumstances of dust formation, on the other hand shock waves can perturb the structure on short timescales, e.g. material is lifted to cooler regimes, which positively influences the growth rate (an important aspect in the explanation of strong mass-loss). Given the usual pulsation periods, the relevant timescales

for the changes are of the order of 10^6 to 10^7 s, similar to t_{growth} . Thus, the growth processes in an AGB atmosphere do not take place under equilibrium conditions, and the evolution of the dust grains will critically depend on the relations between the occurring timescales (see e.g. Sedlmayr 1994; Gail 2010).

Circumstellar Dust Chemistry

Given the dichotomy in the surface chemistry of AGB stars, the condensed dust species can be expected to be built from either oxygen rich or carbon rich elements and molecules. Based on thermal equilibrium calculations, Gilman (1969) was the first to explain that M-stars would produce silicate particles while carbonaceous grains would be formed in C-type stars. Despite this division, there remains quite a number of compounds present in the atmospheres. An overview of the observationally confirmed ones is given in Tab. 1.1. To identify the bonds that are most likely to grow to macroscopic structures, their respective properties have to be known. For example, to allow a formation close enough to the star, i.e. at high densities, a high condensation temperature is required. Such *refractory species* are in the case of carbon stars, e.g. amorphous carbon (amC), TiC and SiC. Additionally, to keep t_{growth} low, the candidate material has to be sufficiently abundant. Considering only the temperature and density/abundance characteristics, thus CO and N₂ with their high bond energies would be prime candidates. However, for efficient grain growth reactive elements/bonds are needed, which is why these two very inertly behaving molecules are not found as dust constituents.

Compared to M-type stars, the chemistry in carbon stars is less complex, in the sense that there are less possible condensates. The most prominent (i.e. detected) grain types are amorphous carbon, SiC and MgS. The term amorphous carbon is rather broad and it covers material with no dedicated atomic configuration. Furthermore, carbon also comes in ordered shapes, e.g. having a layered structure as graphite, or in crystalline form as resistive diamond. The formation process and optical properties of carbonaceous grains are well understood, because soot occurs in combustion engines and its properties are therefore well studied in the laboratory (see e.g. Cherchneff & Tielens 1994).

1.2.4 Mass-loss through Stellar Winds

Mass-loss is a common phenomenon for most stars. During their evolution they lose part of the mass in an outflow of gas and, in certain object classes, dust. One of the earliest evidences for such stellar winds was presented by Biermann (1951), who showed that sole radiation pressure did not suffice to align cometary tails away from the sun and an additional force was needed. Nevertheless, in the case of our sun the mass-loss rate (MLR) is, typical for a main sequence star, very low ($\sim 10^{-14} M_{\odot} \text{ yr}^{-1}$). On the AGB on the other hand, mass-loss plays a much more significant role, where winds can eject stellar matter at rates of $10^{-7} M_{\odot} \text{ yr}^{-1}$ to $\sim 10^{-4} M_{\odot} \text{ yr}^{-1}$. Such heavy winds change the appearance of an AGB star on very short timescales. Regarding the terminal velocities, AGB winds are on the lower end of the scale, the characteristic values range from 5–25 km s⁻¹ (compared to ~ 500 km s⁻¹ for the solar wind)(for mass-loss rate distributions see, e.g. Schöier & Olofsson 2001; Groenewegen et al. 2002; Olofsson et al. 2002). The large MLR together with the low speeds thus implies very high density in the

wind and its forming region. To trigger an AGB wind, a very effective driving mechanism is needed. Although gas accounts for most of the circumstellar mass, radiation pressure on the atoms and molecules does not provide enough momentum to cause the observed mass-loss rate. At present, the generally accepted scenario combines two effects to explain the required momentum transfer: shock waves caused by the pulsation, which extend the scale height of the atmosphere, and dust grains as the main wind drivers.

Compared to gas, solid particles have higher mass absorption coefficients. While molecules can take up momentum only at discrete wavelengths, dust grains absorb over the whole continuum. Hence dust, despite the low mass fraction it has compared to gas ($\sim 1/200$), couples much more effectively to the stellar radiation field. However, in a hydrostatic configuration the growth rate outside the condensation radius would be too low to support sufficient dust formation. Therefore, shocks are needed to lift material outwards, increasing the density in cooler layers (see Bowen 1988). Under such modified conditions grains can condense to a degree where they are able to accelerate to speeds that allow them to escape the stellar atmosphere. On its way out, the dust drags along the gas particles, resulting in considerable mass-loss. The efficiency of the two-step momentum transfer from the photons to the gas can be quantified by comparing the momentum flow of the two components $\beta = \frac{\dot{M}v_{\text{exp}}}{L_{\star}/c}$. In optically thick environments $\beta > 1$ is possible, i.e. when a photon interacts with dust grains several times.

The two dominating forces acting on the dust are gravity and radiation pressure from the star. Depending on which component prevails, the grains will either reach escape velocity or remain bound to the atmosphere. Quantitatively, this can be expressed as a ratio between the two forces:

$$\Gamma_{\text{d}} = \frac{\kappa_{\text{H}}L_{\star}}{4\pi cGM_{\star}},$$

where κ_{H} is the opacity of the dust grain. In the case $\Gamma > 1$, the grains can take up enough momentum from the radiation field to form a wind. For $\Gamma = 1$, no net force is acting and the grains continue to move at their speed gained from the shock. Finally, if $0 < \Gamma < 1$, it depends on the outward directed velocity of the matter at the point where dust formation sets in (r_c), whether the grains and consequently the gas fall back to the surface or overcome the gravitational bond. In such a case the escape velocity is modified, i.e. reduced by the factor $(1 - \Gamma)$, due to the momentum transfer to dust ($v_{\text{esc}} = \sqrt{2GM_{\star}(1 - \Gamma)/r}$) (Höfner 2007). In Höfner (2007) Γ -ratios are calculated for various grain species in order to find out which could, in principle, drive a wind. Adopting a mass-luminosity ratio for the central star of $L/M = 5000 L_{\odot}/M_{\odot}$ and the species in question fully condensed to solid particles (i.e. $f_c = 1$), in the case of a carbon star ($C/O = 1.5$) the momentum transfer is well above the critical threshold with $\Gamma = 10$ for amorphous carbon. For such material, even partly completed condensation ($f_c \approx 0.3\text{--}0.5$) suffices for a wind to develop. Contrary, the situation is less clear for silicates that are expected to form in O-rich environments. The problem and a possible solution to it are discussed in several publications (e.g. Woitke 2006, 2007; Höfner 2008). Despite this shortcoming, dust-driven winds supported by shock waves in the pulsating AGB star atmospheres are currently the most likely scenario for mass-loss, since the predicted wind velocities and MLRs are comparable to the values derived from observations.

The matter outflow from an AGB star can be characterised by two main properties, the mass-loss rate \dot{M} and the (terminal) expansion velocity v_{exp} . Both quantities depend on the stellar properties. Whereas the MLR is essentially determined by the conditions at the transonic point of the wind, the expansion velocity depends on the interplay between dust and gas beyond this region. For a dust-driven wind it can be expected that \dot{M} and v_{exp} correlate to some degree – from observations Olofsson (2004) find that $\dot{M} \propto v_{\text{exp}}^{2.5-3.5}$ (cf. Fig. 1.4). Simplified model calculations by Habing et al. (1994) further show a relation of the terminal velocity to Γ :

$$v_{\text{exp}} = \sqrt{2GM(\Gamma - 1)/r_0}.$$

r_0 is the point at which the acceleration begins (\sim the condensation radius).

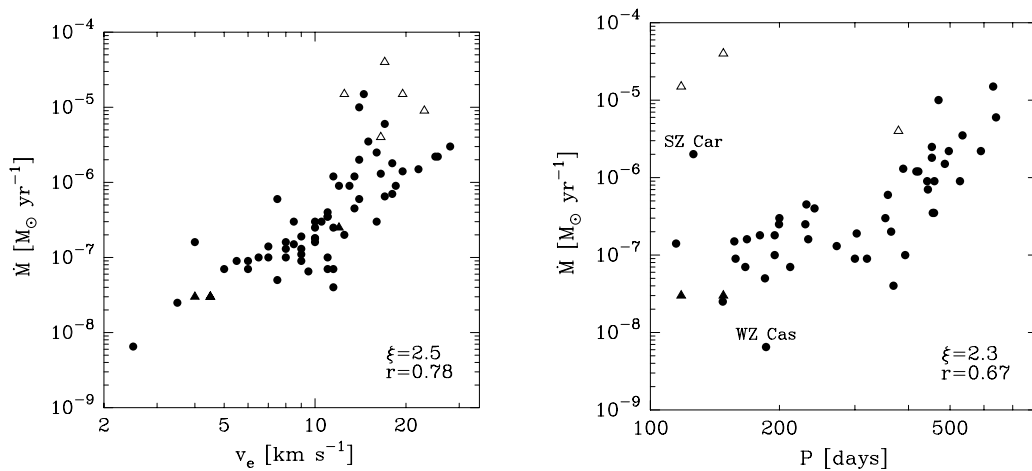


Figure 1.4: Based on molecular line emission, a correlation between the MLR and the expansion velocity (left) and MLR and the pulsation period (right) is found (Schöier & Olofsson 2001).

In particular the mass-loss rate is related to several stellar properties, e.g. mass, luminosity, temperature and metallicity. Numerical simulations (Höfner & Dorfi 1997; Winters et al. 2000; Wachter et al. 2002) suggest that the MLR grows with luminosity and decreases towards larger masses and higher temperatures. On the other hand, the effect of pulsation and, for carbon stars, the C/O ratio is negligible. However, in observational data it is not easy to disentangle the influences on the mass-loss rate. Given the fact that all low and intermediate mass stars end up as White Dwarfs with masses less than $1 M_{\odot}$, objects starting at higher main sequence masses lose more material. Due to similar timescales for mass-loss it can be concluded that there is a positive correlation between main sequence mass and achieved MLR.

As shown in the evolutionary predictions of Vassiliadis & Wood in Fig. 1.3, the stellar properties change with time and one can thus expect the MLR to vary, too. As the AGB star loses a considerable fraction of its mass during the TP phase, the MLR is changing, too. Observationally, this is indicated by a period-mass-loss relation (Fig. 1.4 for C stars), since the pulsation period correlates with the current mass ($P \propto R^{3/2} M^{-1/2}$).

Towards the end of the AGB evolution the mass-loss increases dramatically (*superwind phase*), reaching MLRs of $\dot{M} = 10^{-4} M_{\odot} \text{ yr}^{-1}$. This phase is terminated very rapidly, when the envelope is almost entirely blown away ($\sim 0.001 M_{\odot}$).

Velocity Drift

Considering the mass-loss mechanism in a dust-driven wind – radiation pressure accelerates the grains, which then transfer momentum to the gas particles via collisions – one can expect the two components to move at different speeds, i.e. that there is a so-called *velocity drift* $v_d = v_{\text{dust}} - v_{\text{gas}}$, with the dust moving faster than the gas. According to model calculations by Habing et al. (1994), the magnitude of this dispersion correlates with the mass-loss rate. At high MLRs ($\dot{M} = 10^{-5} M_{\odot} \text{ yr}^{-1}$) the drift is small, the dust grains can transfer a considerable amount of momentum to the gas. As the mass-loss rate decreases, the dust velocity increases, while the gas speed slows down, until at low MLRs the two components basically decouple because the small fraction of dust cannot drag the gas significantly. A minimum MLR is given ($\dot{M}_{\text{min}} \approx 3 \times 10^{-8} M_{\odot} \text{ yr}^{-1}$), below which the gas does not receive enough momentum to escape.

1.2.5 Circumstellar Envelopes (CSEs)

Eventually, the stellar matter outflow forms a shell of dust and gas, enclosing the star. Such an envelope will heavily affect the spectral properties of the observed light (see e.g. Habing 1996, and references therein). In the simplest case an overall spherically symmetric envelope can be assumed. For regions rather close to the star ($\sim 10^{15}$ – 10^{16} cm) interferometric maps support such a geometry for many of the known objects. Additional evidence comes from the fact that molecular line observations show a good fit to the angular size vs line-of-sight velocity relation expected for an expanding spherical shell (e.g. Olofsson et al. 2000). On the other hand, a fraction of objects does show departures from sphericity already at the inner regions (Olofsson 2004, and references therein).

It is known from observations, mostly in the infrared regime (Cox et al. 2012), that there is a rather large morphological diversity when looking at structures further out in the stellar environment ($> 10^{17}$ cm), where interactions between the wind and the ISM become more and more important. The discovered shapes range from bow shocks due to high space velocities to amazingly intricate geometries caused perhaps by binary systems. In many cases it is very challenging to draw conclusions about the actual 3D structure from the 2D imagery. Impressive and recently studied examples are TX Psc and X Her (Jorissen et al. 2011) and *o* Ceti (Mayer et al. 2011). However, also for the “large scale” structures astonishing spherical symmetry is observed around several sources (González Delgado et al. 2003; Olofsson et al. 2010; Cox et al. 2012).

Detached Shells

Circumstellar structures that have a narrow (in the sense that $\Delta R \ll R$), remarkably circular shape and show a vastly enhanced density and hence brightness compared to the immediate vicinity, are referred to as *detached shells*. Such structures are observable

in the IR, as well as in the (sub-)mm regime (Olofsson et al. 2000) and from (polarised) scattered light in the optical (González Delgado et al. 2003; Maercker et al. 2010). In principle, there are multiple explanations of how such structures can form: due to (1) a very short period of greatly increased mass-loss (a few hundred years), (2) a faster young wind interacting with a slower older ejection or (3) interaction of the stellar wind with the surrounding ISM. A detailed view on this class of objects and two representative examples is given in Chapter 4.

1.3 Observing Dusty Objects

As evident from numerous observations, the radiation originating from the central source is substantially altered by the CSEs. Depending on the ejected mass, especially the amount of condensed dust, these envelopes exhibit different optical depths. Accordingly, the effects range from slight reddening of the light to complete obscuration of the visible part of the spectrum. While the gas component manifests itself mainly in discrete spectral lines and bands, broad features (in the case of O-rich stars) or even featureless continuum emission (due to e.g. amorphous carbon) can be ascribed to the dust. Because of the low circumstellar dust temperatures the major part of the radiation is emitted in the infrared. Therefore, studying the solid fraction of CSEs was hardly possible until the 1960s and the rise of IR astronomy. A first survey in the near IR was conducted by Neugebauer & Leighton (1969), who detected 5000 sources, many of them having dusty envelopes, as subsequent studies showed. Also, IRC+10216, presently (because of its small distance) the most extensively studied carbon star was detected during this survey.

A severe shortcoming of ground based IR observations is, however, the high opacity of the earth atmosphere at these wavelengths. In the near and mid IR there are several “telluric windows” between the absorption bands that allow some radiation to reach the surface, but going to the far IR regime, the air layers basically absorb all the light. Thus space telescopes were necessary to expand the observable spectral range. The earliest mission for solely astronomical purposes was *IRAS* (Neugebauer et al. 1984), which surveyed almost the entire sky at 12, 25, 60 and 100 μm and took low resolution spectra. Although it had very limited spatial resolution ($30''$ – $2'$, due to the 59 cm telescope aperture) the photometric data were very fruitful. Based on these observations van der Veen & Habing (1988) created a classification scheme – the *IRAS two colour diagram* (Fig. 1.5) – where IR sources can be assigned to an object class depending on the colour ratios.

The next IR space mission was *ISO* (Kessler et al. 1996), but contrary to *IRAS* it wasn't a survey instrument. With its improved sensitivity and extended spectral range several CSEs have been imaged (e.g. Izumiura et al. 1996), albeit barely resolved due to the still small mirror size. More importantly, the improved spectral resolution and coverage allowed for detections and partial identification of numerous (dust) features in envelopes around O-rich stars. This meant a big leap in the field of astromineralogy (see, e.g. Molster et al. 2010).

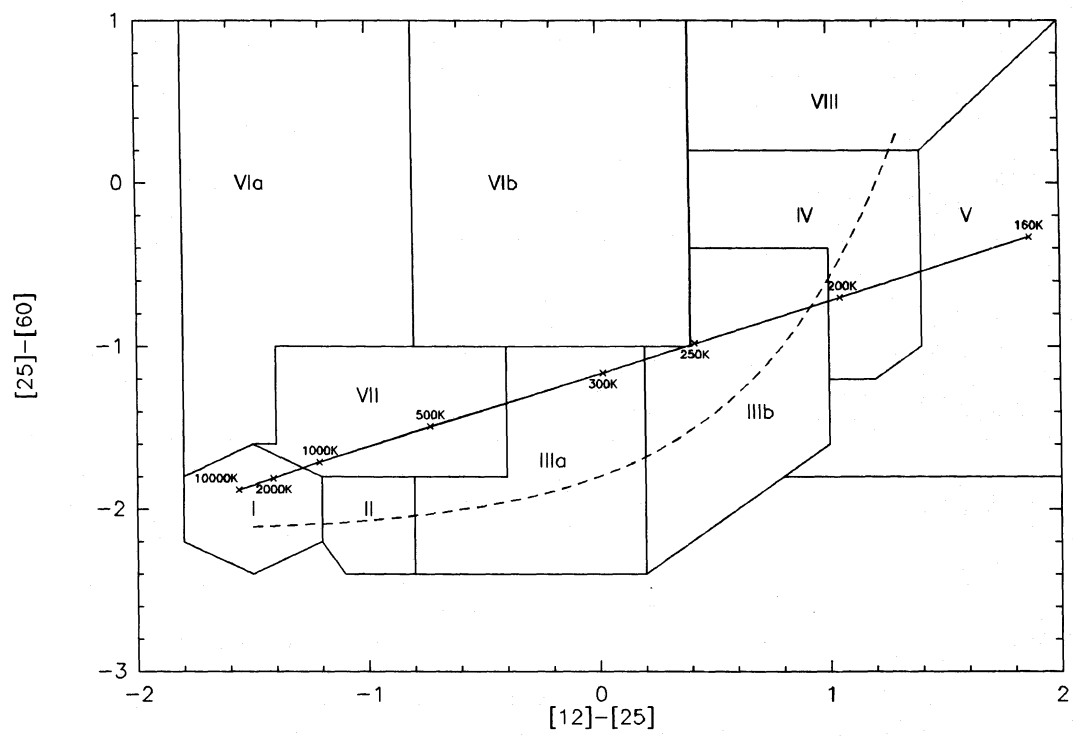


Figure 1.5: IRAS two colour diagram from van der Veen & Habing (1988).

Both spectral and imaging capabilities increased with the *Spitzer* (Werner et al. 2004) space telescope. Some spectacular detections of AGB environments, often showing interaction with the ISM (e.g. Geise et al. 2010), were made.

One of the latest space missions exploring in the IR was the Japanese-led *AKARI* (Murakami et al. 2007) satellite. With its sensitivity and resolution in the far IR circumstellar structures have been resolved to an extent where it is already possible to identify some morphological details in the dust component (e.g. U Hya, see Izumiura et al. 2011).

Comprehensive surveys were also carried out from ground based facilities. Currently in wide use are the *Two Micron All Sky Survey – 2MASS* (Cutri et al. 2003) and the *DEep Near Infrared Survey – DENIS* (Epchtein et al. 1994). These two complementary catalogues of the northern and southern hemisphere contain virtually all AGB stars in the Milky Way and the Magellanic Clouds. They provide photometric information in three NIR bands.

An alternative and more recent approach to study the dusty environment of AGB stars are observations of scattered stellar light at visual wavelengths, as first shown by González Delgado et al. (2001, 2003). This method provides high angular resolution and is able to map the circumstellar structures in fine detail. In addition, polarisation measurements can provide even more information on the dust distribution. Reasonable results, however, can be expected for brighter objects with considerable amounts of mass in the dust shells and hence significant scattering only.

Chapter 2

The MESS Project

As presented in the last chapter, there were numerous observations carried out in the past already, aimed at studying AGB-stars and their environments in particular. While instruments observing in the optical and radio or sub-mm wavelength range could provide quite high angular resolution (in the case of the longer wavelengths via interferometry) in the past, the facilities for the infrared regime had limited capabilities in this respect. All of the IR-space observatories launched so far – *IRAS*, *ISO*, *Spitzer* and *AKARI* – suffered from the comparatively small sizes of their telescope mirrors, restricting the achievable angular resolution, especially in the far infrared domain where the cold circumstellar dust component is emitting. Therefore, the geometry and morphological structures of the dust surrounding the stars remained hidden and with them essential information that would help solving open questions about the mass-loss phenomenon.

With the launch of the *Herschel Space Observatory* (Pilbratt et al. 2010) on May 14, 2009, a new instrument became available to the astronomical community, that with its capabilities should enable a more detailed look into the cold circumstellar environment for the first time. To make use of this opportunity the *MESS* project (Groenewegen et al. 2011) was initiated.

2.1 MESS

The *MESS* (which is the abbreviation of Mass-loss of Evolved StarS) project is a guaranteed time (GT) key program (KP) on board the *Herschel* satellite. Involved are PACS GT holders from Belgium, Austria and Germany, the *SPIRE Specialist Astronomy Group 6* and contributors from the *Herschel Science Centre* and mission scientists.

One of the aims of this collaborative effort is to better understand the time evolution of the mass-loss rate. Also, the geometry of the mass-loss process and its influence on the shape and appearance of nebulae that are found around Luminous Blue Variables (LBVs) and Planetary Nebulae (PNe) is investigated. The program also tries to improve the understanding of the interaction of these stellar winds with the ISM. Further questions concern the formation of various dust species at different locations in the circumstellar environment, the physical and chemical reactions that are responsible for the emergence of mass-loss and their dependence on the chemical composition of the photosphere.

To gather the necessary data, a total of about 300 hours of observing time with the *Herschel* Telescope was granted, using the *PACS* (Poglitsch et al. 2010) and *SPIRE* (Griffin et al. 2010) instruments. Thereof, 170 hours are photometric measurements, the remaining time is spectroscopy. The target list contains a large, representative sample of different post-main-sequence objects, like AGB-stars, Red Supergiants, post-AGB

objects, PNe and also massive stars and Supernova remnants. Concerning the AGB subsample, the candidates were chosen in a way such that all spectral classes (M-types, S-stars, carbon stars), variability types (L, SR, Mira) and mass-loss ranges (from low to high ML-rates) were covered. Another criterion for the selection of a target was the absence of high background emission, which was done by considering the *IRAS* CIRR3 flag.

2.2 The Herschel Space Observatory

The Herschel Telescope was launched successfully aboard an Ariane 5 ECA rocket (together with the *Planck* satellite from the Guiana Space Centre, French Guiana, in May 2009. The first proposal to ESA dates back almost 30 years, then called *Far InfraRed and Submillimetre space Telescope* (FIRST) in 1982. After a feasibility study it then became part of ESA's *Horizon 2000* long term plan (Longdon 1984) as one of the four "cornerstone missions".

The initial mission concept, which envisaged a 3-meter telescope with two science instruments in an approximately 24h highly eccentric orbit around Earth was modified, incorporating the experience gained from the ISO mission. The orbit was eventually changed to be a Lissajous orbit around the 2nd Lagrangian point (L2) in the Sun-Earth system, 1.5 million kilometres away from Earth. Also, the mirror size was slightly enlarged and three instead of two instruments were chosen for the science payload. Another design modification concerned the cooling concept, where a superfluid helium cryostat was employed, replacing mechanical coolers.

In 2000, FIRST was renamed *Herschel*, in honour of Sir William Herschel, who discovered infrared radiation 200 years earlier in 1800.

The Herschel mission was designed to be operated as an observatory facility – consisting of the satellite itself and a ground-based segment, responsible for the mission and science operations – providing at least three years of routine science observations, limited by the available amount of liquid helium coolant.

The Spacecraft

Two major components constitute the Herschel spacecraft (see also Table 2.1), which has to handle tasks such as pointing the telescope, executing the observing time line, on-board data handling and communication with the ground segment: the payload module and a service module. The payload module consists of the telescope with its 3.5 meter primary mirror and the cryostat, containing all the science instruments. The instruments sit on top of the tank (having a nominal capacity of 2367 litres) that comprises the liquid helium which keeps the individual components at the required temperature levels. The telescope on the other hand (for details see Table 2.2), having a classical Cassegrain optical design and being almost entirely made of silicon carbide, is not actively cooled. Its mirrors have an aluminum layer and thin protective coating. Furthermore, in-flight adjustments such as focusing are not possible due to the chosen design.

In contrast to parts of the science payload, the components of the service module do not require extensive cooling, although some need a thermally controlled environment.

These systems are needed for tasks such as the generation, storage and distribution of electric power. They also handle the attitude and orbit control by taking measurements with star trackers, gyroscopes and Sun sensors and if necessary carry out corrections using reaction wheels and hydrazine thrusters. Further functionalities of the service module electronics include the data management and communication with the ground station (sending data, receiving commands).

To prevent additional heating caused by solar radiation, the entire spacecraft is protected by a sun shield/sunshade, which also holds off Earth's straylight. While the upper backside of the shield is coated with a highly reflective foil, the lower part is equipped with solar cells that supply the spacecraft with electric power. The attitude control system maintains the orientation of the baffle in direction of the sun.

Height/width	7.4/4.0 m
Mass wet/dry	3400/2800 kg
Power total/science instruments	1200/506 W
Science data rate (max. average)	130 kbps
Absolute pointing (68%)	$\sim 2''$

Table 2.1: Spacecraft main characteristics, figures from Pilbratt et al. (2010).

Primary physical/effective diameter	3.5/3.28 m
Secondary diameter	30.8 cm
System/primary f-number	8.70/0.5
Angular resolution	$\sim 7'' \times (\lambda_{\text{obs}}/100 \mu\text{m})$
Operational temperature	$\sim 85 \text{ K}$

Table 2.2: Telescope main characteristics, figures from Pilbratt et al. (2010).

Instruments

The science payload of the Herschel satellite contains three instruments, which together are capable to perform spectrometry and imaging spectrometry in the range between 55 and 672 μm and can provide six bands at 70, 100, 160, 250, 350 & 500 μm for imaging photometry. Various observing modes are available, suiting the different needs for point sources, large area imaging, single spectral line studies or observation of one or more spectral ranges. The instruments (details are given in Table 2.3) are provided by consortia of institutes:

- Photodetector Array Camera and Spectrometer (PACS, Poglitsch et al. (2010))
- Spectral and Photometric Imaging REceiver (SPIRE, Griffin et al. (2010))
- Heterodyne Instrument for the Far Infrared (HIFI, de Graauw et al. (2010))

HIFI	Heterodyne spectrometer
Wavelength coverage	157–212 & 240–625 μm
Spectral resolving power	typically 10^6
PACS	2-band imaging photometer
Wavelength coverage	60–85 or 85–130, 130–210 μm
Detectors	64×32 & 32×16 pixel bol. arrays
PACS	integral field spectrometer
Wavelength coverage	55–210 μm
Spectral resolving power	1000–4000
SPIRE	3-band imaging photometer
Wavelength bands ($\lambda/\Delta\lambda \sim 3$)	250, 350, 500 μm
Detectors	139, 88 & 43 pixel bol. arrays
SPIRE	imaging fourier transf. spectrometer
Wavelength coverage	194–324 & 316–671 μm
Spectral resolving power	370–1300 (high) / 20–60 (low)

Table 2.3: Overview of the science instruments, figures from Pilbratt et al. (2010).

Comparing Herschel’s capabilities to earlier infrared space telescopes such as IRAS, ISO, Spitzer and AKARI, shows that not only the larger telescope (Herschel’s 3.5 m mirror is actually the largest of all space telescopes to date) and thus the increased angular resolution at already explored wavelengths is a significant improvement. In fact, especially with the SPIRE and HIFI instruments Herschel grants access to the until now comparatively unexplored far infrared and submillimetre domain of the electromagnetic spectrum, for both photometric and spectroscopic research.

2.3 The Photodetector Array Camera and Spectrometer (PACS)

The work presented in this thesis is based mainly on imaging photometry data from the PACS instrument. Since it is helpful for an efficient, target-oriented processing (see section 2.4) and analysis of the retrieved observational datasets to know about the design, specifications and functionality of the used hardware, a brief description thereof is given in the following.

2.3.1 Instrument Setup

Like SPIRE, the PACS module, cooled down to 3–5 K, houses an imaging photometer as well as an integral field spectrometer – the layout of the Focal Plane Unit is depicted in Figure 2.1. Both sections share the optically separated front optics compartment, which contains two calibration sources (gray-bodies) and a chopper. The chopper allows switching between the field of view on the sky ($3.5' \times 1.75'$ for the photometer & $0.8' \times 0.8'$ for the spectrometer, respectively) and the calibrator fields ($3.5' \times 3.0'$). The calibrat-

ors provide far-IR radiation at two slightly different levels but similar to the telescope background, mainly caused by the mirror having a temperature of ~ 80 K.

A field splitter then guides the light either to the photometer or the spectrometer section. Inserted in the optical path of the photometer, a dichroic beam-splitter separates the light into a long-wavelength (also called “red”) and short-wavelength (“blue” or “green”) channel, where the separation wavelength is at $130 \mu\text{m}$. Eventually the light is projected on the corresponding bolometer arrays which are 32×16 (red) and 64×32 (blue, green) pixels in size, respectively. Moreover, they provide full sampling of the telescope point spread function (i.e. diffraction/wavefront error limited). Because of different magnifying factors they share the same field of view ($3.5' \times 1.75'$). This results in a projected pixel size of $6.4'' \times 6.4''$ and $3.2'' \times 3.2''$ on the sky, respectively. For the short-wavelength detector one has to choose via a filter wheel the photometric band (blue: $60\text{--}85 \mu\text{m}$, green: $85\text{--}130 \mu\text{m}$) to be observed simultaneously with the long-wavelength array ($130\text{--}210 \mu\text{m}$)(see also Figure 2.2). This parallel way of observation has also the advantage of increasing the observing efficiency.

Since the spectrometer part of the PACS instrument was not used for this work, it is not presented here. A detailed depiction is given in Poglitsch et al. (2010), for example.

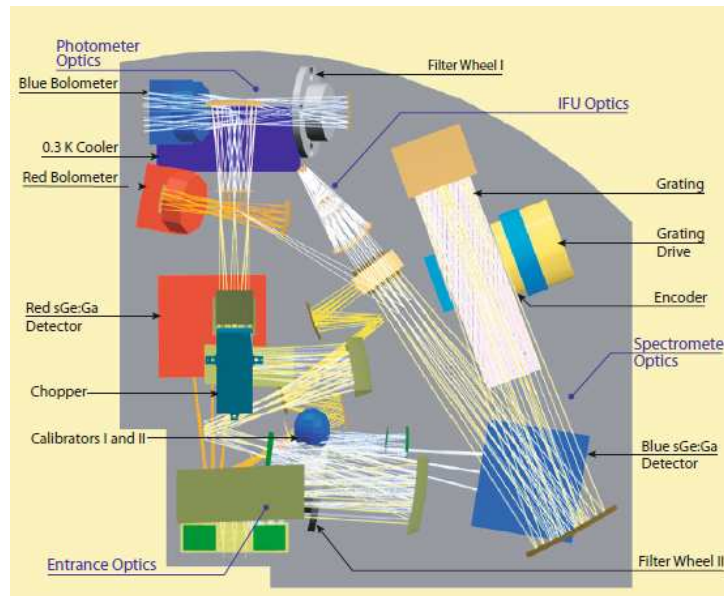


Figure 2.1: The PACS Focal Plane Unit. Shown are the elements and light paths for both the photometer and spectrometer. Taken from Poglitsch et al. (2010).

The bolometer arrays are built up of monolithic sub-arrays, combining 16×16 pixels. The gaps – about the size of one pixel – between the tiles need to be filled by applying appropriate mapping techniques. Whereas the whole bolometer assembly is kept at a temperature of ~ 1.65 K, the individual sub-arrays are operating thermally isolated at 0.3 K. ^3He was chosen as the cooler because unlike ^4He it does not become super fluid below 2.2 K and is also the better coolant. The cooling mechanism was designed to allow for an uninterrupted bolometer operation of at least two days, after which recycling would

be required. As in-flight measurements show this prerequisite is met easily (Poglitsch et al. 2010).

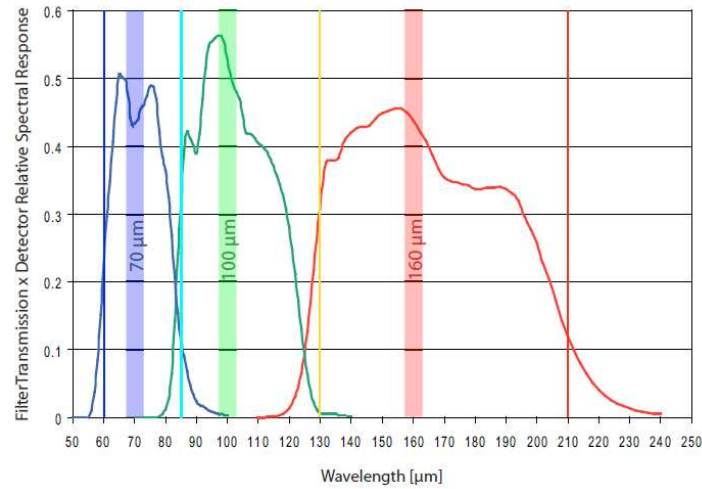


Figure 2.2: Effective spectral response curves of the filter/detector combinations for the PACS photometric bands (Poglitsch et al. 2010).

2.3.2 Observing Modes

To deliver the optimal observational results for the manifold astronomical targets and suit specific observer's demands, the PACS photometer provides three observing modes, also called *astronomical observing templates* (AOT):

- the point-source photometry mode (chopping & nodding technique)
- scan map mode
- PACS/SPIRE parallel scan map mode

Before any observation starts, calibration measurements are taken. Therefore, the chopper switches between the two calibration sources. In each observing mode the short- (where the observer can choose between the blue and green filter) and long-wavelength bolometers are read out simultaneously at a rate of 40 Hz. However, this is not the sampling frequency the observer obtains with his dataset. Due to the satellite's limited downlink bandwidth – it is approximately 1.5 million kilometres away from ground controls after all – the Signal Processing Unit averages four consecutive frames (eight in the case of PACS/SPIRE parallel observations), leading to an effective sampling rate of 10 Hz. To further reduce the transfer time, compression additionally shrinks the data-size. The software that takes care of this on-board data reduction was developed by members of the Institute of Astronomy at the University of Vienna and the TU Graz in Austria (Ottensamer & Kerschbaum 2008). In turn guaranteed observing time was granted.

The observations this thesis is based on, were all taken using the scan technique. It is adequate for capturing small maps as well as for imaging large areas of the sky (e.g. when conducting extragalactic surveys), which is probably one of the reasons that this is the most frequently used observing method with PACS.

Performing a scan means that the telescope is slewed along parallel tracks at constant speed (see schematic in Figure 2.3) – the observer can choose between slew rates of 10, 20 or $60''/s$ – while the detectors are read out at the sampling frequency. The number and orientation of scan legs as well as their length (no more than 20 degrees) can be set by the user in order to cover the desired area. Also the separation of the legs can be changed to adjust the overlapping of the individual scan lines – the maximum distance allowed is $210''$, corresponding to the long side of the bolometer array. To improve the coverage and thus the signal to noise ratio of the map the scan pattern can be repeated multiple times.

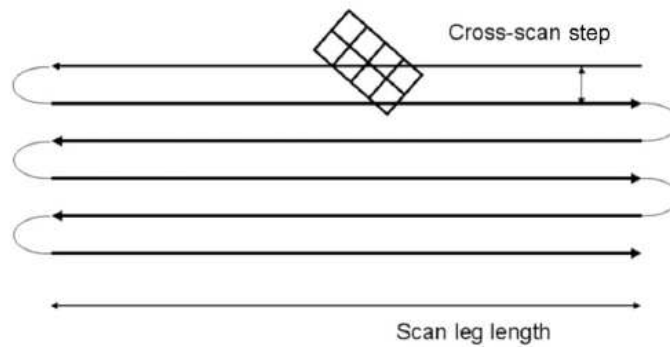


Figure 2.3: Slewing pattern of the scan map mode, taken from Poglitsch et al. (2010).

2.3.3 Photometer Performance

During the performance verification phase of the Herschel mission an extensive check up was carried out in order to find potential deviations of the actual in-flight performance from ground measurements and calculations.

Point Spread Function

PACS photometer optics provide diffraction limited images in all photometric bands ($70, 100, 160 \mu\text{m}$) – the Strehl ratio is $> 95\%$ – so the PSF is dominated by the telescope. As can be seen in Figure 2.4 the PSF has a bright circular core, which becomes a bit elongated in the $160 \mu\text{m}$ band. Caused by the secondary mirror's support structure and an imperfect mirror shape, the PSF also shows a tri-lobe pattern attached to the centre. When fast scan speeds are used (e.g. $60''/s$) the PSFs become smeared in all bands, for quantitative results see Table 2.4. Additionally, in a final map the point spread function will smear out even more, due to the averaging of frames (40 Hz to 10 Hz) and telescope pointing instabilities.

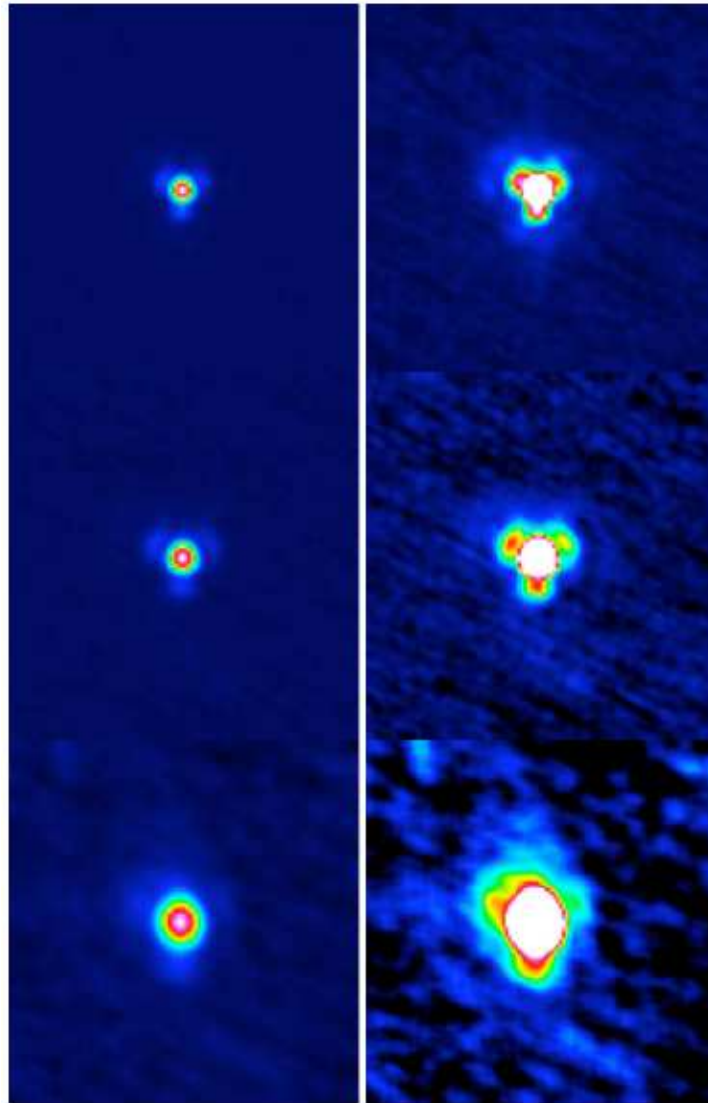


Figure 2.4: PACS photometer PSF for the blue, green and red channel (top to bottom). Left-hand panel shows linear scale, on the right-hand side the cut is set to 10% of the peak brightness. Scan speed is $10''/s$ (PACS ICC 2010).

Band	Speed ("/s)	FWHM (")	PA (°)
blue	10	5.26×5.61	
	20	5.46×5.76	
	60	5.75×9.0	62.0
green	10	6.57×6.81	
	20	6.69×6.89	
	60	6.89×9.74	62.0
red	10	10.46×12.06	7.6
	20	10.65×12.13	9.3
	60	11.31×13.32	40.9

Table 2.4: FWHM values at different scan speeds, measured by fitting 2D Gaussians to the PSF. The scanning angle was 63° (PACS ICC 2010).

Sensitivity

The passively cooled telescope mirror with a temperature of ~ 80 K is the main source of thermal noise and therefore, together with the readout noise, limits the sensitivity of the instruments. As an example, Table 2.5 shows point source sensitivities, derived from science observations. It has to be noted that the achieved sensitivity is highly depending on the processing of the raw data. The parameters chosen for the observation (scan) influence the outcome, too.

Band	Point source: $5\sigma/1$ h	Scan map: $5\sigma/30$ h
blue	4.4 mJy	3.7 mJy
green	5.1 mJy	3.7 mJy
red	9.8 mJy	3.7 mJy

Table 2.5: Point source sensitivity. In scan map mode, a $10' \times 15'$ area was scanned (Poglitsch et al. 2010).

Furthermore absolute photometric uncertainties were determined by point source observations of several targets. They turn out to be 10% in the blue/green and 20% in the red photometric band, respectively (Poglitsch et al. 2010). These values, however, were valid in the early mission phase only and have improved with time, as the quality of the calibration has advanced. Currently, the errors are about 5% and 10%, respectively.

Astrometric Accuracy

For pointed observations Herschel has an absolute pointing accuracy of $2''(1\sigma)$, whereas in scan map mode deviations as large as $5''$ can occur (PACS OM 2011). This causes additional smearing of the PSF, while the typical jitter along the scan legs ($\sim 1''$) doesn't greatly deteriorate the result further.

2.4 From Raw Data to the Final Map

Observing from space and in the far infrared is a demanding task, hence sophisticated techniques have to be applied in order to get useful results. As a consequence, the data collected by Herschel's instruments is quite complex and requires a considerable amount of processing. This section outlines the necessary reduction steps and describes the difficulties encountered while working with the PACS photometer products.

The Herschel raw data – where *raw* means the already on-board averaged data – is first being processed systematically to various degrees by the Herschel Science Centre and then made available through the *Herschel Science Archive* (HSA) as standardised products. Depending on the already performed reduction/correction steps, the provided products are assigned one of the following levels:

- **Level 0:** this is the data as received from the telescope, with minor manipulation from the HSC applied
- **Level 0.5:** AOT independent to this point, basic unit conversions have been done, also, masks for e.g. saturated or bad pixels have been created and added
- **Level 1:** after some final calibration steps the data can be considered as instrument and observatory independent. Until here the procedure shouldn't deviate much from the standard pipeline.
- **Level 2:** the path from level 1 to level 2 data highly depends not only on the used instrument mode, but also on the nature of the object (e.g. point source, extended emission) observed. Basically, the individual frames are mapped onto a final image, which then can be scientifically analysed.
- **Level 3:** this product level is not initially provided by the HSA. Level 3 data can be results from Herschel observations combined with theoretical models or other observations or catalogues. It is expected that such products will be loaded into the archive by the community, making them available for all users.

For each conducted observation, uniquely identifiable via the *observation ID*, all level products are accessible (except level 3) right away, without any further processing required by the user. While the automatically pipeline-generated level-2-map allows for a quick inspection of the observed target, the quality of the reduction is usually too poor for a comprehensive scientific analysis. Especially in the case of most of the objects observed in the course of the MESS program, whose nature calls for special treatment, an adapted procedure starting from the level 0 data is inevitable.

To provide an appropriate environment for the work with all Herschel data, the *Herschel Interactive Processing Environment* (HIPE)¹ was developed. It can be controlled using a GUI as well as by *jython*-commands and offers, besides the data processing routines, functionalities for extensive analysis of the results. It further provides the basic pipeline scripts, suiting the various AOTs and accounting for different target characteristics. The individual processing steps and the whole pipeline have been improved

¹HIPE is a joint development by the Herschel Science Ground Segment Consortium, consisting of ESA, the NASA Herschel Science Center, and the HIFI, PACS and SPIRE consortium members.

with time, but because first data reduction was performed early into the Herschel mission (during the Science Demonstration Phase (SDP)), the back then available pipeline scripts did not satisfy the individual requirements and were hence used as a starting and reference point for the reduction chain only (see Appendix A.1).

2.4.1 Calibration of the Dataset

Once an observation is obtained and loaded into HIPE, one can recognise the basic structure of the Herschel data. The actual observation is stored in a data cube, which contains the individual bolometer *frames* in a readout sequence. These frames are available at the already mentioned levels of reduction progress. Apart from that, there are also the calibration files and some auxiliary content. The calibration files include the instrument characteristics, such as the flat field and detector responsivity. They are not measured with each observation but are rather updated from time to time as the knowledge about the instrument behaviour advances. The auxiliary products provide further information recorded by the satellite during the observation and are mostly astrometric readings (e.g. pointing information, orbit ephemeris). Additionally, a *quality* section informs about possible troubles during the observation or the pipelining process. All of the measurements taken for the MESS guaranteed time key program were carried out using the scan map mode of the PACS photometer. Therefore, the principle structure of the dataset is identical for all of the targets in the sample, as well as the applied processing routines.

The Path to Level 0.5

After all of the above products needed for the reduction are loaded, one starts with identifying the various parts – so-called *blocks* – of the observation. At first, a task recognises the beginning of the observation, where the telescope slews to the starting point of the scan. Before the actual observing of the target starts, the chopper switches between the two calibrators next to the field of view of the sky, providing a calibration signal. When this sequence is completed the scanning of the determined area begins. For very large scans the observation of the sky can be interrupted by another calibration block. The different parts of an observation can be illustrated by plotting the signal of the bolometer as a function of time (i.e. read outs). Figure 2.5 shows the signal from a single pixel of the blue PACS bolometer array, where the phases of the observation run are clearly distinguishable. The task further differentiates between the scan directions and identifies the turnarounds from one scan leg to another. Finally all the detected blocks are labelled in a human readable manner.

As a next step, based on the block labels and additional instrumental status parameters (these are necessary because it turned out that the labels alone don't provide reliable identification of the calibration block), the whole calibration block is removed from the frames. The calibration data is not used further in the reduction procedure. Early into the Herschel mission the recognition of the calibration sequences was not very precise, making manual corrections necessary. Also, some early observations contained unintended calibration blocks during the observations (e.g. between repetitions), which were not removed properly and also required adjustments by hand.

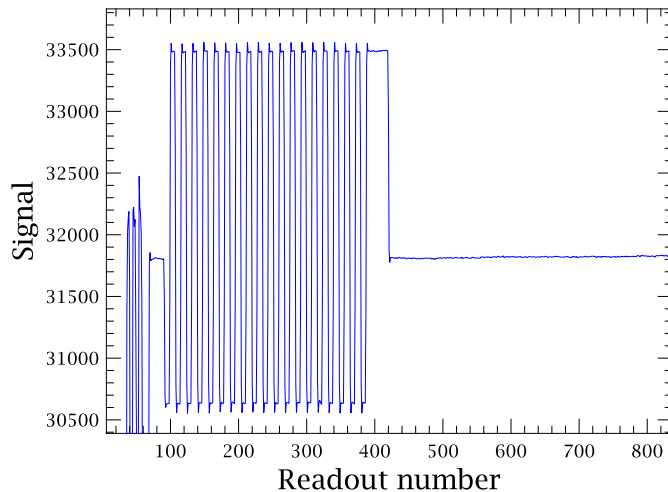


Figure 2.5: The readout signal (in instrumental units) of a single blue PACS photometer pixel as a function of time. Preceding the apparently smooth scan part (which is just due to the magnification factor) the signal jumps between two levels, corresponding to the two slightly differing calibration sources. This part is removed before any reduction steps are taken.

The blue and red bolometer arrays consist of 2048 and 512 pixels, respectively. Since the detector parts and technology are very sensitive, it comes as no surprise that not all of the individual elements function without flaws or at all. Some pixels are known to be dysfunctional prior to launch. Additionally, the rough phase during take-off and simply ageing of the hardware are responsible for detector array elements not functioning properly (see Figure 2.6). These malfunctioning pixels have to be identified and must not be considered for the following calculations. Instead of simply removing the peculiar datapoints, masks are created, assigning every read out pixel a *good* (“0”) or *bad* (“1”) flag concerning the checked criterion. Thus a pixel can be both masked or unmasked and correspondingly being taken into account for a specific calculation or not, depending on the type of mask adopted by the task. For instance, a *badpixel* mask is created which flags regions of the array that show unusual behaviour (i.e. are very noisy) or cannot detect a signal at all (dead pixels). The created mask is then valid for the whole frames sequence and the flagged pixels are not considered for the final map projection.

Apart from the *bad pixels*, areas that are saturated have to be masked out, too. The according task can check for two kinds of saturation: one comes from the readout electronics, while the other is due to the A/D converter. Based on either one of the two or both origins upper and lower saturation limits are calculated and the pixels showing exceeding readout values are marked.

Usually, the steps conducted so far get hold of all the array segments behaving erroneously. However, some observations still show anomalies after the corrections and therefore require some individual expansion of the calculated masks. A possible cause for the rarely occurring peculiarities are cosmic ray hits which can temporarily severely

influence the characteristics of single bolometers or even whole subarrays, which eventually results – although the glitch itself is getting masked/removed – in artefacts in the projected map.

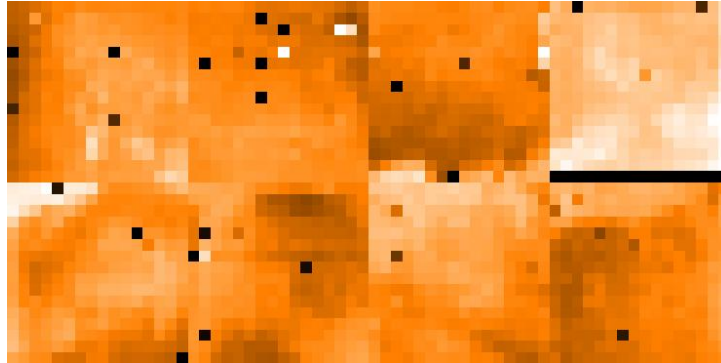


Figure 2.6: A single raw frame from the blue PACS bolometer array. The signal is dominated by the background (warm telescope mirror), making it impossible to identify even a bright source in this unprocessed image. Noticeable are the black pixels (mostly dead), most of which (also the whole line at the bottom of the upper rightmost subarray) have been *bad* from the beginning.

After the masks have been created, additional (minor) steps are performed to take the data product to level 0.5. In order to get calibrated figures, the readout values, which are still given in A/D units, are converted to volts using the following equation,

$$signal[volt] = (signal[ADU] - offset) \times gain$$

where offset and gain are extracted from the calibration data. Following that, a task appends information about the initial noise of the bolometer pixels to the frames by either getting it from the calibration product or computing it using one of three provided methods. Further calibrations correct for the time difference between the satellite on board time and UTC on ground and calculate the chopper position angle with respect to the optical axis of the FPU and on the sky.

At this point in the pipeline it is suggested to clean the data from effects caused by cosmic rays that hit the bolometer. This is done by executing a task based on the multiresolution median transform (MMT) (Starck et al. 1999). The signal recorded by a pixel shows different characteristics whether it is due to the target source or a glitch. By analysing the temporal evolution of the signal (unlike a real object, a glitch usually appears in one or two readouts only) – particularly the noise properties – and applying the MMT technique, the glitches are identified and masked/removed. For observations of faint point sources such as deep fields this method is expected to perform well. However, if the dataset contains bright objects – which is the case for most of the MESS targets – it turns out that the algorithm also removes parts of the core of the source (see Figure 2.7), thus distorting the photometry. To solve this problem the critical areas in the map could be masked and protected from being considered a glitch, although actual glitches within the mask then wouldn't be treated either of course. Moreover, observations that show

significant extended emission are problematical, too. Because in such cases the noise can't be determined correctly, the detection of cosmic ray hits doesn't work well and again parts of real sources are removed by mistake. Therefore it was decided not to use this method to free the data from cosmic ray effects. Instead, another approach – 2nd level *deglitching* (see Section 2.4.2) – was incorporated in the reduction process.

Before reaching level 0.5 pipeline stage, a first astrometric calibration is carried out. Using the pointing product and Spacecraft/Instrument Alignment Matrices (SIAM) from the auxiliary observation context, sky coordinates and the position angle are assigned to the virtual aperture (i.e. the centre of the PACS bolometer array) for each frame. While the pointing product passes along the information about the Herschel satellite pointing, the alignment matrices describe the position of the virtual aperture relative to the spacecraft orientation. Additionally, the astrometry can be corrected for aberration.

After going through all of the reduction steps above, which are all independent from the photometer observing mode (AOT), the data has level 0.5 status. There is, however, another issue that needs to be tackled before going on to the AOT specific processing. It has been noticed for both the red and blue bolometer array, that if a bright source is present in the rightmost column of a subarray, there is also a correlated signal detected in the leftmost column of that same subarray (PACS OM 2011). There is currently no task implemented into HIPE that could correct for that effect, known as *electronic crosstalk*. That is because the behaviour of this phenomenon doesn't seem to be easy to model, thus there is no straightforward way to mitigate the impact. Therefore, to prevent artefacts possibly hard to ascribe in the final image, all leftmost columns (indices 0, 16, 32 & 48) of both photometer arrays are masked out preemptively. That unfortunately also means throwing away 1/16 of the observation data, of course. Although clearly visible artefacts could be made out in a small sample of the processed observations only (see Figure 2.8 and Table 2.6), all targets were treated in this cautious manner, leading to a lower coverage of the observed area and a worse signal-to-noise ratio.

masked column indices	measured flux [Jy]	flux missing
no masking	0.120	45%
0	0.170	22%
0/32	0.181	17%
0/16/32	0.219	0%
0/16/32/48	0.219	0%

Table 2.6: Flux changes measured in the region most apparently affected by electronic crosstalk (see also Figure 2.8).

Level 0.5 to Level 1

At this processing stage the individual frames still suffer from flat field effects (see Figure 2.9). Also, in order to make the observation comparable to others and independent of the instrumentation, the signal (which is still in Volts) needs to be converted to a flux density and photometrically calibrated.

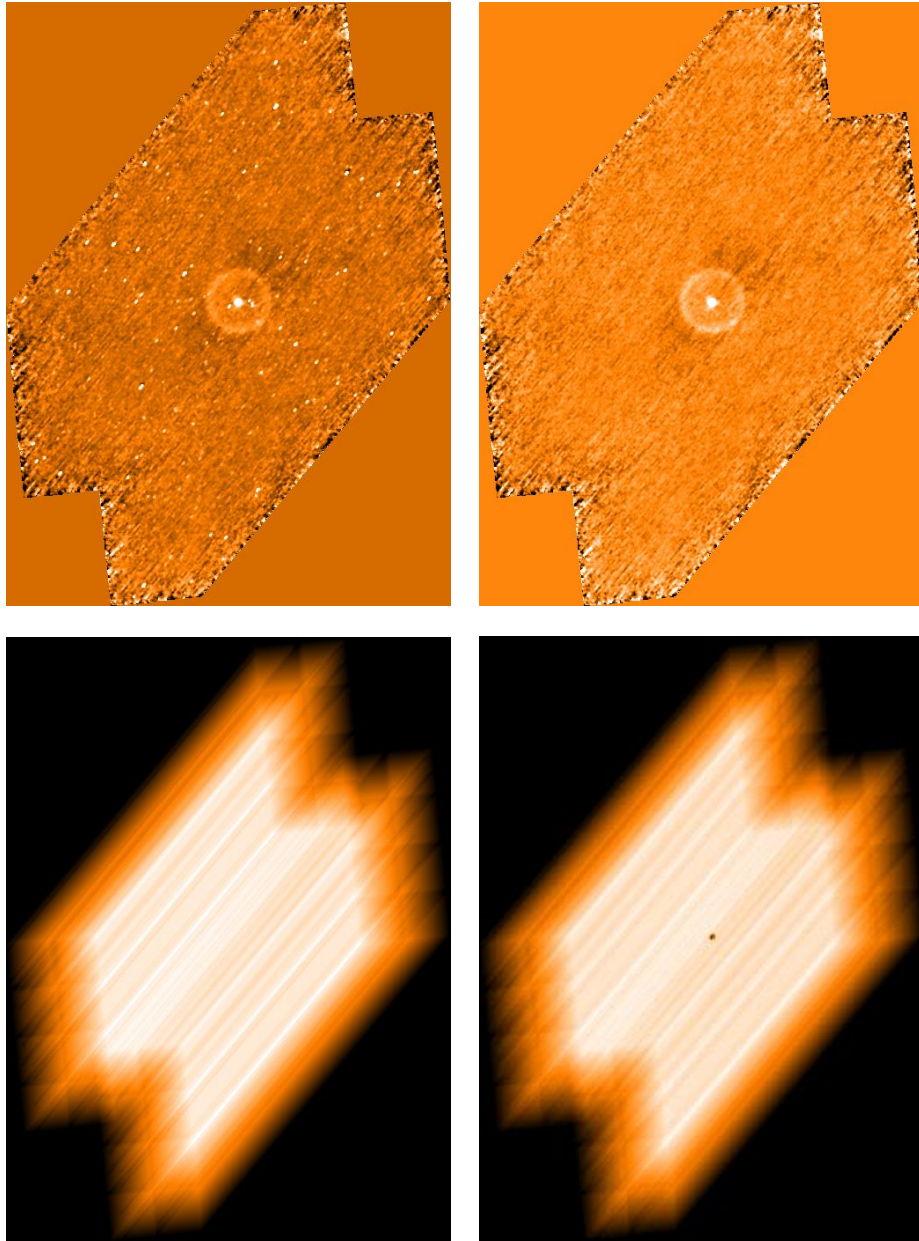


Figure 2.7: The top row shows a simple projection of one scan observation (carbon star TT Cygni), with no deglitching applied (left) and using the MMT algorithm (right). Clearly, the glitches are removed effectively. The corresponding coverage maps (bottom row) however, reveal the downside of this method in the case of a bright source (with extended emission in this case). The “hole” at the position of the star indicates wrongly removed parts of the signal.

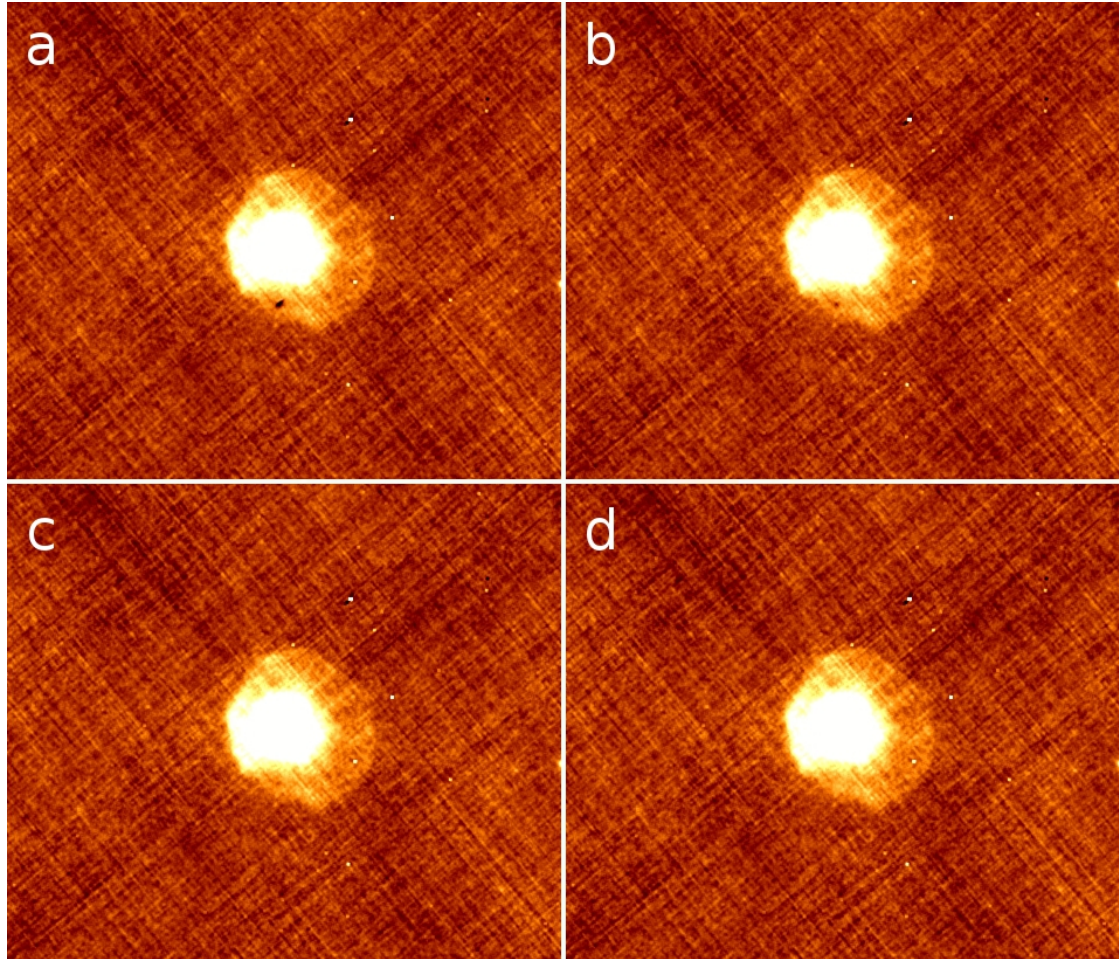


Figure 2.8: A sequence of scanmaps of the very bright source W Hydrae, showing the apparent impact of electronic crosstalk. The dark spot below the star as an effect of the phenomenon diminishes as the leftmost columns of the bolometer subarrays are successively masked out. Starting top left no column (a), column 0 (b), columns 0/32 (c) and columns 0/16/32/48 (d) are masked. For quantitative results see Table 2.6.

All these transformations are done following the formula

$$\delta f(t) = \delta s(t) \frac{1}{J\Phi},$$

where $s(t)$ is the input signal in Volt, Φ is the normalised flat field and the responsivity factor J that converts the Volt values to Jansky², yielding the calibrated output $f(t)$.

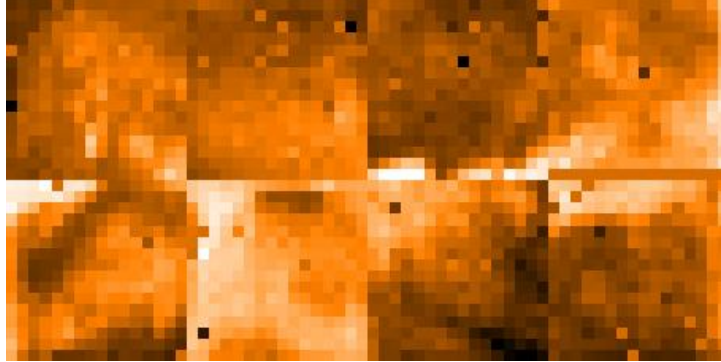


Figure 2.9: The flat field image used for calibration of the blue PACS bolometer array.

In order to map all the single frames onto a final image, the astrometric calibration carried out so far is not sufficient (only the coordinates and position angle of the array centre have been assigned to the frames). For an accurate projection the small misalignments and rotation of the bolometer elements have to be taken into account. Therefore, in a first step, the pixel centre coordinates have to be transformed into the PACS focal plane reference system using the supplied spatial calibration file. Then these coordinates are further transformed into an orthogonal local grid on the tangential sky plane. Approximated by polynomials, these values give the offset from the bolometer centre and eventually the centre of each pixel gets the proper right ascension and declination coordinates.

With the completion of this last task, the calibrated frames would in principle be ready to assemble a map of the sky. There are, however, still major effects present in the data that demand further processing, as is shown in the following section.

2.4.2 Mapping Techniques

The two PACS bolometer arrays show a large sensitivity drift in the course of an observation. Besides a drift of the whole detector array (shown in Figure 2.13) there is also a considerable offset between the individual pixel signal levels. The latter is due to the design of the instrument – since the PACS bolometers are multiplexed, only the mean signal values of modules (subarrays) can be set to zero which leads to the significant pixel-to-pixel variations. In fact, this effect dominates the pattern of each photometer readout. Additionally, the signal of a single pixel has a component caused by correlated noise ($1/f$). Without correcting for these effects no useful output can be produced. Depending on the selected mapping algorithm there are different approaches to handle the mentioned issues.

²1 Jansky [Jy] = 10^{-26} W Hz⁻¹ m⁻²

2nd level deglitching Since the nature of a typical MESS target does not allow for the MMT-deglitching technique (see Figure 2.7 on Page 43) to provide proper results, another method has to be used in order to free the data from glitches. For that matter HIPE has implemented an alternative solution, called *2nd level deglitching*. Unlike the MMT algorithm, which analyses the signal of a single detector pixel independently (thus working in the time domain), *2nd level deglitching* makes use of the redundancy of the observation data (i.e. a spot in the sky is covered several times by different bolometers due to the scanning motion, some overlapping of the scan legs and repetition of the scan path) and works in a spatial dimension. The assumption is that a pixel on the sky (map) contains contributions from several detector pixels. Of course, during the observation the signal from that area of the sky should remain constant – therefore any significant deviation from the average value can be considered a glitch. The deglitching task is basically a two step process. First, a so-called *Mapindex* is created which computes the flux contributions from the detector elements to each map/sky pixel. For every map/sky pixel a sigma-clipping algorithm then detects the outliers among the contributing signals and the corresponding detector elements are masked in the frames product.

To achieve optimal deglitching results the sigma clipping parameters have to be adjusted. In our case the use of median filtering (adopting a filter width of 20 elements and $\sigma = 15$ (median absolute deviation)) to detect both positive and negative outliers turned out to work well, not showing the flaws of the MMT technique.

Photproject

This is the simpler of two methods to assemble the final image provided by HIPE. Photproject just co-adds the individual frames resulting in a map of user-defined resolution. It neither takes care of the detector drift and pixel offset nor the $1/f$ noise. Thus a separate way to get rid of these effects has to be found. The standard procedure to mitigate all of them at once is to apply a highpass filter (HP) – from the signal time line of each pixel a moving median is subtracted. The median is calculated for every data point (i.e. readout) from a box having a user specified width. The quality of the output, however, strongly depends – again – on the structure of the processed object. Two drawbacks of this method necessitate special attention towards the filtering. For one, because of the principle of a highpass, structures larger than half the filter width are not preserved. Since the applied box sizes have to be rather small (compared to the dimensions of a typical scanmap) to efficiently remove the correlated noise, real extended emission will be removed from the signal. The other downside mainly concerns bright sources – in the vicinity of such an object the computed median is high, therefore the signal adjacent to the peak itself is over-corrected, resulting in artefacts before and behind (in scan direction) the object (Figure 2.10). Towards smaller filter widths the effect increases, as can be expected. To reduce the impact, the critical areas of the map can be masked, thus excluding the corresponding bolometer readouts from the median calculation. This is achieved by first HP-filtering the data (we used a box width of half the map size to not introduce additional artefacts) and then creating a preliminary map. For this map an average brightness value is calculated, in order to then mask all the parts that lie above a defined *n sigma* limit (see comparison in Figure 2.11). The masking information is then assigned to the unfiltered frames and the highpass task is run again.

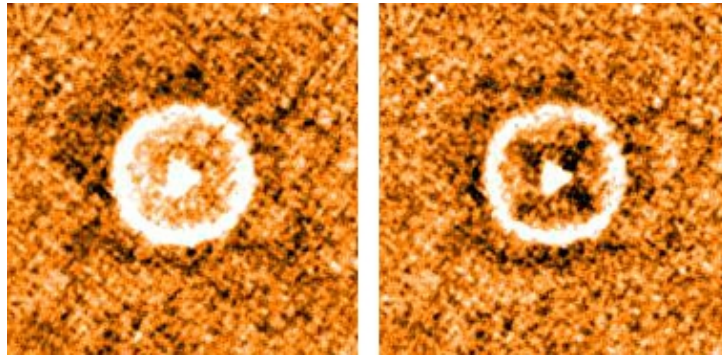


Figure 2.10: Artefacts introduced by the highpass filtering. Narrower filter widths intensify the effect. The applied box sizes are 60 (left) and 30 (right) readouts, which corresponds, taking into account the scan speed of $20''/s$ and sampling rate of 10 Hz, to 2 and $1'$ on the sky, respectively.

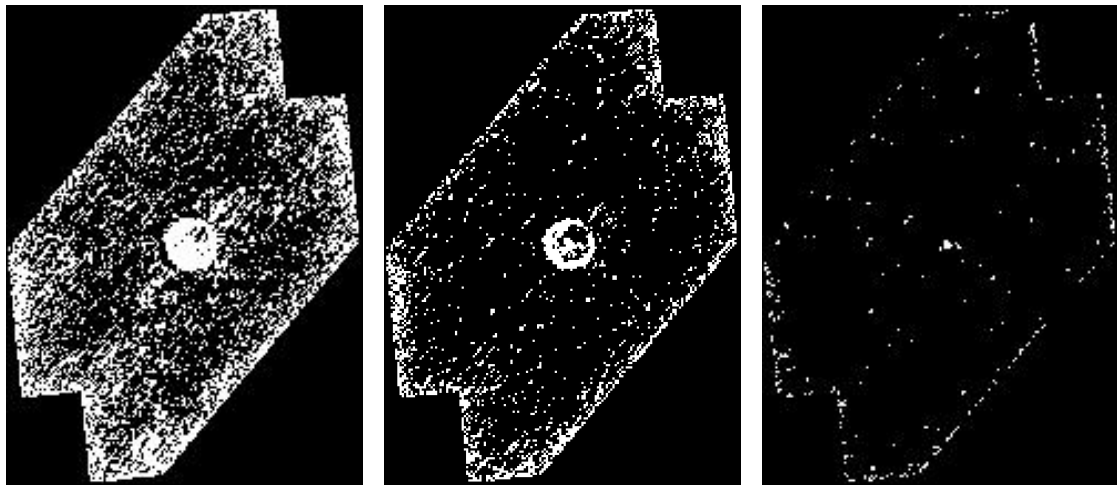


Figure 2.11: By choosing the n *sigma* value one defines how much of the map is masked and excluded from highpass filtering. Ideally, all bright parts of the source should be masked (centre). With a too low threshold (left) the drift and noise can't be removed effectively and the resulting map remains rather "striped", whereas images where too little has been protected from filtering (right) will still show the "shadow" artefacts.

The frames, which are now corrected for drift and to a certain degree depending on the selected HP filterwidth for $1/f$ noise, are mapped to an image, adopting the drizzling technique (Fruchter & Hook 2002). Figure 2.12 gives an overview of Photproject output maps where different HP and mapping parameters were used.

Comparing photometry measurements of differently processed maps shows a systematic dependence on the HP filterwidth. It appears that the filtering, despite the masking of bright sources, removes parts of the signal, where the loss of signal becomes more severe with narrow filters (measurements are given in Table 2.7). Therefore, if one is looking for an efficient removal of the “striping” artefacts due to the correlated noise while retaining reliable photometry, the highpass method plus Photproject mapping is not the ideal choice, at least for objects that have characteristics similar to those of the MESS project.

filterwidth [readouts]	flux
20	2.46 Jy
40	2.89 Jy
60	3.17 Jy
80	3.29 Jy
100	3.35 Jy
125	3.42 Jy
150	3.48 Jy
200	3.56 Jy

Table 2.7: Highpass filtering, despite the masking, also influences the photometry. Exemplarily the flux measured for TT Cyg in maps created using different HP filterwidths is listed.

MADmap

The second map making method incorporated into HIPE is the *MADmap* technique (Cantalupo et al. 2010). Based on the algorithm initially developed for mapping the data of the WMAP satellite, this method employs a maximum likelihood technique to eliminate the $1/f$ noise. It does not, however, correct for detector drift and will treat any systematic effects as real signal. Therefore the preprocessing approach is different from the Photproject case. Drift and pixel-to-pixel variations can be mitigated in a way that, opposite to the moving median, preserves the extended emission.

The most prominent effect – the variable individual pixel levels – can be treated in two ways. One is to simply subtract a *zero level image* that is provided from a calibration campaign. The other approach is to compute the median of the signal of a whole observation for each pixel and then subtract the accordant value. As it turned out, the latter method yields better results in the final map.

After this correction it can occur – for the blue detector only – that a pair of two submodules shows a systematic offset compared to the rest of the array due to a different drift. So before treating the global drift, the *module-to-module drift* has to be removed

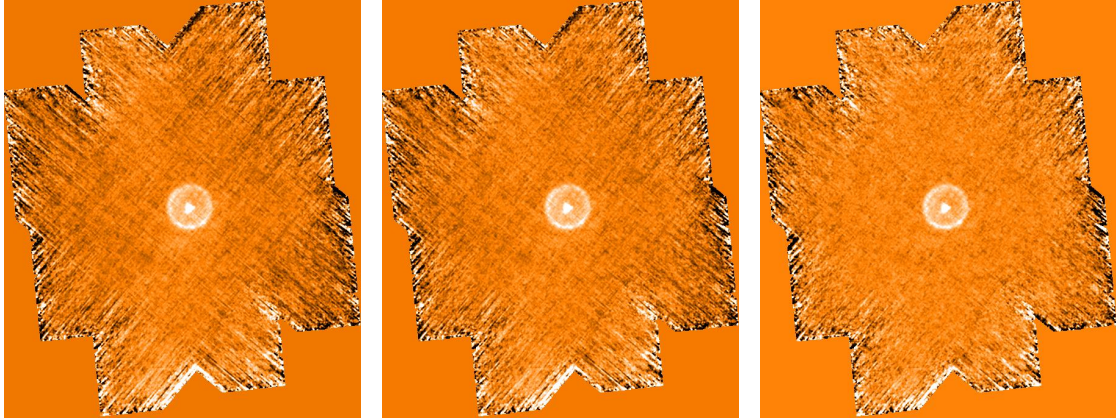


Figure 2.12: Photproject results, preprocessed using iterative highpass filtering, where bright regions have been masked. The final filter widths are, from left to right, 100, 70 & 30 readouts (corresponding to 200, 140 & 60'' on the sky, respectively) – a relatively smooth (i.e. stripe-free) background is only achieved with parameters, where the filtering already severely affects the photometry (cf. Table 2.7).

(e.g. by fitting a straight line to the drift of the submodule signal relative to a reference submodule and then subtract it from all the corresponding pixels). If one doesn't correct for this effect, the final image shows broad striped artefacts.

To avoid large scale gradients in the map, the considerable drift of the average detector signal has to be taken into account during preprocessing. The optimal method somewhat depends on the amount of extended emission present in the observation. First, the median of each readout frame has to be put as a function of time. In case the background is negligible (i.e. the median signal variation is therefore mainly caused by detector drift), it should suffice to fit a polynomial (usually a 2nd order one will do) through the datapoints and subtract the function from each pixel, thus removing the global drift. However, if the observed area contains considerable extended emission, it will contribute essentially to the signal shape. Therefore, prior to estimating the drift via a fit, one has to find the parts of the signal where it can be assumed that the background contribution is relatively small. This is achieved by taking the minimum value of a defined number of samples along the signal timeline and then fitting a function through the determined points (see Figure 2.13) which is then subtracted analogously to the former method. The goodness of this drift correction is crucial for the homogeneity of the background in the map.

After the preprocessing and ready for being MADmapped, a single frame should typically look like depicted in Figure 2.14, where it is possible to already identify bright sources. That snapshot also demonstrates the necessity of having thousands of frames put together to end up with images having unprecedented resolution and sensitivity.

Using the PACS *inverse noise time-time* correlation matrix (which describes the noise properties of the detector) from the calibration product, the MADmap algorithm removes the $1/f$ noise and produces the map. Compared to the highpass filtered Phot-

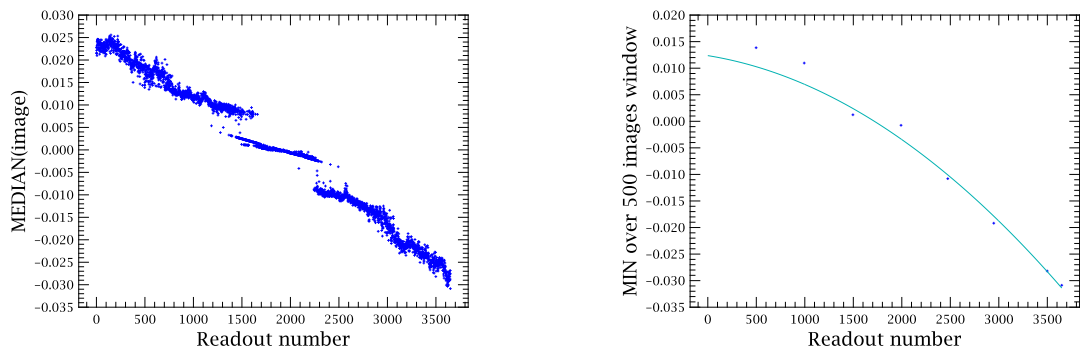


Figure 2.13: Left: the median signal of the whole bolometer array as a function of time (readouts). Right: the minimum values over a box size of 500 readouts, fitted by a 2nd order polynomial that models the global drift.

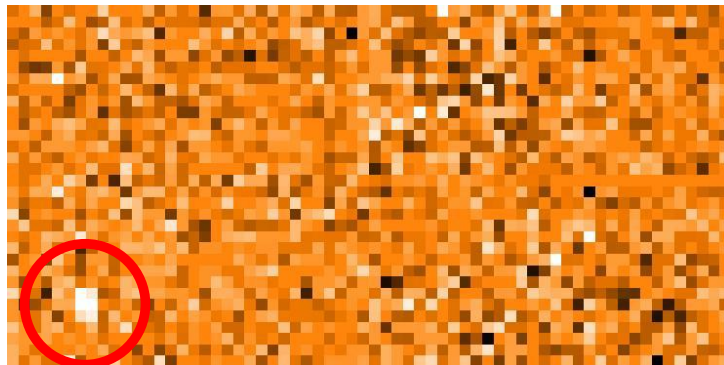


Figure 2.14: A single blue bolometer frame after the MADmap preprocessing. Once the pixel signal levels have been homogenised, bright sources become visible (red circle).

project output, there is no “striping” pattern left (cf. Figures 2.16 & 2.17) and because of the “smoothness” faint emission becomes more apparent. The technique suffers, however, from another artefact: bright sources show a dark cross attached to them (see Figure 2.15). The strength of the effect correlates with the source intensity, but is less apparent in maps with higher spatial sampling. So far the cause of that phenomenon is not well understood.

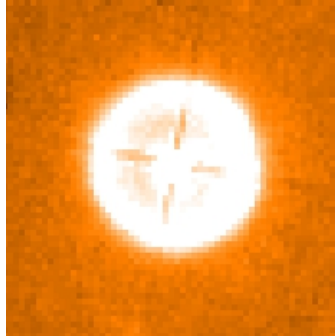


Figure 2.15: The cross artefact as it appears for bright objects in MADmapped images.

Scanamorphos

An alternative to the map making algorithms supported by HIPE is the *Scanamorphos* software³ (Roussel 2011). The external, IDL-based program is the most promising method so far. While it was developed for the Herschel photometers, it can be applied to scan observations with other bolometer arrays as well, as long as they are sufficiently redundant. Also, some basic instrument characteristics have to be known in order to adapt the routine. For input it requires level 1 data processed the usual way, i.e. frames after bad/saturated pixel masking, unit conversions, flux calibration and the astrometric information added. Scanamorphos takes care of both the low- and high-frequency noise present in the observation. Contrary to MADmap, it does not make use of an assumed noise model, but solely relies on the high redundancy of the PACS data, i.e. a spot on the sky is observed by many different bolometers several times, instead. Empirically determining the low-frequency noise would be a tricky task, since its power spectral properties are not easy to disentangle from those of extended emission, which is often present in PACS and SPIRE observations. Also, it does not make use of any filtering (e.g. highpass-filtering, as it is applied before Photproject mapping), which would remove noise as well as some actual extended emission.

Before any noise is corrected for, the Herschel data requires another preprocessing step. The individual bolometer signals show an offset that varies significantly from bolometer to bolometer (because of calibration uncertainties of a reference voltage value). The offset is removed by subtracting a constant baseline per scan leg for each bolometer. The low-frequency noise is dominated by two main components, namely the thermal drift and flicker noise. These sources are treated separately. The thermal drift, which is due to

³Available at <http://www2.iap.fr/users/roussel/herschel/>

temperature fluctuations of the cryogen, shows a strong correlation among all bolometers, hence an average time series can be calculated for the whole array. In an iterative fashion the difference between a linear baseline fit to this series and the linear baseline of a time series simulated from a reference map is subtracted. The drifts are removed on various timescales (scan, scan leg and shorter). Similarly Flicker noise is treated, although the correction is done individually for each bolometer. The treatment of the high-frequency noise includes white noise, discretisation, noise and glitches. Finally, the corrected data is projected onto a user-defined grid. Additionally, the output contains a weight map, an error map and a map displaying the removed low-frequency noise (drift).

A more detailed description of the calibration/mapping process and the principles behind it, as well as a brief user guide can be found in the cited paper. Briefly assessing the Scanamorphos maps one can say that they don't show any obvious artefacts, noise is adequately treated and faint emission is rendered well. A comparison to the results of Photproject and MADmap is depicted in Figures 2.16 & 2.17.

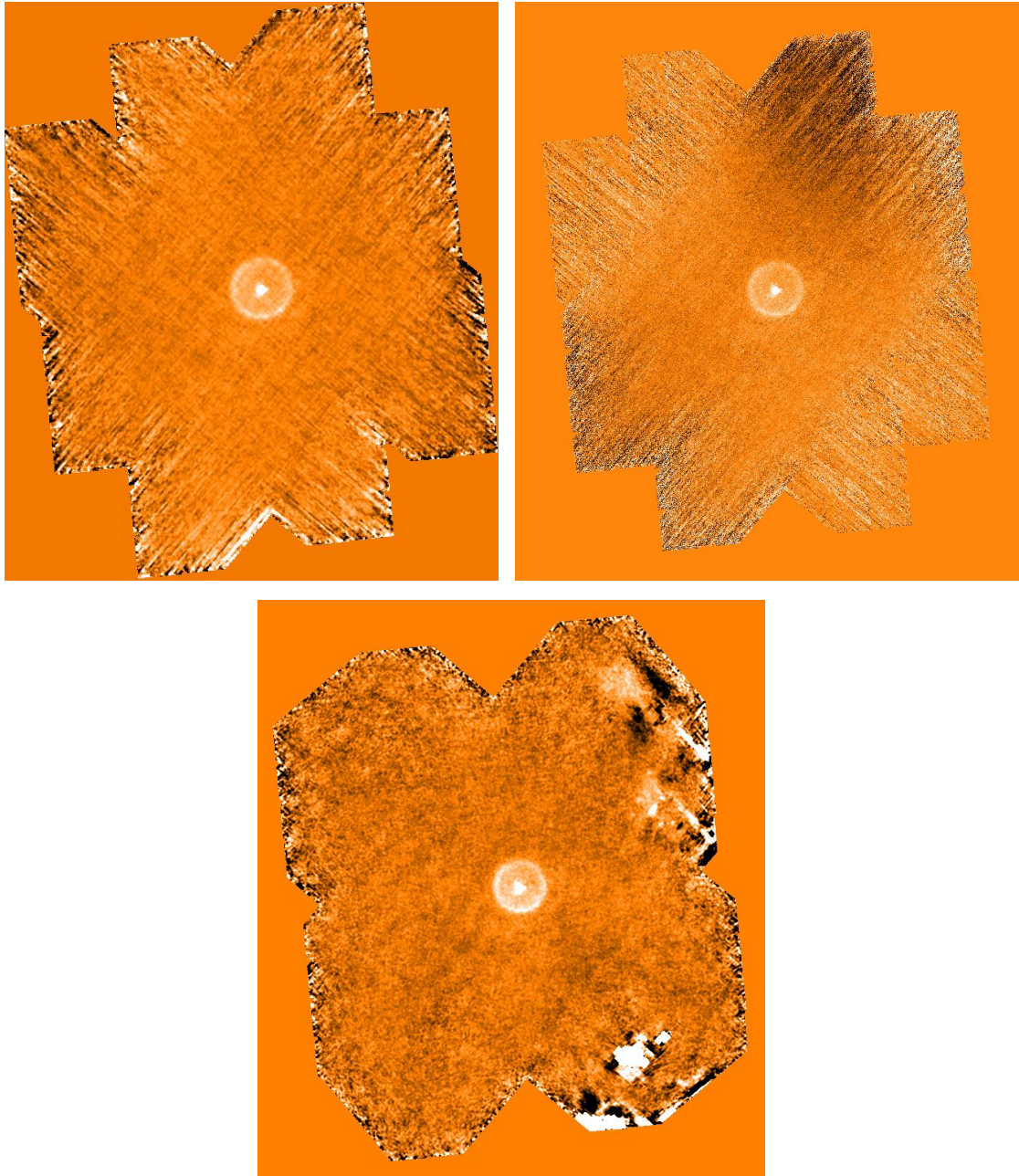


Figure 2.16: Overview of the three map making methods in the $70 \mu\text{m}$ band: Photproject (top left), MADmap (top right) and Scanamorphos (bottom). Compared to Photproject, the other two techniques show no “striping” or “banding” artefacts. The contrast of the MADmap, however, is relatively low (it is a function of map resolution – higher sampling leads to lower contrast).

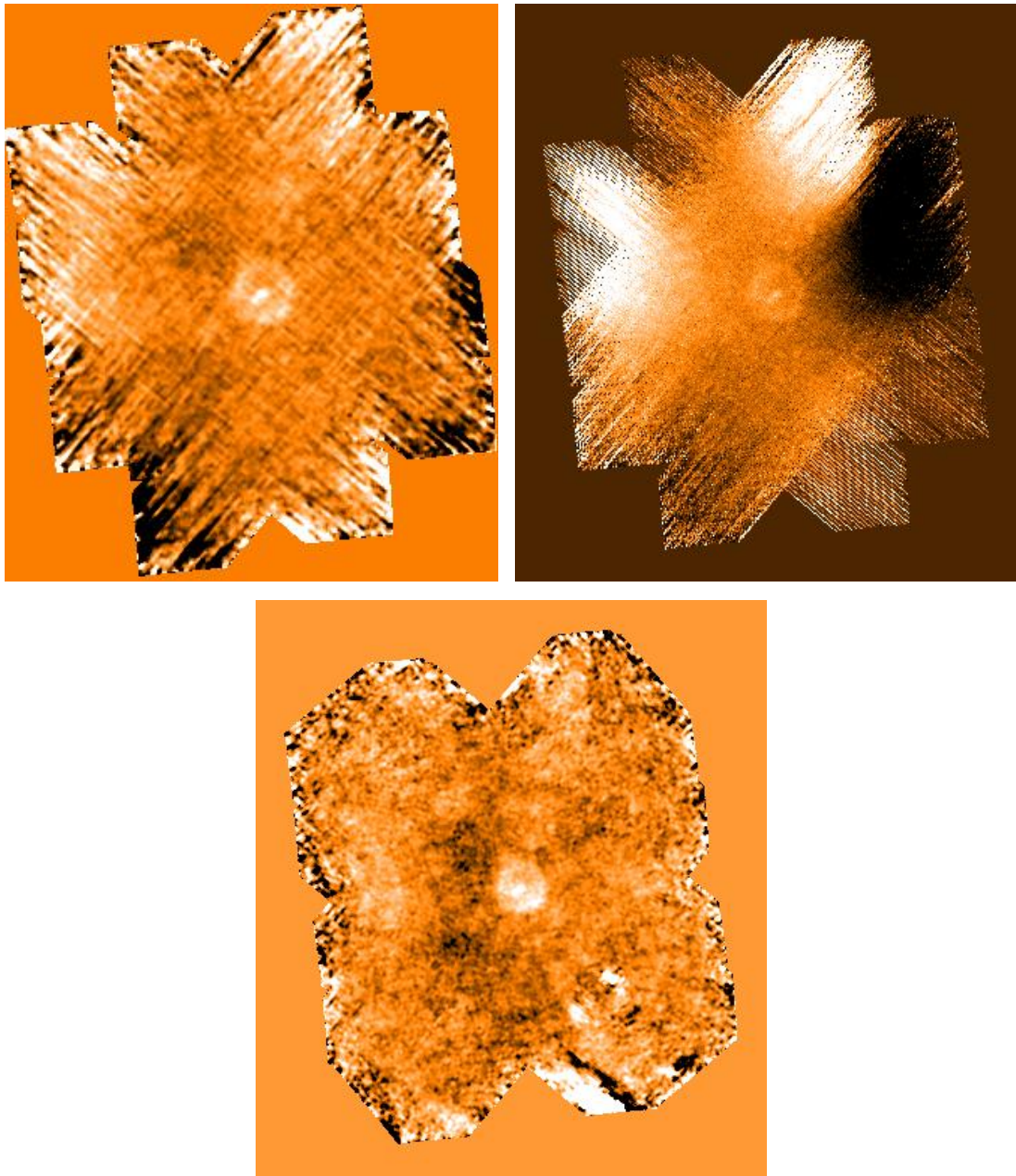


Figure 2.17: Photproject (top left), MADmap (top right) and Scanamorphos maps (bottom) at $160\ \mu\text{m}$.

Chapter 3

Analysis & Modelling

The characteristics of the *gas* component of circumstellar environments have been studied with high angular resolution for some time, using interferometric (sub)millimetre observations (e.g. Lindqvist et al. 1999; Olofsson et al. 2000). On the contrary, the Herschel space telescope and the PACS imaging photometer in particular, recently provide the opportunity to explore the morphology of the cold circumstellar *dust* environment in a manner not possible with earlier space IR missions such as IRAS and ISO, or even Spitzer and AKARI. The 70 and 160 μm scanmaps with their high resolution and sensitivity, obtained by adapted processing as described in Chapter 2, mark a sound starting point for scientific analysis.

The objects observed in the course of the MESS consortium show a wealth of shapes and geometries (cf. Cox et al. 2012). Among the various subcategories this work focuses on the morphological class of so-called *detached shell* objects, with the best studied and thus most prominent members of this group being S Sct (e.g. Groenewegen & de Jong 1994), TT Cyg (e.g. Olofsson et al. 2000) & U Ant (e.g. Maercker et al. 2010). Sources in this subsample all show a more or less symmetric ring-shaped structure surrounding the central star. Characteristically, the circumstellar emission is constrained to a geometrically thin region, i.e. $\Delta R \ll R$. Properties of such detached shells and circumstellar envelopes in general are discussed at length in several publications (e.g. Habing 1996; Habing & Olofsson 2004). In many cases the circular shape is highly symmetric, which makes a quantitative description of the object and a rough estimate of basic parameters rather straightforward. For example, by determining the angular size of the shells and using additional data from literature, the physical sizes and timescales were estimated – a detailed discussion thereof is given in Sect. 3.1. Furthermore, models of CSEs have been calculated for comparison in order to constrain some parameters (see Sect. 3.2). Based on the deduced quantities and morphological attributes different scenarios for the shell formation can be discussed.

3.1 Measuring CSEs

3.1.1 Profiles – Condensed Information

Azimuthally Averaged Radial Profiles (AARPs)

Dealing with rather symmetrical detached shell objects, there is more than one way to quantify the structures in the map. One of the more straightforward approaches to obtain the size (i.e. the diameter or radius of the ring shaped emission) is to calculate radial

profiles. In the case of very bright shells with a high signal-to-noise ratio it would usually suffice to simply plot the pixel values along a line through the shell centre – which, for some objects, doesn't necessarily coincide with the position of the star. For many targets, however, the circumstellar emission is rather faint, too weak to distinguish the structure as a feature from the background in this kind of profile. Therefore, in order to get a satisfactory profile result, the brightness contributions having the same radial distance from the centre are averaged to improve the SNR. These *azimuthally averaged radial profiles* (AARPs) provide reasonable output only for (partly) rotationally symmetric emission, of course.

The specific characteristics (contrast, smoothness of the background etc.) of the different mapping techniques displayed in Sect. 2.4.2 are also expected to show in the corresponding profiles. Indeed, a comparison in 1D (Fig. 3.1 reflects the impressions of the 2D data. It becomes apparent that the highpass filter artificially enhances the contrast between the shell and the inner region. Apparently, the masking of the bright areas did not completely prevent this artefact. While this fact does not influence the positional measurements, the photometric results will most likely be incorrect (cf. Sect. 3.1.3). Thus, for all further analysis, the output of the Scanamorphos routine is used, also since it renders the faint emission best.

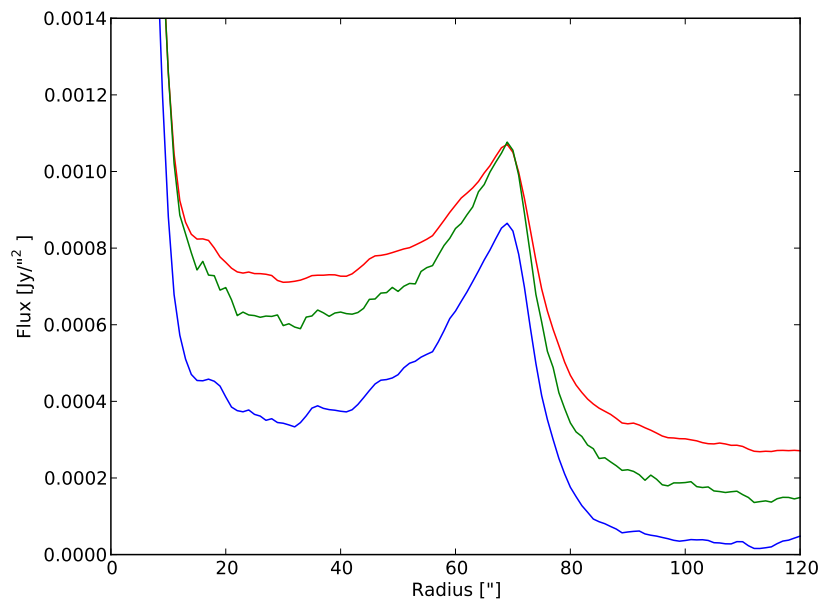


Figure 3.1: AARPs, based on the highpass filtered Photproject (blue), drift corrected MADmap (green) and Scanamorphos (red) output. The highpass filter causes the signal to drop disproportionately between the star and the shell. Also, some shell signal is cut off.

How is an AARP created? One option is to employ the aperture photometry task provided by HIPE. Measuring the differential flux from two concentric apertures for a

range of radii yields a so-called differential aperture photometry profile. The drawback of this method is that it is relatively slow. Moreover, it is restricted to averaging over the full circumference, while some targets require the profile to be created for a limited angular section only. For that matter a suited script was written, making use of HIPE’s built-in capabilities (see Appendix A.2). In short, it computes the radial distance for every pixel and then takes the average over all pixels within a defined radial range. Optionally, the angular section for the averaging can be restricted. Further, instead of a simple circle an ellipse in any user-defined position can be used to enable profiling of even more complex structures. A minor downside of this routine is the fact that it doesn’t provide sub-pixel precision (contrary to the differential aperture photometry approach), but considering the typical angular resolution of the PACS maps (1" and 2" in the blue and red photometric bands, respectively, compared to the PSF FWHM of 5.6" and 11.4") this limitation does not show any noticeable effect in the resulting profiles.

For the detached shell objects the centre of the shells is by default assumed to be located at the stellar position. So the exact coordinates of the reference point for the profile computations are found by fitting a two-dimensional Gauss function to the star. The peculiar tri-lobe shape of the instrument PSF (see Chapter 2) causes some uncertainty in the found peak position. Nevertheless, the effect is small enough (well below pixel size) to be negligible for further analysis.

In the profiles of “showcase” sources (in the sense of having a high symmetry and a good signal-to-noise ratio) the shell signatures are very apparent and well shaped, making a determination of the (average) radius rather easy. The narrow feature, due to the geometrically very thin shell, allows for a identification of the peak position – and thus of the shell radius – without further fitting procedures. When dealing with more difficult examples, however, the approximation of the then more subtle and noisier profile feature by a suitable function is desirable.

One could also apply fitting for the well shaped features. Because of the asymmetric slopes of the shell profile, a Gaussian usually yields unsatisfactory results, so a more complex function has to be used. Given the fact that such a comparatively intricate approach does not significantly improve the results of the initial straightforward peak determination, it is used in non-trivial cases only.

As noted before, some targets having a very symmetric detached shell (e.g. R Scl, TT Cyg) show a small displacement between the star and the centre of the ring shaped emission. This is hardly apparent at first glance – consulting literature reveals that the offset values for the objects in question are typically of the order of $\sim 1''$ (e.g. Olofsson et al. 2000, 2010). Given the map resolution of 1" and the FWHM of the PACS photometer PSF (5.6") at $70 \mu\text{m}$, deviations on such a scale are at the border of being reliably measurable in the Herschel data. Although the shifts are comparatively small to the usual extents of the shells, they still influence the shape of the derived radial profiles, e.g. by broadening the shell signature and additionally dislocating the position of the peak. Therefore, in order to deteriorate the profiles as little as possible, it is recommendable to take the offset central position into account. A rather crude estimate of the misalignment can be derived by comparing the shell positions in profiles from differing azimuthal angles. For example, averaging over circular sectors which point

to the (equatorial) north, east, south and west. Regarding the opening angle of the “cones” a compromise has to be found – large sectors increase the SNR but in turn blur the signal. Once the positions are found, the offset in declination and right ascension can be calculated by simply halving the difference between N-S and E-W, respectively. Consequently, a position angle can be approximated.

A more sophisticated and accurate method to obtain shell parameters is to fit a circle with a Gaussian brightness distribution to the 2D image data. For this task, a routine using the *Python* programming language was employed, making use of the *numpy*, *scipy* and *pyfits* modules. In the case of TT Cyg, using an unaltered version of the Scanamorphos map, the algorithm was not able to find a best fit to the image data – maybe due to the low contrast of the shell structure. Therefore, a technique common in image processing/editing was applied, known as “unsharp mask”. A duplicate of the original image was blurred by convolving it with a Gaussian. This frame was then subtracted from the initial image, resulting in a “sharpened” version. Using the edited data, the fitting procedure was successful (see Fig. 3.2). After the processing the image doesn’t provide the correct photometry anymore, of course, but position measurements remain unaffected. In the case of TT Cyg the fit suggests a displacement between the star and the shell centre of $1.8''$ at a position angle of 20° , which is in excellent agreement with measurements of CO data by Olofsson et al. (2000). As a “byproduct” the fitting also gives values for the shell radius and thickness. As already mentioned, the shell brightness does not exactly show Gaussian characteristics and therefore the best fit radius will most likely not represent the actual peak position as found in the profile. The shell width, on the other hand, is dominated by the PSF, hence no reliable figure for the actual shell thickness can be given without deconvolution, which is limited to the brightest objects though.

Radially Averaged Azimuthal Profiles (RAAPs)

While radial profiles provide useful information about the dimensions of the circumstellar shells and can even reveal details that are barely seen in the maps, it is also of interest to find out about smaller scale structure of the ring shaped emission. That is where *radially averaged azimuthal profiles* (RAAPs) can be helpful to sketch the geometrical properties. In this case brightness values are averaged over a defined radial range for each angular bin. That way brightness (i.e. density) variations can be traced and quantified along the perimeter. Additionally, a frequency spectrum can be computed from the obtained RAAP, as it was done in the work of Olofsson et al. (2010), for example. In their paper, however, they used data from the *Advanced Camera for Surveys* (ACS) on-board the *Hubble Space Telescope*, providing a much higher spatial resolution. In the Herschel data comparable small scale features are not present, hence the frequency spectrum does not provide any useful supplementary information.

3.1.2 Basic Shell Figures

Having determined solely the apparent extent of a circumstellar shell from the profiles, it is already possible to derive – by incorporating various literature data – some further basic properties of the object, such as the physical size and, under certain premises,

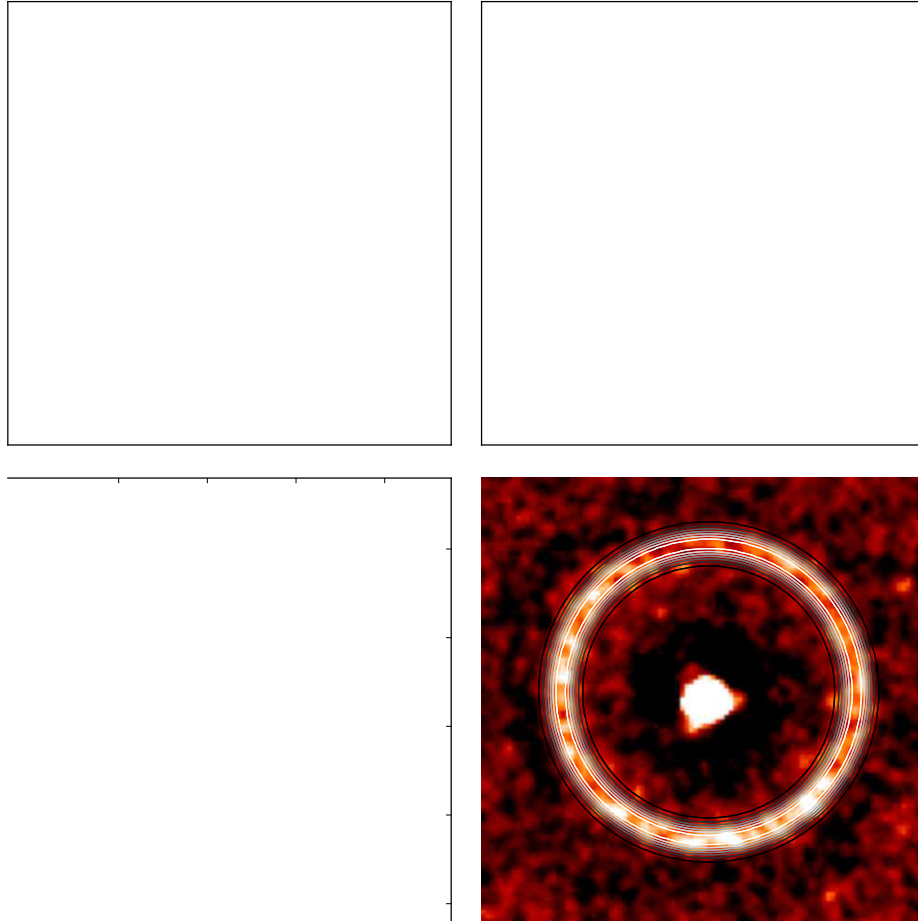


Figure 3.2: TT Cyg as obtained from the Scanamorphos method (top left); TT Cyg after “sharpening” (top right); image of the best fit Gaussian ring (bottom left); “sharpened” TT Cyg image with contours of the fit superimposed (bottom right).

the dynamical age. Due to the rather uncertain numbers concerning the distance and assumptions on the kinematics of the dust and gas component, however, the obtained figures have to be considered as estimates.

Distances

The distance measurements for the MESS sample of objects (and for AGB stars in general) are rarely well confined, mainly because of two reasons. Often the targets are distant, implicating very small parallaxes. Typically, they are just above 1 mas or even below in some cases. Hence, in this regime the relative error of the Hipparcos data (Perryman et al. 1997) is usually too large to allow for a reliable result. On the other hand, also for comparatively nearby sources the distance is difficult to constrain due to the large extension of the star and its pulsating behaviour. Nevertheless, where good data were available, Hipparcos distances were used, taken from a catalogue based on improved, reprocessed data (van Leeuwen 2007).

Alternatively to the parallax measurements, the distances were derived using period-luminosity relations for long period variables. After the work of Knapp et al. (2003), they are

$$M_K = -3.39(\pm 0.47) \log P(\text{days}) + 0.95(\pm 3.01)$$

for Miras and

$$M_K = -1.34(\pm 0.06) \log P(\text{days}) - 4.5(\pm 0.35)$$

for semiregular variables, using K band photometry. The corresponding periods were obtained from the *General Catalogue of Variable Stars* (GCVS) (Samus et al. 2009), photometric data were taken from the *PPMXL* catalogue (Roeser et al. 2010), which incorporates the *Two Micron All Sky Survey* (2MASS) (Cutri et al. 2003). Another possibility, for example in the case of objects with unknown pulsation period, is to assume a K-magnitude and that way estimate the distance. This approach, however, has not been taken.

Expansion Velocities

Observing the dust and its FIR thermal emission does not yield any direct quantitative information on kinematic properties of the CSE. On the contrary, for example (sub-)millimetre or radio observations of molecular line features can provide accurate expansion velocities. A good resource including, among other parameters, these velocities is the catalogue compiled by Loup et al. (1993). They searched literature for observations of $^{12}\text{CO}(1-0)$, $^{12}\text{CO}(2-1)$ and $\text{HCN}(1-0)$ lines, mostly in AGB stars. One has to be cautious though, because a lot of measurements only detect the present day mass-loss and not the movement of the older detached shell that is required. For the cases without an appropriate entry a generic value of 15 km s^{-1} can be used. Although theory suggests a drift between the dust and the gas component in the slow AGB stellar winds, the assumption of dust overtaking the gas was neglected for the sake of having at least a rough estimate on the dust speed. As a comparison of CO maps (e.g. Olofsson et al. 2000) with PACS data reveals, such a scenario seems to be justifiable in at least some cases. A more detailed discussion is given in Sect. 4.1.1.

When one considers a scenario, where the detached shell is the consequence of a thermal pulse and can expand freely (i.e. no interaction with the ISM), the dynamical age of the structure can be estimated easily. The ages typically range from 1000 (or even below for the very youngest) to some 1000, or few 10 000 years.

3.1.3 Photometry

The PACS photometer is able to observe in three wavelength bands (70, 100 and 160 μm , see Fig. 2.2). Because of limited observing time, however, only scanmaps in the 70 and 160 μm band were obtained for the vast majority of the MESS sample. For both channels aperture photometry was conducted (again using the functionality of HIPE), measuring the flux of the central star and the separated shell. The appropriate parameters for the aperture size, the annulus and the region for measuring the background flux were chosen based on the AARPs. Also the total flux of the target (i.e. everything inside the outer shell edge) was measured, in order to compare it to the photometric data of previous IR space missions such as IRAS and ISO. Except for the (apparently) very largest shells, these did not have sufficient resolving power to distinguish between the source components.

In some cases the correct determination of the background was hampered by the extended emission of the surrounding ISM. Especially the 160 μm maps often display filamentary structures, biasing the outcome. Moreover, also rather concerning the longer wavelengths, a non-uniform background is caused by erroneous drift correction during processing.

As is already evident from the AARPs, the outcome of photometric measurements somewhat depends on the chosen mapping technique, too. With improving absolute photometric calibration accuracy, this circumstance cannot be neglected. In the early Herschel mission phase the typical absolute calibration error was 10% in the 70 μm and 15–20% in the 160 μm band. Up to now the uncertainty has improved to 5 and 10% in the blue and red, respectively. Exemplarily, Fig. 3.3 shows the dependencies of the aperture photometry on the employed reduction methods. An obvious trend is due to the highpass filter width – at small sizes parts of the real signal seem to be removed by mistake. At larger widths the effect decreases, but at that point the drift and noise aren't corrected sufficiently anymore. Thus, currently the Scanamorphos maps are considered to deliver the most reliable photometric results.

Dust Temperature

With flux information at just two wavelengths the options for scientific deductions are rather limited. Whilst with more photometric measurements a SED fit would be adequate to estimate the temperature of the dust component of the circumstellar shell, necessarily here the approach is more straightforward. In a first simple attempt one assumes the spectrum of the shell emission to have the shape of a blackbody. Comparing the ratio of the two observed fluxes F_{70}/F_{160} to the ratios obtained from a calculated range of Planck curves gives the approximate temperature. The monochromatic fluxes were not considered to get the theoretical flux ratio. Instead, the blackbody spectra

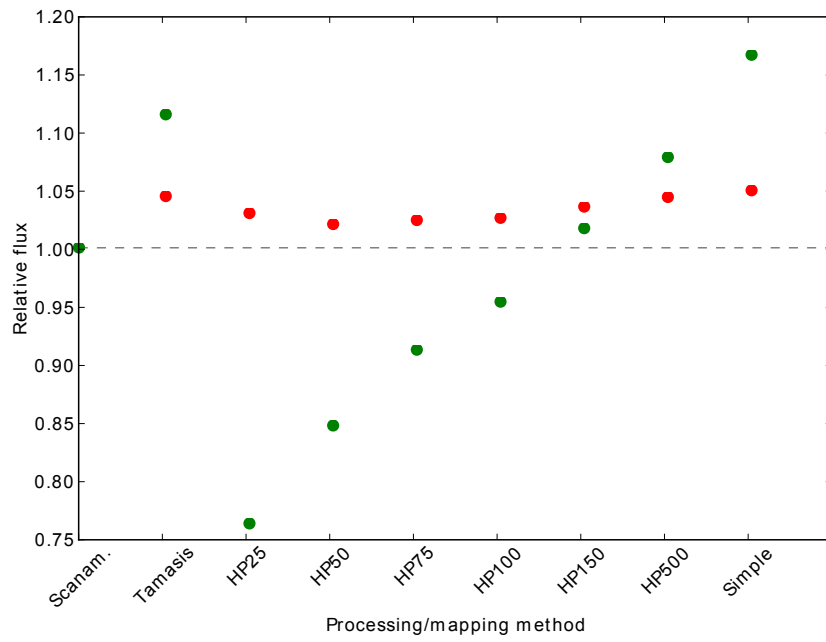


Figure 3.3: Photometry measurements for the various reduction methods/parameters (Scanamorphos, Tamasis, highpass filtering and simple baseline subtraction with Photproject), given relative to the Scanamorphos result. Red dots are measurements of the whole object from which the outer background is subtracted. Green dots represent the star minus the “inner” background (between the star and the shell).

were convolved with the two filter response curves of the PACS instrument (Fig. 2.2)¹. In another variant, the blackbody is replaced by a greybody, with additional parameters allowing to modify the spectrum. The flux of a greybody $F_{\lambda,\text{GB}}$ relates to that of a blackbody $B_{\lambda}(T)$ as follows:

$$F_{\lambda,\text{GB}} = B_{\lambda}(T) (1 - e^{-\tau})$$

where

$$\tau = \left(\frac{\lambda_0}{\lambda} \right)^{\beta}$$

is the wavelength dependent optical depth, with β being the spectral coefficient and λ_0 the wavelength at which τ is 1. Analogously the theoretical fluxes are derived taking into account the spectral response of the PACS filters. Figure 3.4 depicts the properties of the BB and GB curves and their dependence on the parameters. For amorphous carbon in circumstellar environments the spectral index β is usually near 1 (Andersen et al. 1999). A value of $\beta = 1.1$ is adopted, λ_0 is set in steps from 50 to 200 μm .

Looking at the resulting dust temperatures, the figures are within the order of magnitude of what is expected for the cold shell material (e.g. Olofsson 2004). Nonetheless both blackbody and greybody models are most likely not very realistic, considering excess in the FIR region that is usually present in the detached shell class of objects (cf. Fig. 3.10). To account for the radiation characteristics of the carbon dust, the emission of the shell j_{λ} can be described, following Kirchoff's law, as

$$j_{\lambda} = k_{\lambda} j_{\text{BB},\lambda}(T)$$

where $j_{\text{BB},\lambda}$ is the emissivity of a blackbody at wavelength λ and k_{λ} the dust absorption coefficient. Draine (1981) provides the Q factor, which is proportional to k_{λ} . Since only the ratio at two wavelengths is needed, Q can be used instead of k_{λ} . To determine the dust temperature thus the relation

$$\frac{F_{70}}{F_{160}} = \frac{Q_{70} j_{\text{BB},70}(T)}{Q_{160} j_{\text{BB},160}(T)}$$

can be used. Given $Q_{70}/Q_{160} = 439/203 = 2.16$, the dust temperature must therefore satisfy the condition

$$\frac{j_{\text{BB},70}(T)}{j_{\text{BB},160}(T)} = \frac{F_{70}/F_{160}}{2.16}.$$

The findings of these rather simple methods can be compared to results of more sophisticated modelling, which also yields additional parameters, described in the next section.

3.2 Modelling Circumstellar Shells – The DUSTY Code

The dust commonly surrounding TP-AGB stars severely influences the radiation originating from the central star. To predict and model the scattered, absorbed and reemitted light, the problem of radiation transport in a dusty environment has to be solved. To

¹The HIPE-script for that routine was provided by Stefano Pezzuto.

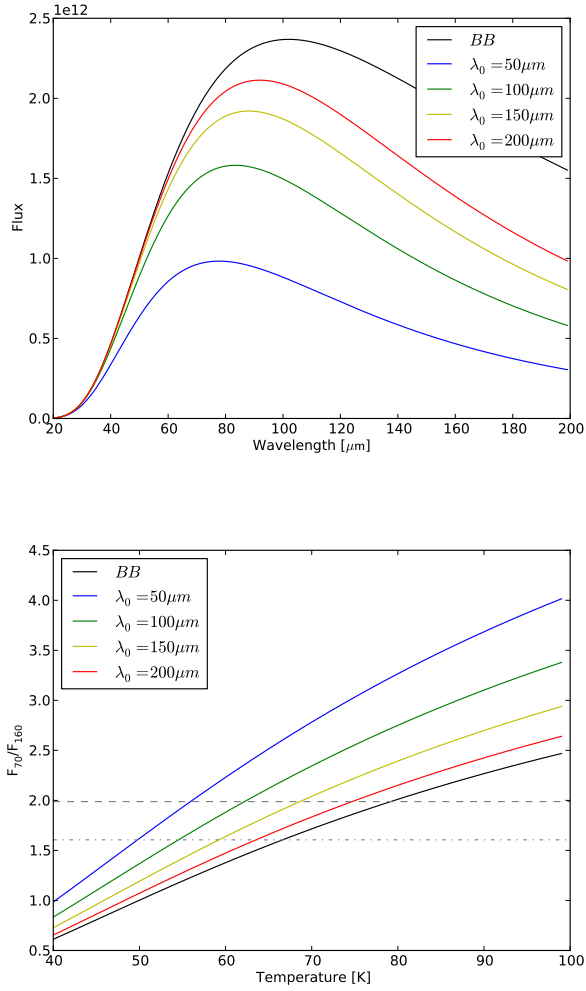


Figure 3.4: *Top*: spectral curves representing blackbody and greybody emission at $T = 50$ K. For the greybody $\beta = 1.1$ and the annotated λ_0 -values were adopted. *Bottom*: dependence of the PACS $70 \mu\text{m}/160 \mu\text{m}$ flux ratio on T , assuming the flux distributions given in the top panel. Observed flux ratios of TT Cyg (dashed) and UX Dra (dash-dotted) are indicated by horizontal lines. For the considered cases the BB emission yields the highest temperature estimate.

this end DUSTY (Ivezic et al. 1999) was used, a code for 1D radiative transfer modelling. Providing input such as the spectral shape of the initial (hereafter also called external) radiation, optical properties of the dust grains and density distribution, the output is computed, based on the equation of radiative transfer in steady-state (after Ivezic & Elitzur 1997)

$$\frac{dI_\lambda}{dl} = \kappa_\lambda (S_\lambda - I_\lambda)$$

where κ_λ is the overall extinction coefficient at a given wavelength λ , being the sum of the absorption $\kappa_{a\lambda}$ and scattering $\kappa_{s\lambda}$ coefficients. The optical depth $d\tau_\lambda$ along a path dl follows the relation $d\tau_\lambda = \kappa_\lambda dl$, and S_λ and I_λ are the source and intensity functions, respectively.

As found by Rowan-Robinson (1980) the radiative transfer problem has general scaling properties that reduce the parameter space. Moreover, Ivezic & Elitzur (1995) found that with given optical dust properties the results are described by a single parameter – the overall optical depth. Consequently, the DUSTY-calculations are independent from linear sizes and in turn also length scales cannot be derived, of course. For example, two systems with different absolute extent and absorption coefficients can have the same optical depth and hence equal radiative intensities. Thus an independent method for determining the system size is needed. A detailed discussion of the solution to the 1D radiative transfer problem is given in Ivezic & Elitzur (1997).

3.2.1 Input Parameters

Regarding the geometrical shapes of the modelled environments, DUSTY is able to compute the radiation transfer for either planar or centrally heated spherical density distributions. For the input parameters it provides manifold options, already implemented models and settings can be employed as well as suited user supplied variants.

External radiation

For all models a centrally heating point source was assumed to be the origin of the internal radiation (somewhat confusingly, this radiation is referred to as *external* in the DUSTY nomenclature, meaning it is not originating from the dust itself). Due to the geometry and the scaling properties of the code, the only attribute of this parameter is the spectral shape of the flux. The simplest way to go is to assume a blackbody with a given temperature. This simple case can be modified by adding further sources (up to ten, with individual temperatures and luminosities) to account for binary or multiple systems, for example. To account for atmospheric effects, such as the influence of H^- and SiO (Engelke 1992; Marengo et al. 1999), a modified Planck curve, the so-called Engelke-Marengo function can be applied.

Another option is a broken power law of the form

$$\lambda F_\lambda \propto \begin{cases} 0 & \lambda \leq \lambda(1) \\ \lambda^{-k(1)} & \lambda(1) < \lambda \leq \lambda(2) \\ \lambda^{-k(2)} & \lambda(2) < \lambda \leq \lambda(3) \\ \vdots & \\ \lambda^{-k(N)} & \lambda(N) < \lambda \leq \lambda(N+1) \\ 0 & \lambda(N+1) < \lambda \end{cases}$$

Finally, also user specified input lists providing $\lambda F_\lambda (= \nu F_\nu)$ or F_λ or F_ν vs. λ can be used. If the shortest tabulated wavelength is above $0.01 \mu\text{m}$, the flux is set to zero for all smaller wavelengths. At the long wavelength end, missing values are extrapolated until 3.6 cm following the Rayleigh-Jeans law.

The modelled targets are all carbon stars, therefore both single blackbody radiation and COMARCS stellar atmosphere models (Aringer et al. 2009), covering a narrow parameter range, were tested as external sources. For orientation, values from Bergeat et al. (2001) were consulted for temperature and Abia et al. (2002) for the CO ratio, in order to choose the suited COMARCS models.

As can be seen from Fig. 3.5 the change in the condensation radius when using an atmosphere model instead of a blackbody is not very significant. Especially since this work focuses on the radiation intensity distribution only, and does not incorporate spectral analysis (where distinct absorption and emission features in the source spectrum certainly do have a large impact), the simpler blackbody option is chosen for all modelling attempts.

Dust Chemical Composition

The optical properties of the dust depend on the absorption and scattering cross sections of the present dust species. DUSTY provides these for six common grain types. Additionally, the user can specify up to ten more species by either supplying the absorption and scattering coefficients directly, or inputting the corresponding real and imaginary part of the index of refraction, from which the coefficients are then calculated using Mie theory. For each constituent its fractional abundance has to be chosen. DUSTY then simulates the mixtures by a single grain that composes all the given species.

To test the influence of the different chemistries on the shape and size of the CSE, a grid of models was computed, representing the basic grain types, typical for both oxygen and carbon rich environments. As Fig. 3.7 shows, in the case of silicate dust – with all the other parameters remaining the same – the dust shell forms much closer to the star than in the case of amorphous carbon. This is due to the fact that silicate dust is more transparent for infrared radiation, compared to carbonaceous grains and can thus condense at smaller radii. However, since the selected targets are known to have a C/O greater than 1, the models intended to fit the individual observations incorporate only species that are present in carbon rich environments.

Grain Size Distribution

Not only the chemical composition but also the grain size distribution in the CSE play an important role in the radiative transfer problem. By default, DUSTY provides two kinds of distribution shapes. One the one hand it is the Mathis, Nordsieck and Rumpl (MNR) power law (Mathis et al. 1977), which is expressed as

$$n(a) \propto a^{-q} \quad \text{for} \quad a_{\min} \leq a \leq a_{\max}.$$

Here n is the grain size distribution and a is the radius of the grains considered to have a spherical form. Further there is a modified version of this relation by Kim, Martin and Hendry (KHM) (Kim et al. 1994), in which the sharp upper cutoff in the MNR distribution is replaced by a smooth exponential drop with the characteristic grain size a_0 :

$$n(a) \propto a^{-q} e^{-a/a_0} \quad \text{for} \quad a \geq a_{\min}.$$

The effect of the steepness of the power function and the lower and upper grain size limit as well as the difference between the MNR and KHM models is depicted in Fig. 3.8.

Alternatively, further distributions can be applied, although they have to be implemented as a subroutine. For example, in the work of Kerschbaum et al. (2010) a continuous distribution of ellipsoids (CDE, for details see Min et al. (2003)) was used instead of spherical grains. For the modelling in this work the default MNR distribution was chosen, adopting the standard grain parameters $q = 3.5$, $a_{\min} = 0.005 \mu\text{m}$ and $a_{\max} = 0.25 \mu\text{m}$.

Condensation Temperature

The condensation temperature parameter determines the temperature at the inner border of the shell. Trying to model exclusively the C-rich stars, primarily the properties of carbon dust were of interest. As estimated by Salpeter (1977) the condensation temperature of carbonaceous species can reach up to 1800 K. This temperature regime applies for the innermost regions where dust grains can begin to form. However, since the detached shells observed with Herschel are at larger distances and have advanced dynamical age, the dust temperatures in these structures are expected to be much lower, of course. Based on the findings of the $70 \mu\text{m}/160 \mu\text{m}$ flux ratio in Sect. 3.1.3 and modelling results in Kerschbaum et al. (2010) the considered temperature range for the cold dust was 20–100 K.

Density Profiles

The density distribution in spherical geometry is given as a function of the scaled radius

$$y = \frac{r}{r_1}$$

with r_1 being the inner radius of the shell. The dimensionless density profile can be defined as an analytic function (e.g. a (piecewise) power law or showing an exponential decrease) or being supplied by an arbitrary tabulated profile. DUSTY also provides the possibility to calculate the density distribution in the case where the wind is driven by radiation pressure on the dust particles, by solving a set of hydrodynamic equations,

incorporating dust drift and gravitational attraction from the star (for details see Ivezic & Elitzur 1995). This option is of special interest in the present case of modelling AGB stars.

All variants have in common, that the outer boundary of the shell has to be constrained by an additional parameter Y , which gives the relative shell thickness in terms of the inner shell radius r_1 . Two options were tested: a power law of the form

$$\eta(y) \propto y^{-2}$$

where η is the dimensionless density, and the full radiatively driven wind solution. For both cases a range of shell thicknesses was tested, with the lower limit being $Y > 1$, below which a solution is not achievable, and a maximum extension of $Y = 1000$. While the advantage of the predefined density distribution is the shorter computation time, a benefit of the full hydrodynamic solution is that it also yields, among others, the mass-loss rate as an output parameter, whereas for the fixed power law distribution this is not the case.

Optical Depth

Optical depth crucially affects the modelling results (see Fig. 3.7). For the input the wavelength for which the optical depth τ_λ is entered can be chosen freely. Following the usual convention τ_λ was specified for $\lambda = 0.55 \mu\text{m}$. The computed models sample $\tau_{0.55\mu\text{m}}$ -ranges between 0.001 and 100 for exploratory purposes, representing objects with both low and high mass-loss obscuring the central star.

3.2.2 Modelling Output

A successful DUSTY run yields comprehensive results, basically in three categories. Global parameters describe the general properties of the computed model, such as the bolometric flux hitting the inner shell border, apparent and linear shell size. In the case of a full solution of a radiatively driven wind there is even more information, like the mass-loss rate and terminal outflow velocity. Furthermore there are radial profiles for several physical quantities, e.g. the density, dust temperature, optical depth and most importantly, since it is used for direct comparison (i.e. fitting) with the observations, the surface brightness. Again, for a RDW calculation there are additional tabulations for Γ and the velocity drift between the gas and dust components. Completing the extensive output are various spectral data, providing widely used fluxes and colours, as well as spectral distributions.

General Characteristics

At first, and before tackling the main task of producing models which should reproduce the observations, a large parameter space was defined to explore the general behaviour of the output model over a widespread range of physical conditions. For the actual model fitting (see Sect. 3.2.3) the parameters were then narrowed down to only include plausible values for the respective objects.

In the following, the effects of the input parameters and their relevance for modelling the detached shell objects are briefly illustrated. All brightness profiles are calculated for a wavelength of $70\ \mu\text{m}$.

Figure 3.5 shows the impact of different external radiation sources on the resulting dust condensation radius and thus the shell size. Apart from the characteristic spectral features, the COMARCS models allow for smaller condensation radii than a blackbody with the matching temperature. Since this work does not try to model spectral properties of the observed objects, a BB seems to be a viable approximation of the centrally heating source, even more so if the stellar characteristics are not well known and hence neither is the appropriate model. For the BB case the obtained radius values can be regarded as an upper limit. However, for the considered objects the required stellar parameters are available and thus the most likely better suiting COMARCS spectra have been adopted for modelling.

The arguably most important factor in the calculations is the dust chemistry. The optical constants (n , k – see Fig. 3.6) and thus the absorption and scattering efficiencies of the respective dust species vary substantially, and accordingly should the computed shell parameters. Looking at Fig. 3.7, there is a generally recognisable trend that silicate mixtures, as they are expected in oxygen rich environments, at a given temperature exist closer to the star, i.e. are more transparent to the radiation, than the carbonaceous dust. For the case of amorphous carbon several measurements of n and k were tested. Surprisingly, even in this subsample the differences can be striking, up to a factor of almost 3 between the condensation radii of the largest and smallest carbon shell. This implies that the opacity of carbon material can differ by nearly an order of magnitude ($L \propto r^{-2}$), depending on the considered measurement. The enormous variations can be explained by the very different environmental conditions under which the constants are determined (see, e.g. Zubko et al. 1996).

This thesis only deals with carbon stars, therefore the silicate mixtures can be excluded for the modelling process. From the amorphous carbon species several were tried out in more detail (amC-Pb, amC-zb1, amC-Hn). Also, the impact of the abundance of silicon carbide was investigated.

As can be seen from Fig. 3.8, the effect of the chosen grain size distribution is small. The brightness is slightly enhanced in the case of the KHM distribution, the peak position remains essentially unchanged. It can be assumed that the choice of the grain size distribution will not notably influence the outcome of the fitting procedure.

The possible relative thicknesses of a dust envelope can span a large range. While young (i.e. representing the present mass-loss) shells can expand to $Y = 100$ or even more, the more distant, dynamically old and cold detached shells observed with Herschel are geometrically thin ($\Delta R \ll R$, i.e. $Y \ll 1$). However, DUSTY only allows calculations for which $Y > 1$. Nevertheless, small values of Y are still able to reproduce the detached shells. While changing the thickness above $Y \approx 10$ has no great impact on the radial properties in the important region around the brightness peak, thinner shells do show a very increased peak intensity (Fig. 3.9).

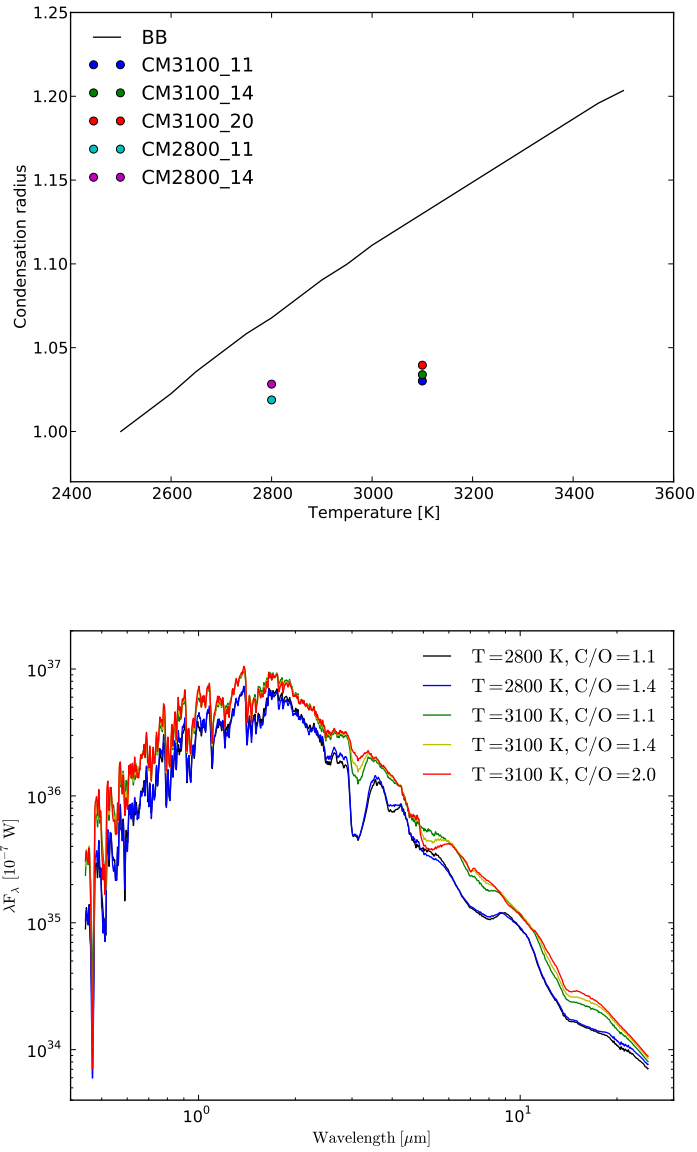


Figure 3.5: *Top*: condensation radius as a function of the spectral shape of the external source. Black line indicating BB temperature dependence, compared to COMARCS models of a C-rich atmosphere depicted in the bottom panel. COMARCS models yield lower shell radii and seem to show a lower T-dependence. An effect of the C/O ratio is also noticeable. *Bottom*: spectra of COMARCS model atmospheres for stars with solar mass and metallicity and the respective annotated temperature and C/O ratio.

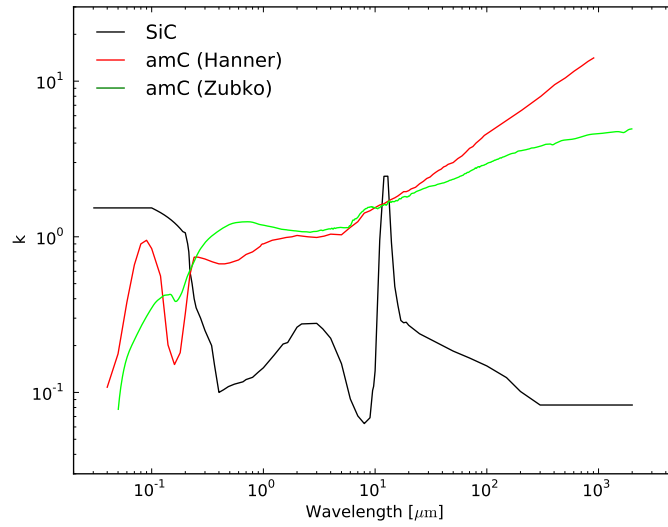
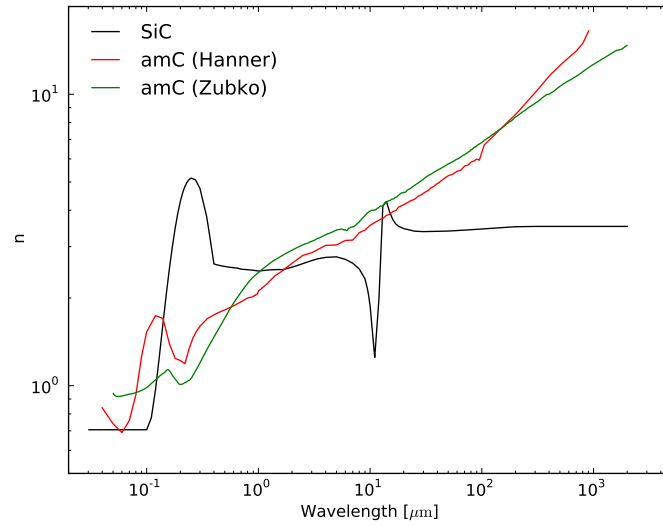


Figure 3.6: Optical constants n and k for different dust species. All data comes with the DUSTY package, see Ivezić et al. (1999) for references.

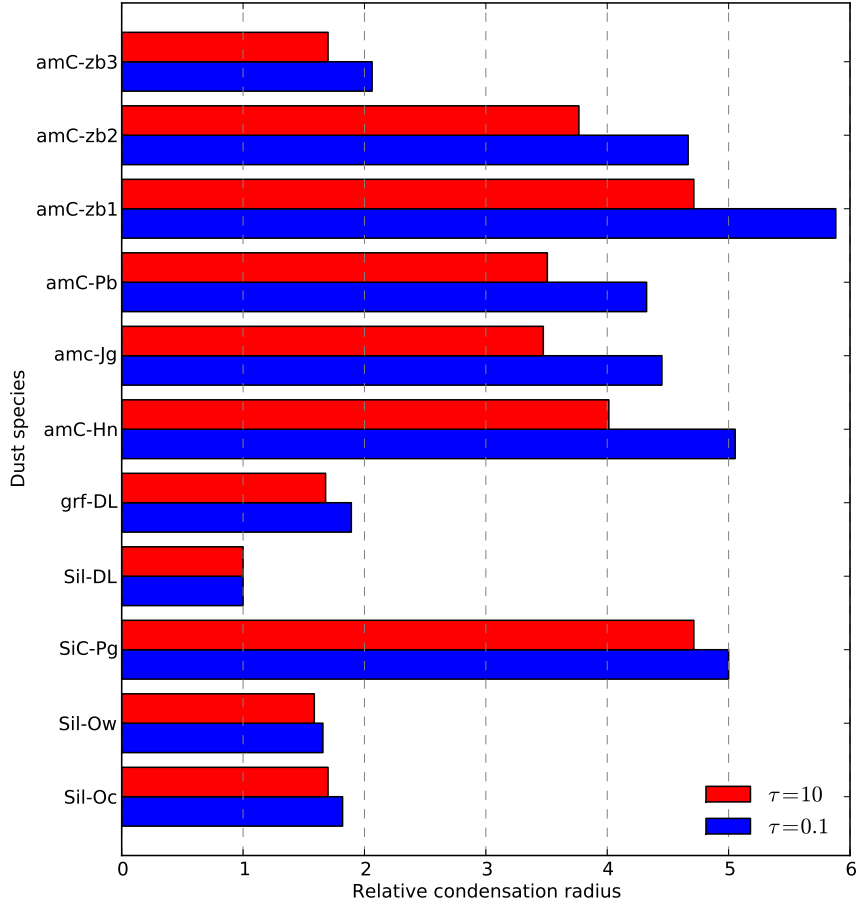


Figure 3.7: Condensation radius as a function of the dust species for a fixed condensation temperature. Blackbody with $T_{\text{eff}} = 2800$ K as the external source, density distribution $\propto r^{-2}$ and standard MNR grain size distribution. Results are given for the optically thin and thick case. The radii are normalised to the lowest value (Sil-DL). *Abbreviations:* Sil-DL: “Astronomical silicate”, Sil-Ow: warm O-deficient silicates, Sil-Oc: cold O-rich silicates, grf-DL: graphite, SiC-pg: α -SiC, amC-Hn: amorphous carbon, amC-zb1: amorphous carbon (BE), amC-zb2: amorphous carbon (ACAR), amC-zb3: amorphous carbon (ACH2), amC-Pb: amorphous carbon (Preibisch et al. 1993), amC-Jg: amorphous carbon (Jager et al. 1998). For further details and references see Ivezić et al. (1999).

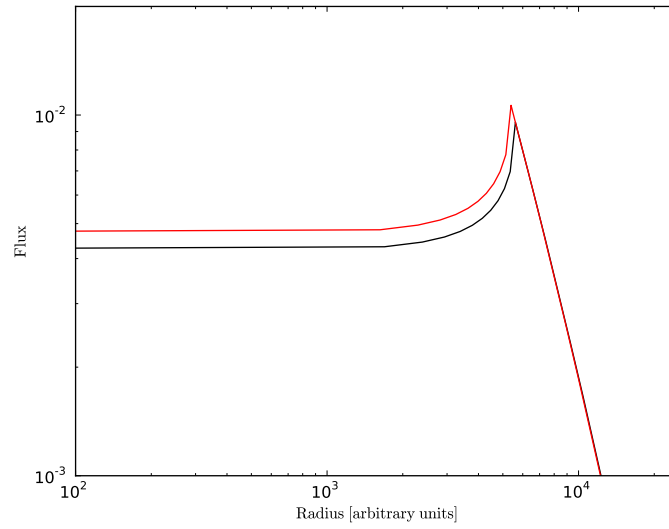


Figure 3.8: Radial brightness profiles for standard MNR (black) and KHM (red) grain size distributions, computed for the parameters $T = 2800 K$ and $\tau = 0.1$.

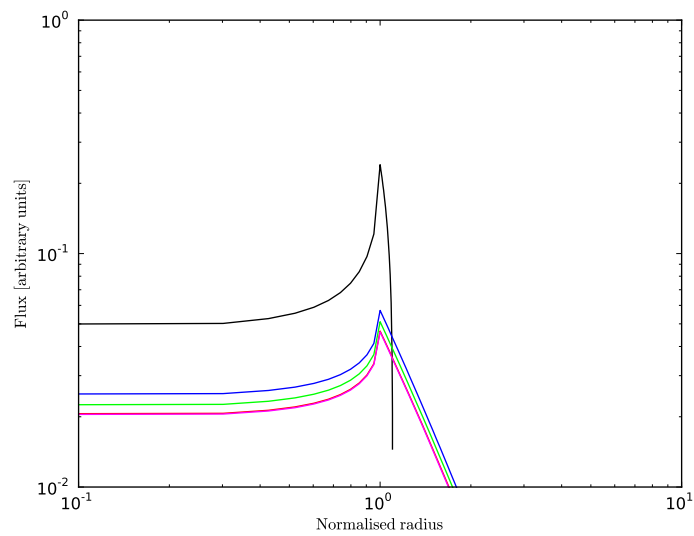


Figure 3.9: Radial brightness profile, as it changes with shell thickness Y . Plotted are $Y = 1.1$ (black), $Y = 5$ (blue), $Y = 10$ (green), $Y = 100$ (red) and $Y = 1000$ (magenta).

Besides the changing geometric and photometric shell characteristics it is also interesting to take a look at the general spectral shape of the radiation. Fig. 3.10 shows how the dust component around the star alters the emission. The FIR bump caused by the cold dust nicely explains the very red colours that are observed for detached shell objects.

Based on these testing results a set of parameters was selected for the model fitting.

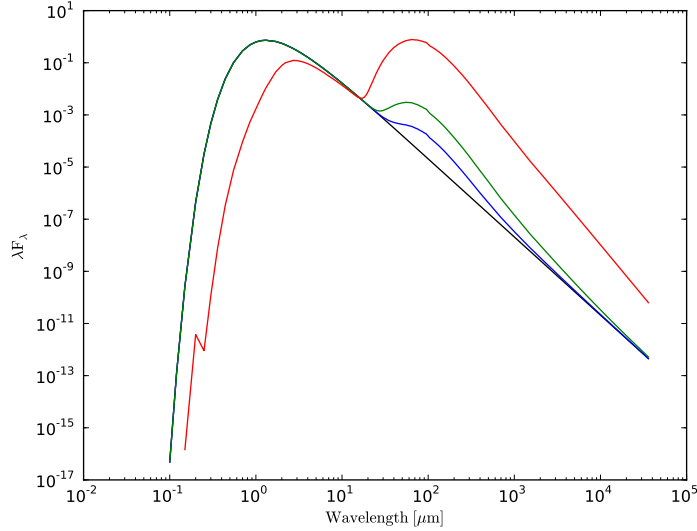


Figure 3.10: The influence of warm and cold dust on the spectral shape of the observed light of an AGB star. The warm dust component close to the condensation radius ($T = 1100$ K) causes the initial BB emission ($T = 2800$ K) to peak at NIR wavelengths ($\approx 1 \mu\text{m}$) (black line). When a cold dust component is present (i.e. a detached shell) a second maximum can be observed in the FIR. While at low optical depths only a subtle bump is noticeable, for large τ (i.e. high mass-loss) the FIR maximum can even exceed the NIR one, which is additionally shifted to longer wavelengths. Another effect, not displayed in the plot: the colder the dust, the longer the wavelength of the FIR feature position.

3.2.3 Models & Observations

In order to determine the model parameters that resemble the observations best, the computed brightness profiles were compared to the AARPs obtained from the respective PACS maps. In a first simple approach the model output profile, which is sampled at 105 unequally spaced radial positions by default, was interpolated to a uniform grid. Since the DUSTY calculations are scale free, a scaling factor has to be applied to get absolute values on the actual size of the model. This can be done in two ways, by either giving a bolometric flux measurement or a luminosity value expressed in solar units and a distance. The calculated spatial dimensions and thus the best fitting parameters critically depend on this input (the poorly known distances are a major source of uncertainty).

The angular size of the model scales with the bolometric flux $l \propto \sqrt{F_{\text{bol}}}$, as does the inner shell radius with the luminosity $r_1 \propto \sqrt{L}$. The luminosity was derived via the relation

$$\frac{L}{L_{\odot}} = 10^{-0.4(M_{\text{bol}} - 4.73)}$$

where the absolute bolometric magnitude M_{bol} for the targets was obtained from Bergeat & Chevallier (2005). For the distance figures from the same paper were adopted, as well as values from Hipparcos and P - L relations for comparison.

After the model profile is properly scaled it needs to be convolved with the PSF of the PACS instrument at the respective wavelength to enable a correct comparison. A Herschel observation of a source showing no extended emission (AFGL 1390 in this case) was used for this purpose. Its radial profile, representing the 1D-PSF, was convolved with the regridded and rescaled model output. As it turns out, a convolution in one dimension does not yield an accurate enough model profile, particularly when it comes to the very inner regions (cf. Fig. 3.11). Due to the asymmetric PSF (see Fig. 2.4) a two-dimensional treatment is necessary. In this way the model profile is created from a synthetic image using the same method as for the observed profile.

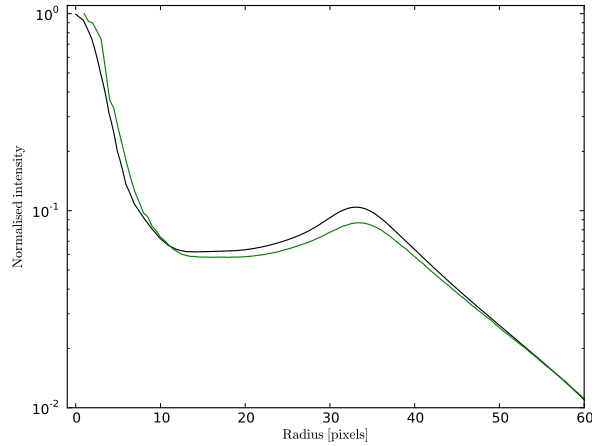


Figure 3.11: A convolution of the 1D model profile with a PSF AARP (black) yields results that deviate from the profile obtained from a model convolved in 2D (green).

In the 2D approach the steps up to the scaling are identical to the 1D case. Then a synthetic map is created from the profile information at the same pixel scale as the observation (see Fig. 4.7). Using 2D Fast Fourier Transform the image is convolved with the properly shaped PSF. From the resulting map the profile is created, which now better resembles the typical shape of an observed profile.

The model profile is then compared to the observation profile and an error Δ is computed:

$$\Delta = \sum \frac{(I_{\text{mod}} - I_{\text{obs}})^2}{\sigma^2}.$$

I_{mod} are the calculated intensity points and I_{obs} the observed ones. σ is the error of the observation.

Since the quality of the fit has to be evaluated for a large number of models, the described steps have to be executed by an efficient automated method. This task was handled by a Python script (see Appendix A.3) outside the HIPE environment. The way to compute an AARP in HIPE was slow and hence not suitable here, therefore a quicker method was employed².

Model Types

The spatial resolution of the maps delivered by PACS and hence the profiles is far too low to directly detect young shells close to the condensation radius. Therefore, in a first attempt only the extended detached shells were considered in the model. In such a scenario, the model consists of the central star, represented by a COMARCS spectrum, and a geometrically thin ($Y = 1.1\text{--}3.5$), low temperature ($T = 30\text{--}70\text{ K}$) dust envelope. Data from Preibisch et al. (1993) were adopted for the optical properties of a pure amorphous carbon composition. The density distribution was calculated from the solution for a radiatively driven wind. Using these parameters for a range of opacities in the optically thin limit ($\tau = 0.001\text{--}0.5$), an approximate fit for the region around the shell peak was found. For the inner part, on the other hand, especially the stellar component, a satisfying fit was not possible, i.e. with the shell brightness at the observed level the central emission is always too faint. Therefore the initial model was modified by adding a warm ($T \approx 1000\text{ K}$) shell close to the star (representing present, spatially unresolved mass-loss), with the intent that this dust component would shift the emission towards longer wavelengths and hence increase the central brightness in the observed 70 and 160 μm bands (cf. Fig. 3.10). In a first run the warm shell was calculated, using the same chemistry as for the outer envelope. The resulting output spectra were then fed to a second run as the “external source”, computing the detached shell. Several parameter sets were tested for the inner shell, however, only a change in the optical thickness had relevant effects on the finally obtained radial profile. Varying the geometrical thickness and dust temperature did not have any severe influence. With this approach both the central emission and the detached shell were successfully (to a certain degree) reproduced.

In carbon rich environments amC is by far the most abundant species, nevertheless additional constituents can play a role. SiC and MgS are usually the most abundant ones, with fractions of typically 5 to 10%. To decide whether to incorporate one of the two or even both of these species, ISO SWS spectra or, in case those were not available, IRAS low resolution spectra can be consulted. Presence of silicon carbide is thought to be indicated by a feature at 11.2 μm , whereas magnesium sulphide is traceable via a feature at $\sim 30\text{ }\mu\text{m}$. However, given their usually low abundance and (at least for SiC) quite similar characteristics/effect regarding a shell’s geometrical shape, their impact on the present modelling, with no interest in spectral fitting, is practically negligible.

²Code by Adam Ginsburg, available at <http://code.google.com/p/agpy/source/browse/trunk/agpy/radialprofile.py?r=346>

Shortcomings

While the observed central emission and most of the shell are reproduced by the model, other parts of the radial brightness profile do not fit as accurately. Typically, the part between the stellar emission and the detached envelope is too faint in the model, i.e. the contrast of the ring shaped emission with respect to the “inner background” is higher than observed. In models where this intermediate area is congruent with the observations (e.g. for increased τ), the detached shell does not match. A possible solution to this problem could be an addition of further (low mass-loss) shells, as it was done in Kerschbaum et al. (2010), for example.

Another flaw of the obtained models is the fact that they don't reproduce the outer part of the shell well. In the observations the intensity to the background level is smoother than in the model. Out of all tried density distributions, the full wind solution seems to approximate the radial profile best in this region.

These shortcomings, however, while they may prohibit a proper description of the whole object, are not expected to severely influence the determination of certain parameters of the detached shell. Values such as the dust temperature (which is mainly determined by the shell position only) or envelope thickness, and to some extent even the mass-loss that caused the structure should be usable.

Chapter 4

Dust Shells Around Evolved Stars

4.1 TT Cygni & UX Draconis – A Well Known and a New One

4.1.1 TT Cygni

The carbon star TT Cyg (IRAS 19390+3229) of spectral type C5,4 is a semiregular variable (SRb) with a pulsation period of 118 days, according to the GCVS. The visual amplitude is 1.1^{mag} with a brightness minimum of 11.9^{mag} and a maximum of 10.8^{mag} . The IRAS colours are $[12]-[25]=-1.45$ and $[25]-[60]=-0.21$, which places TT Cyg in the “VIa” sector of the colour-colour diagram established by van der Veen & Habing (1988). Objects in this part of the diagram are attributed as typically *having cold dust at large distances and generally being carbon stars*.

For the stellar temperature Bergeat et al. (2001) derive an effective temperature of 2825 K. In Bergeat & Chevallier (2005) the bolometric magnitudes are given as $m_{\text{bol}} = 4.99^{\text{mag}}$ and $M_{\text{bol}} = -3.98^{\text{mag}}$, where the latter corresponds to a luminosity of $3050 L_{\odot}$. Further, a bolometric flux is provided, $F_{\text{bol}} = 2.52 \text{ W m}^{-2}$. The atmospheric composition according to Abia et al. (2002) has a C/O ratio of 1.04.

The distance estimates are quite uncertain, Bergeat & Chevallier (2005) give a value of 620 pc, while the Hipparcos parallax measurement (van Leeuwen 2007) suggests 560 pc, with a considerable error of $-130, +230$ pc. Using period-luminosity relations and K-magnitudes, an even smaller distance of 440 pc is obtained for the relation of Groenewegen & Whitelock (1996), whereas the formula of Knapp et al. (2003) yields a much larger value of 700 pc. Both figures are, however, still within the Hipparcos error. The proper motion of the star is 6.3 mas yr^{-1} (P.A. = -120°), the radial velocity -49 km s^{-1} .

The Detached Shell

The $60 \mu\text{m}$ excess found for TT Cyg, along with several other carbon stars in the IRAS survey (van der Veen & Habing 1988), was interpreted as a consequence of cold detached dust shells by Willems & de Jong (1988). This scenario was supported by single-dish observations of molecular line emission by Olofsson et al. (1990), who found indication for a detached CO shell. Further observations delivered proof of such a circumstellar structure and also provided an estimate of the shell size (Olofsson et al. 1996). First spatially highly resolved images of TT Cyg were presented in Olofsson et al. (1998), and a thorough analysis on the interferometric IRAM Plateau de Bure CO data was conducted in the paper by Olofsson et al. (2000). Given the high resolution (beam sizes of $\sim 2''$ and $\sim 1''$ for the $J = 1 \rightarrow 0$ and $J = 2 \rightarrow 1$ data, respectively), stunning details in the shell structure were observable. The shell turns out to be remarkably thin, with

a width of $2.5''$ at a radial distance of $35''$, also, its centre shows a slight offset ($1.7''$, P.A. = -20°) with respect to the stellar position. The shift in position is thought to be caused by TT Cyg having a companion. Such a scenario is considered more likely than interaction with the surrounding ISM, given the morphological properties of the shell. The gas distribution seems to be highly spherically symmetric, as it is indicated by the radial velocity maps and supported by the correlation between the line-of-sight velocity and radial position. The expansion velocity of the gas was found to be 12.6 km s^{-1} , which would set the age of the shell to $\sim 7000 \text{ yr}$ in the case of a freely expanding wind. For the substructure of the shell CO maps further indicate that the material is not smoothly distributed but rather clumpy – simulations suggest clump sizes smaller than $1''$. This influences the abundance of the CO, since in a clumped medium (i.e. locally high densities) the molecules can withstand dissociation by interstellar UV-photons out to larger radii.

Morphology While high resolution data of TT Cyg’s gas component have been available for some time, equivalent information on the dusty part just became available with the Herschel data. Looking at Figs. 4.1 & 4.2, the similarities between the CO interferometric data and the PACS maps are obvious. Not only the size coincides well, a radius of $33''$ is determined from the highest resolved $70 \mu\text{m}$ image, also the variations in the shell brightness along the perimeter show quite a resemblance (e.g. the fainter part to the north). To recognise finer details, however, the resolution of the PACS data is not sufficient. Azimuthal variations in the radial brightness distribution can be seen in Fig. 4.3, as well as in the RAAP in Fig. 4.4. They indicate the already known offset between star and shell centre. Fitting a circle having a radial Gaussian distribution to the PACS observation, indeed yields a displacement of $1.8''$ and -30° P.A., in good agreement with Olofsson et al. (2000). Additionally, the fitting gives a shell radius consistent with the initial measurement, and a shell width (standard deviation of the Gaussian) of $2.4''$, which can be seen as an upper limit, considering that the image is not deconvolved. Thus the relative shell thickness can be given as $\Delta R/R \lesssim 0.07$.

The obtained linear dimensions of the shell of course vary due to the distance uncertainty. In the lower limit (using the P - L -value of 440 pc) the radius and width are $2.2 \times 10^{15} \text{ m}$ and $1.6 \times 10^{15} \text{ m}$, respectively, whereas adopting 620 pc from Bergeat & Chevallier (2005) one gets $3.1 \times 10^{14} \text{ m}$ and $2.2 \times 10^{14} \text{ m}$, respectively.

Fluxes & Temperature The photometric measurements for the object are given in Tab. 4.1. Compared to IRAS data, available at nearby wavelengths, the values are in rough agreement. For the detached shell alone the flux ratio $F_{70}/F_{160} = 1.98$. In the simplest case of a BB model, this corresponds to a dust temperature of 79 K . The more realistic approximation considering the dust emissivity gives a lower T_{dust} of 48 K . When one assumes a grey body with spectral index $\beta = 1.1$, the obtained temperatures are 75 , 62 and 56 K for a λ_0 of 50 , 100 and $200 \mu\text{m}$, respectively.

Models The dust chemistry was selected based on ISO spectral information, shown in Fig. 4.5. While SiC may be present, it is not expected to alter the outcome considerably, compared to a pure amorphous carbon mixture (cf. condensation radii in Fig. 3.7). At

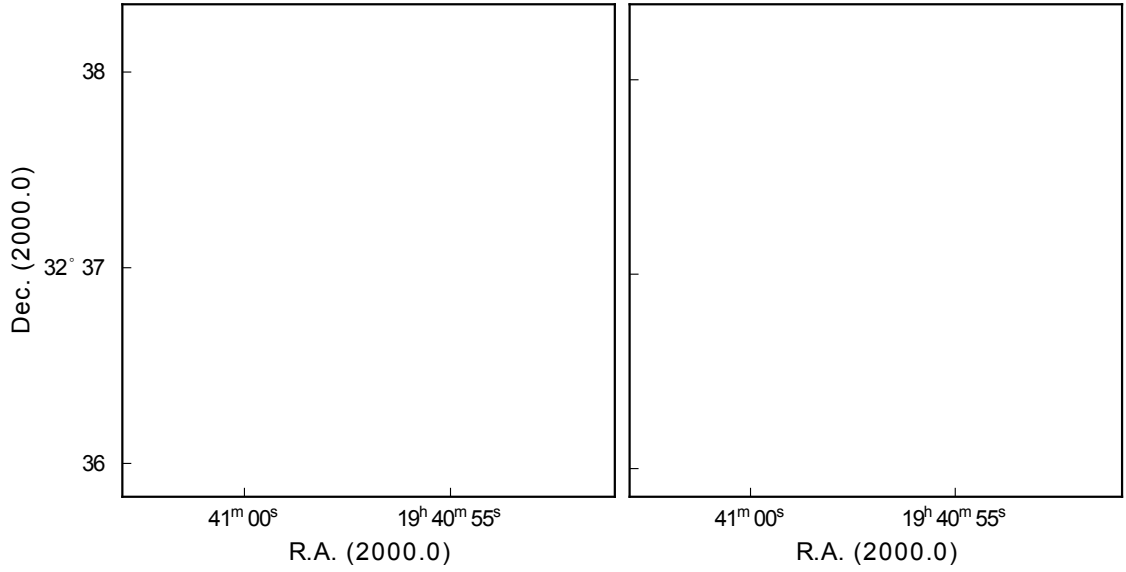


Figure 4.1: PACS maps of TT Cyg in the $70\ \mu\text{m}$ (left) and $160\ \mu\text{m}$ (right) band. The image resolution is $1''/\text{pixel}$ and $2''/\text{pixel}$, respectively.

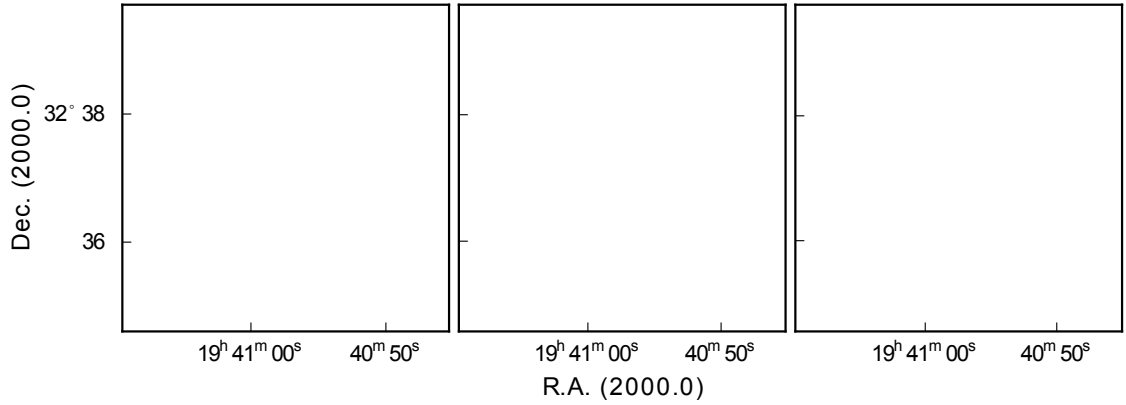


Figure 4.2: SPIRE maps of TT Cyg in the $250\ \mu\text{m}$ (left), $350\ \mu\text{m}$ (centre) and $500\ \mu\text{m}$ (right) bands. The comparatively low spatial resolution at longer wavelengths doesn't allow to identify structural details anymore, however, the very cold foreground ISM cirrus becomes visible. Note also the dots in the background, which are distant galaxies.

	total		shell		IRAS	
$\lambda\ [\mu\text{m}]$	70	160	70	160	60	100
Flux [Jy]	3.10	1.42	1.65	0.83	3.45	4.41

Table 4.1: Photometry of TT Cyg, given for the whole object, the detached shell only, and IRAS measurements for comparison.

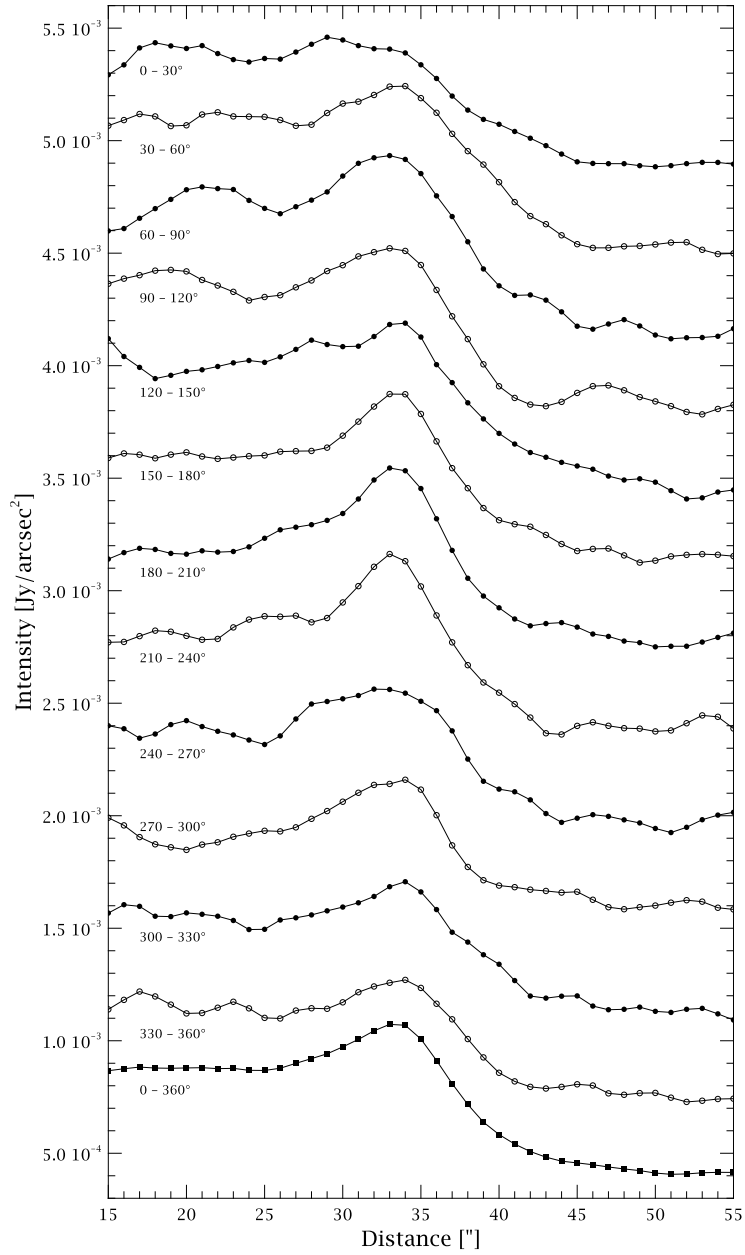


Figure 4.3: Radial profiles of TT Cyg ($70 \mu\text{m}$), each averaged over 30° in P.A. as indicated. At the bottom is the average over the full circumference. The centre is set to the stellar position – shifts in the shell peak position thus indicate a displacement of the shell centre and also cause a broadening of the shell feature (cf. Fig. 3.2).

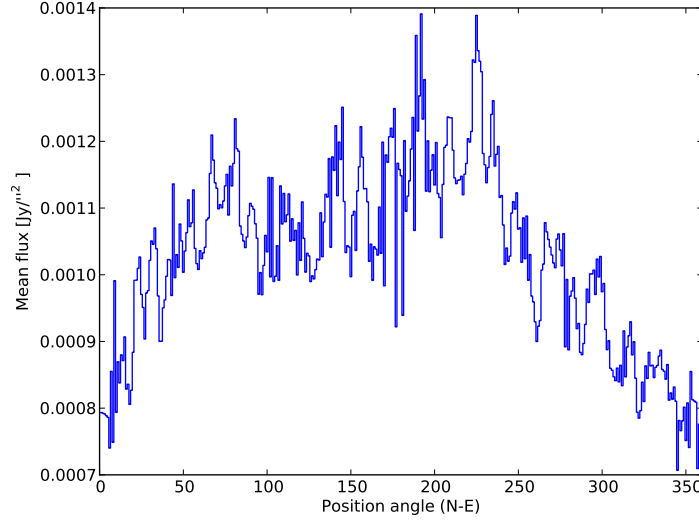


Figure 4.4: RAAP of TT Cyg ($70 \mu\text{m}$) in the annulus between 30 and $35''$. The global profile trend is mainly due to the actual azimuthal intensity variations of the shell, but also bears the effect of the small displacement with respect to the star.

typical abundances of 5–10% its influence on the radial brightness profile is negligible, therefore only the Preibisch optical constants were adopted. To get the proper scaling, M_{bol} from Bergeat & Chevallerier (2005) and, for consistency, the distance therein were adopted.

Using the appropriate COMARCS model as the external source, a model fit (see Fig. 4.6) gives a shell thickness of $Y = 1.9$, and a temperature at the inner boundary of 51 K, dropping to 40 K at the outer edge (Fig. 4.8). For the optical depth $\tau_{0.55\mu\text{m}} = 0.006$ is obtained. Furthermore, the solution of the radiatively driven wind suggests a mass-loss rate of $\dot{M} = 8 \times 10^{-7} M_{\odot} \text{yr}^{-1}$, when adopting a gas-to-dust mass ratio $\Psi = 0.005$ and a dust grain bulk density of 1.85g cm^{-3} (Preibisch et al. 1993). For the inner, unresolved shell the parameters cannot be well constrained, since the only feedback one gets in the present case is the central (~ 5 – $10''$) peak brightness distribution. Here, a dust envelope with a condensation temperature of 1000 K and a $\tau_{0.55\mu\text{m}}$ of 0.4 fits best, with the temperature having a relatively small effect compared to the opacity. A 2D representation of the computed model can be seen in Fig. 4.7.

Summary A $33''$ dust shell around TT Cyg is prominently visible in both PACS bands and the respective radial profiles. Radiative transfer modelling yields a MLR of $8 \times 10^{-7} M_{\odot} \text{yr}^{-1}$ for a mass outburst 7000–8000 years ago, possibly related to a recent He-shell flash. Previous studies give MLRs of $2 \times 10^{-6} M_{\odot} \text{yr}^{-1}$ (Kerschbaum et al. 2010, also based on Herschel data) and $10^{-5} M_{\odot} \text{yr}^{-1}$ over a period of ~ 500 years ($M_{\text{shell}} = 0.007 M_{\odot}$), according to CO observations (Olofsson et al. 2000). For the dust mass in the shell Schöier et al. (2005) find $4.3 \times 10^{-4} M_{\odot}$. That the flow of matter

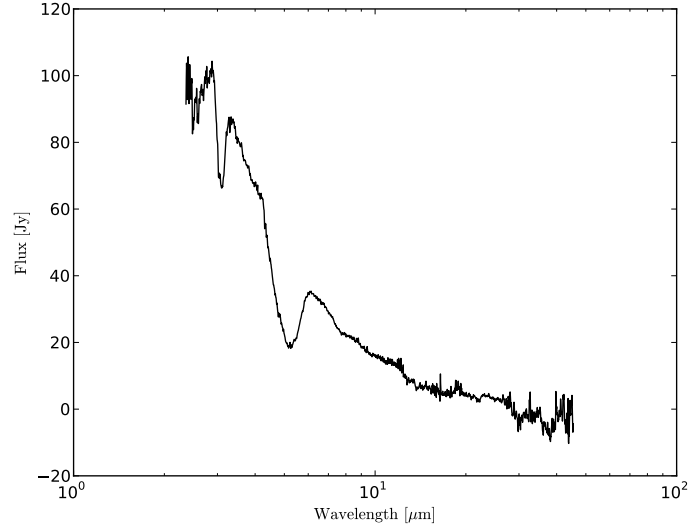


Figure 4.5: ISO SWS spectrum of TT Cyg, used to get an estimate on the chemical composition of the dust. It may show a slight indication of SiC (feature at $11.2 \mu\text{m}$). MgS on the other hand, which would cause a signature at $\sim 30 \mu\text{m}$ does not seem to be present.

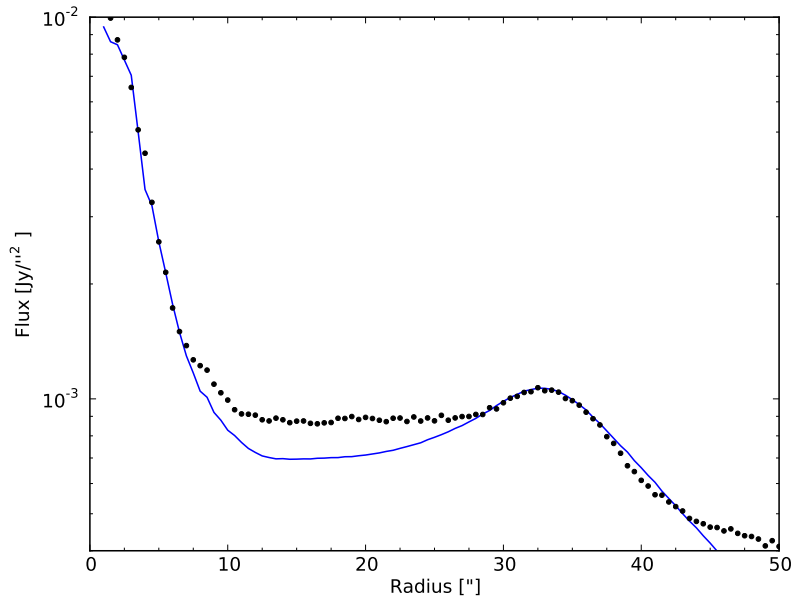


Figure 4.6: Best fitting model radial brightness profile (blue line) at $70 \mu\text{m}$ compared to the AARP of TT Cyg (black circles). The observed shell peaks at $\sim 33''$. Model parameters for the detached dust are $T_{\text{dust}} = 51 \text{ K}$, $\tau_{0.55\mu\text{m}} = 0.006$ and $Y = 1.9$ for a pure amC composition.

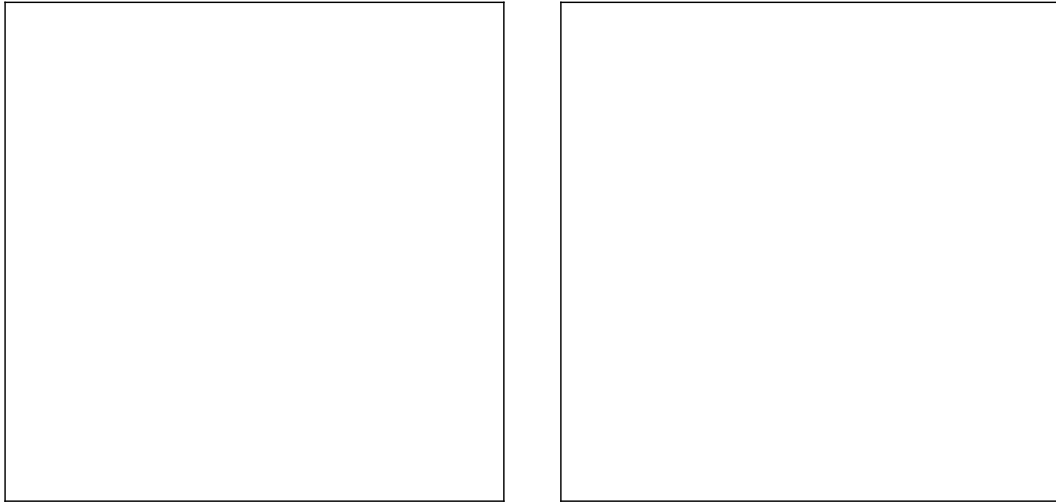


Figure 4.7: 2D synthetic brightness maps at $70\ \mu\text{m}$ of the best fit TT Cyg model, for the original output (left) and after the convolution with the PACS PSF (right). Created from the radial brightness profile in Fig. 4.6.

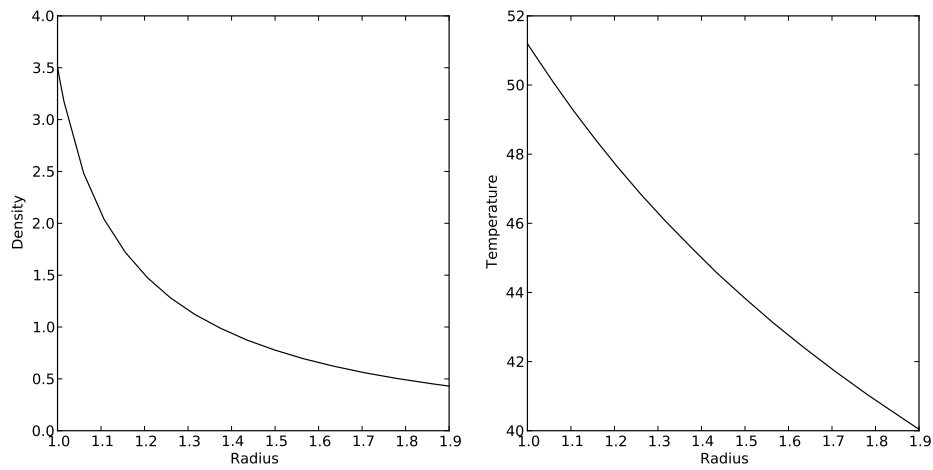


Figure 4.8: Radial profiles of the normalised, dimensionless density (left) and dust temperature (right) from the inner shell boundary outwards. Results of the best fitting radiatively driven wind model of TT Cyg.

hasn't completely ceased since this ejection is indicated by the remaining faint emission inside the ring, which could not be fitted using the single shell model. Currently the MLR is low, at $\dot{M} = 3 \times 10^{-8} M_{\odot} \text{ yr}^{-1}$ and a wind velocity of 3.8 km s^{-1} (Olofsson et al. 2000). Concerning the dust temperature, the obtained values are rather high, compared to other modelling results. By fitting the SED, Schöier et al. (2005) obtain 39 K and from more detailed modelling Kerschbaum et al. (2010) get 28 K. The present model result is, however, in agreement with the temperature estimated from the F_{70}/F_{160} flux ratio when using dust emissivity (Draine 1981).

The PACS observations show that the gas and the dust component around TT Cyg are cospatial. Assuming a radiatively driven wind one would, however, expect the dust shell to be at larger distances due to velocity drift. This discrepancy suggests that the shell(s) are not expanding freely. Interaction with an older and slower wind could explain this situation. Schöier et al. (2005) analysed a sample of 7 AGB stars showing detached shells in CO. For the mass of the shells they found that it increases with the radial distance. The expansion velocity on the other hand, shows a vague negative correlation with the size. Both effects are interpreted as indicators for a wind-wind interaction, where the faster young wind is decelerated by an old shell, while sweeping up material. Thus, wind-wind interaction could be a common cause to observed detached shells. As argued by Olofsson et al. (2000), wind-ISM interaction is less likely in the present case, although the space motion is mostly oriented in the radial direction, which would be compatible with the observed shape (Wareing et al. 2006). Also the offset between the stellar position and the shell centre, which could in principle be due to ISM interaction, is speculated to be caused by a companion star. Nevertheless, it is possible that TT Cyg has features that are a result of its space motion, similar to the faint “tail” detected by AKARI for U Hya (Izumiura et al. 2011).

4.1.2 UX Draconis

UX Dra (IRAS 19233+7627) is a carbon star with a MK spectral type C7,3. As a semiregular variable (SRa) it pulsates with a period of 168 days and an amplitude of 1.16^{mag} in the V -band ($V_{\text{max}} = 5.94^{\text{mag}}$, $V_{\text{min}} = 7.10^{\text{mag}}$). It lies in region “VII” (*variable stars with more evolved C-rich circumstellar shells*) of the IRAS two colour diagram, with measured IRAS colours $[12]-[25] = -1.33$ and $[25]-[60] = -1.53$. 3090 K is given as the stellar temperature by Bergeat et al. (2001). The bolometric magnitudes are given in Bergeat & Chevallier (2005) as $m_{\text{bol}} = 3.16^{\text{mag}}$ and $M_{\text{bol}} = -5.53^{\text{mag}}$. The corresponding luminosity is $12\,700 L_{\odot}$. For the C/O ratio of the atmosphere Lambert et al. (1986) derived 1.05.

The Hipparcos distance of UX Dra is rather well constrained to 390 pc $-40, +50$ pc. Values obtained from P - L -relations again deviate, depending on the applied relation. The relation from Groenewegen & Whitelock (1996) gives 270 pc, whereas the one from Knapp et al. (2003) yields 370 pc and is thus in good agreement with the parallax measurements. At the upper end of the scale, 545 pc are cited by Bergeat & Chevallier (2005). For the following analysis the Hipparcos distance of 390 pc is adopted, for the modelling the Bergeat values are compared, too.

Contrary to TT Cyg, UX Dra is not that well studied and hence has a shorter historical record of dedicated studies. One noteworthy early discovery is the detection

of technetium (Hackos 1974; Abia et al. 2002), whose occurrence is usually tied to a recent thermal pulse/ 3^{rd} dredge-up event. Olofsson et al. (1987) observed UX Dra in CO, but no indication for detached molecular line emission is seen in the radial velocity profiles. A present day mass-loss was confirmed, however. According to more recent measurements, the MLR is $1.6 \times 10^{-7} M_{\odot} \text{ yr}^{-1}$, with a terminal wind expansion velocity of 4.0 km s^{-1} (Schöier & Olofsson 2001).

Concerning IR missions, UX Dra was, apart from being detected by IRAS, also observed by ISO. Circumstellar structures of dust were not clearly resolved, but the $60 \mu\text{m}$ data (see Fig. 4.9) give a clue that there is some extended dust emission, as is also suggested by Young et al. (1993). A first presentation of Herschel data is given in Mecina et al. (2011).

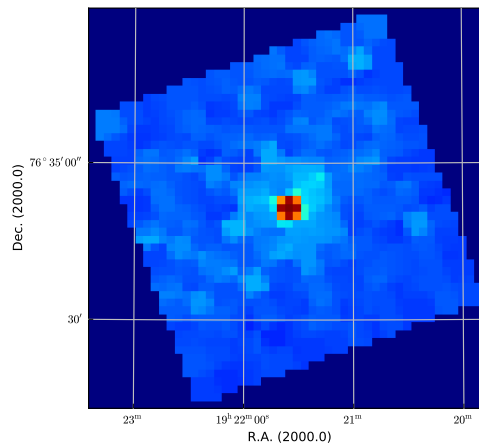


Figure 4.9: ISO PHT22 image of UX Dra at $60 \mu\text{m}$. Indication of extended emission.

Morphology In the PACS maps the main detached emission is detected north of the central source. The bright and well defined part is constrained between approximately -70° – 70° P.A. The arc noticeably deviates from a circularly symmetric shape, hence only an average distance can be given. From the AARP (Fig. 4.12) a radius of $77''$ is derived. In the southern part there is only very faint emission, particularly at $160 \mu\text{m}$. It appears to form, together with the northern arc, a discontinuous, roughly circular structure. To the S-W there is a bright blob, in both the 70 and $160 \mu\text{m}$ band, which appears to be part of the detached dust emission. Going to longer wavelengths, there is no or only very poor detection of the circumstellar emission in the SPIRE maps.

Fluxes & Temperature The PACS photometry (Fig. 4.2) is in agreement with the IRAS data. Since there is no closed detached shell, the extended dust emission was measured only where a clear structure can be observed, i.e. the northern arc, ranging from -70° – 70° in position angle in the 65 – $95''$ radial interval. The obtained flux ratio or colour $F_{70}/F_{160} = 1.61$ suggests a blackbody temperature of 67 K , whereas with an adjusted dust emissivity one gets 43 K . When considering grey bodies ($\beta = 1.1$), the

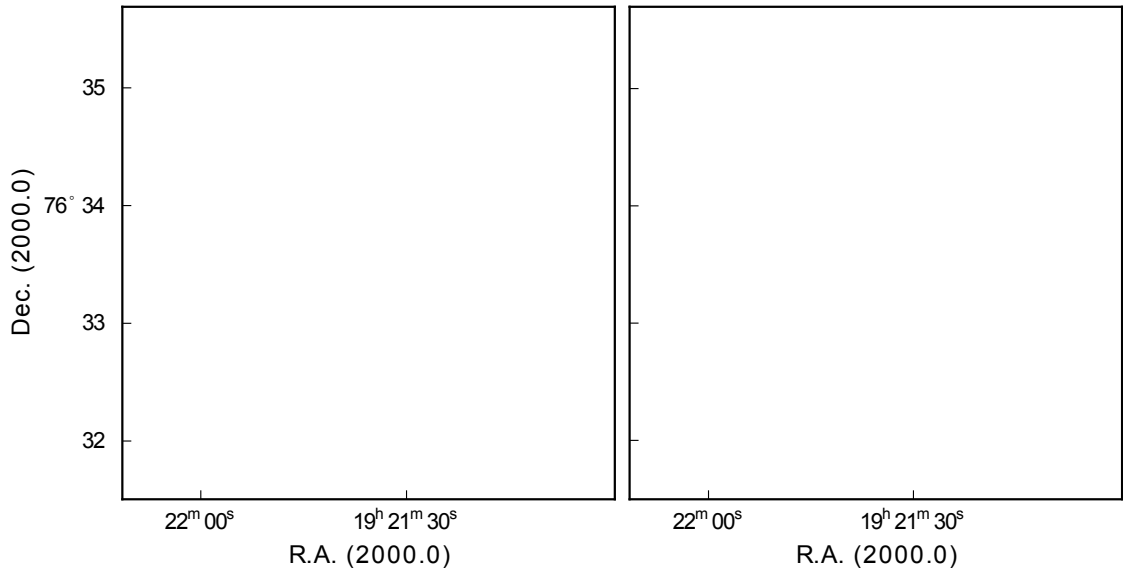


Figure 4.10: PACS maps of UX Dra in the $70\ \mu\text{m}$ (left) and $160\ \mu\text{m}$ (right) band. The image resolution is $1''$ and $2''$, respectively.

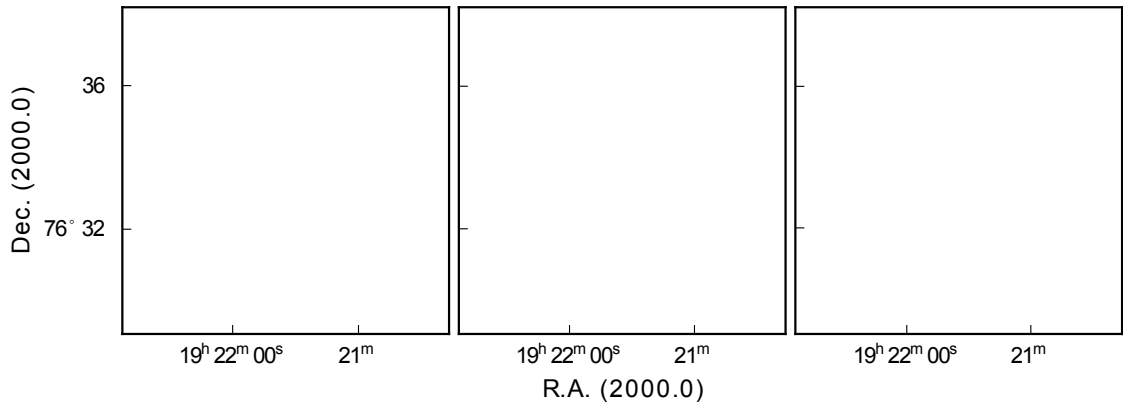


Figure 4.11: SPIRE maps of UX Dra in the $250\ \mu\text{m}$ (left), $350\ \mu\text{m}$ (centre) and $500\ \mu\text{m}$ (right) bands. No clear detection of the detached dust emission.

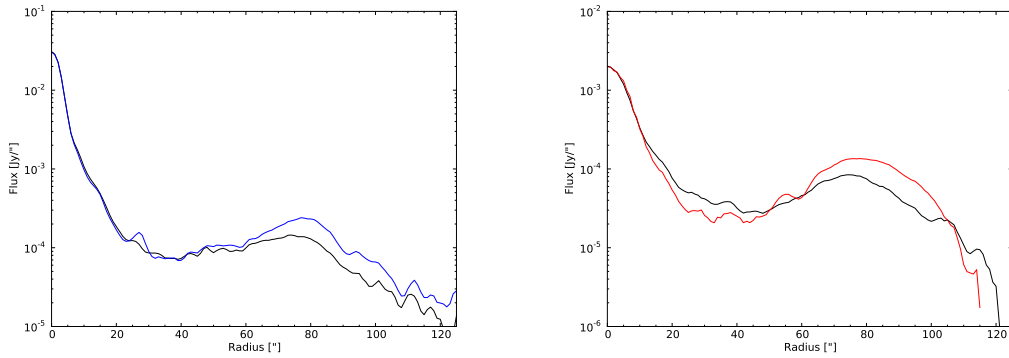


Figure 4.12: AARPs of UX Dra. *Left*: averaged from -70° – 70° (blue) and over the whole P.A. (black) at $70\ \mu\text{m}$. *Right*: averaged from -70° – 70° (green) and over the whole P.A. (black) at $160\ \mu\text{m}$.

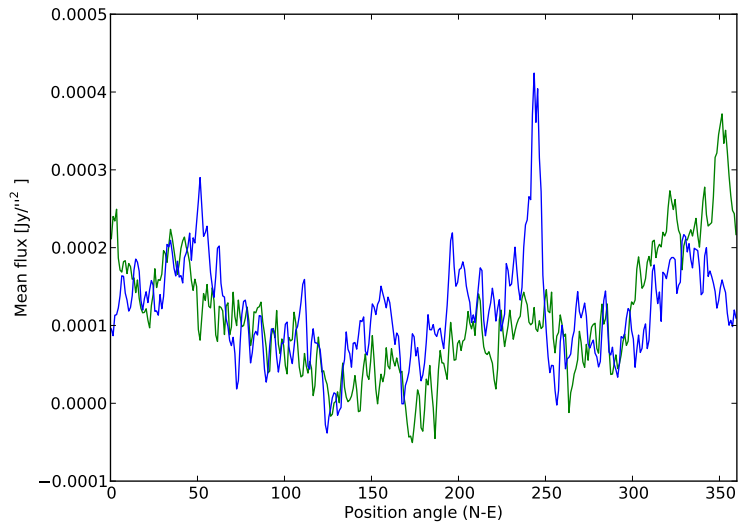


Figure 4.13: RAAP of UX Dra for the annuli $58''$ – $73''$ (blue) and $73''$ – $90''$ (green).

temperatures are between those values, namely 64, 55 and 50 K for a λ_0 of 50, 100 and 200 μm , respectively. The generally lower dust temperatures, compared to those of TT Cyg, are plausible considering the larger distance of the dust to the star (\approx factor 1.5–2), although the higher luminosity/stellar temperature of UX Dra counteracts this effect to some degree.

λ [μm]	total		shell		IRAS	
	70	160	70	160	60	100
Flux [Jy]	4.15	1.62	1.06	0.66	4.74	3.82

Table 4.2: Photometry of UX Dra, given for the whole object, the northern part of the arc (P.A. = -70° – 70°), and IRAS measurements for comparison.

Models Since UX Dra does not show spherically symmetric emission, DUSTY modeling of the detected structure cannot be expected to yield as much useful information as in the case of TT Cyg. However, at least the temperature can be estimated, as it is determined solely by the shell/arc radial distance, and not by the radial shape or brightness. For the dust composition a pure amorphous carbon mixture (Preibisch) was used, as the IRAS low resolution spectrum (ISO spectral data is not available) shows no compelling evidence of either SiC or MgS (see Fig. 4.14). The luminosity of $6300 L_\odot$ was calculated using $M_{\text{bol}} = 3.16$ from Bergeat & Chevallier (2005) and the Hipparcos distance (390 pc). For the inner hot envelope again a 1000 K shell was fitted, where a τ of 0.17 gave the best result. Eventually, a matching shell position is found for the detached emission with $T_{\text{eff}} = 51$ K. Except the shell radius, the profile (for the northern section) is very poorly reproduced, as can be seen in Fig. 4.15, hence the temperature remains the only parameter that can be reasonably determined.

Summary The ambiguous shape of the detached dust emission allows for different interpretations of the formation process. The most prominent structure to the north could suggest an ISM-wind interaction. However, the proper motion of the star is headed towards the west ($\mu = 6.65$ mas/yr, P.A. = 262°) and the radial velocity is low (6 km s^{-1}). Thus, despite not having calculated the actual space motion, it is very unlikely that the observed shape is a bow shock at the ISM-wind interface. Alternatively, the arc can be explained as due to a heavy modulation in \dot{M} , potentially enhanced by the interaction with a slower older wind. The observed shape would, however, suggest a highly anisotropic ejection of the material. An effect, that could be amplified by an inhomogeneous surrounding medium (old wind or ISM). Adding another possibility: Vetesnik (1984) speculates that UX Dra could be a binary. If so, could the companion cause the observed dust distribution?

The lack of corresponding detached CO line emission may be a consequence of the quite advanced age and size of the structure. At the radius of 4.6×10^{15} m the arc is roughly 10 000 years old (adopting a generic expansion velocity of 15 km s^{-1} , since no measurements exist for the detached part) – at this point photodissociation is likely to be effective, given a typical photodissociation timescale of $\sim 10^3$ yr (van Dishoeck & Black 1988).

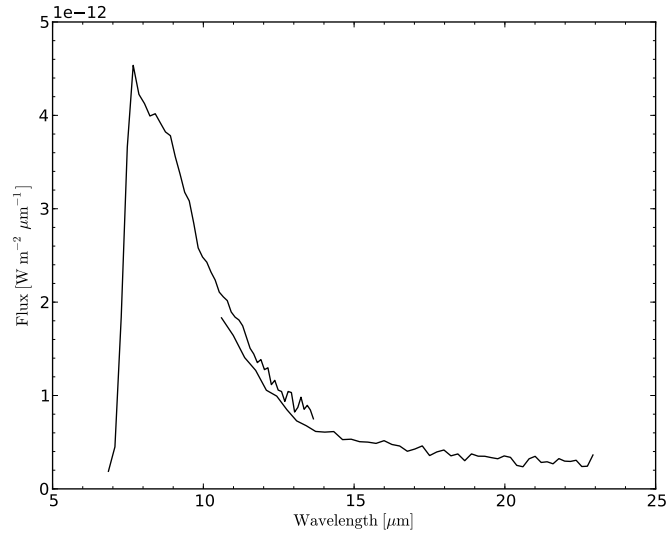


Figure 4.14: IRAS low resolution spectrum of UX Dra.

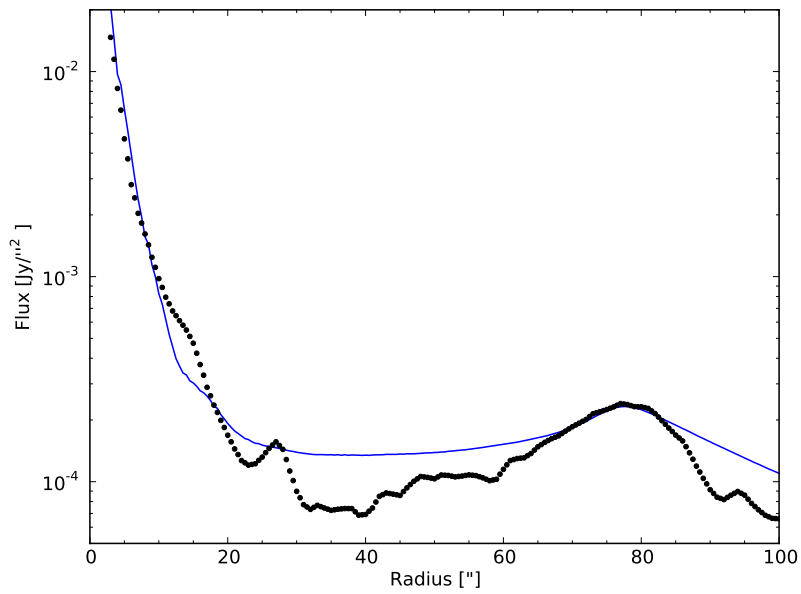


Figure 4.15: Best fitting model radial brightness profile (blue line) at $70 \mu m$ compared to the AARP (-70° – 70° P.A.) of UX Dra (black circles). The shell peaks at $\sim 77''$. Model parameters for the detached dust are $T_{\text{dust}} = 51 \text{ K}$, $\tau_{0.55 \mu m} = 0.002$ and $Y = 25$ for a pure amC composition. Due to the smaller azimuthal averaging angle, little features (e.g. PSF artefacts) are more prominent in the profile, causing considerable fluctuations.

4.2 Conclusion & Prospects

In this thesis, the mass-loss of AGB stars was investigated from a morphological perspective. Up-to-date observational material in the far infrared, obtained by the currently operational *Herschel Space Observatory* was used to study the dust emission surrounding the two carbon stars TT Cyg and UX Dra. Dust properties and characteristics of the mass-loss were derived from straightforward estimates and radiative transfer modelling, using the DUSTY code.

The resolution of the PACS photometer data for the first time allows for a very detailed look at the morphological characteristics of the circumstellar dust component. However, data reduction started very early into the mission, where only limited information and experience was gathered about the proper processing methods. The tricky nature of the observed objects and the complexity of the instrumental effects (drift, etc.) required some adaptations to the standard pipeline in order to take full advantage of Herschel's capabilities. Regarding map-making, the *Scanamorphos* routine turned out to provide the best results, especially when it comes to sensitivity. Future improvements of the imaging results can be expected – more accurate photometry, due to the gradually advancing calibration data, as well as enhanced maps as a result of more sophisticated map-making algorithms (SANEPIC, TAMASIS). Additionally, re-observations could help detect fainter emission and confirm present features.

For TT Cyg the PACS maps, particularly the higher resolved image at $70\ \mu\text{m}$, show a spherically symmetric detached dust shell. It coincides to a remarkable degree with interferometric CO line data. The geometrical and morphological details also agree with previous knowledge. The missing drift between the dust and the gas component is interpreted as being due to a wind-wind interaction. The lower resolving and less sensitive $160\ \mu\text{m}$ map is not as yielding concerning morphological information. It is, however, essential for a straightforward temperature estimate based on a flux ratio. Opposed to TT Cyg, the detection and resolution of a detached structure around UX Dra is a first. An explanation of the formation scenario for the dust arc(s), for which no molecular counterpart is known, is difficult, but an ISM-wind interaction seems unlikely. Here, additional observing time could shed more light on the true shape of the dust emission. The radiative transfer modelling yields results that are roughly consistent with previous studies. Nevertheless, the quite simplistic approach is not expected to provide very reliable results and leaves much space for improvements, such as taking into account also the spectral information. While for TT Cyg the model reproduced the observations acceptably due to the symmetric nature of the object, the emission around UX Dra seems too complex to be calculated with a simple 1D approach.

The two objects presented in this work are only examples of a larger sample of detached shell objects observed in the MESS program. Their analysis will provide more insight on the dust properties around evolved stars and consequently a better understanding of the responsible mass-loss process. For the (sub-)mm regime good data are already available for some sources of interest. In the future, the already operational ALMA facility will further improve the observational material in both resolution and sensitivity. As for upcoming IR space missions, SPICA will be the next big step. Having an actively cooled primary mirror, the Herschel successor can be expected to provide greatly enhanced sensitivity for faint extended emission.

Bibliography

- Abia, C., Domínguez, I., Gallino, R., et al. 2002, *ApJ*, 579, 817
- Alcock, C., Allsman, R. A., Axelrod, T. S., et al. 1995, *AJ*, 109, 1653
- Andersen, A. C., Loidl, R., & Höfner, S. 1999, *A&A*, 349, 243
- Aringer, B., Girardi, L., Nowotny, W., Marigo, P., & Lederer, M. T. 2009, *A&A*, 503, 913
- Bastian, U. & Hefele, H. 2005, in *ESA Special Publication, Vol. 576, The Three-Dimensional Universe with Gaia*, ed. C. Turon, K. S. O'Flaherty, & M. A. C. Perryman, 215
- Bergeat, J. & Chevallier, L. 2005, *A&A*, 429, 235
- Bergeat, J., Knapik, A., & Rutily, B. 2001, *A&A*, 369, 178
- Biermann, L. 1951, *Zeitschrift für Astrophysik*, 29, 274
- Boothroyd, A. I. & Sackmann, I. 1988, *ApJ*, 328, 641
- Bowen, G. H. 1988, *ApJ*, 329, 299
- Burbidge, E. M., Burbidge, G. R., Fowler, W. A., & Hoyle, F. 1957, *Reviews of Modern Physics*, 29, 547
- Cantalupo, C. M., Borrill, J. D., Jaffe, A. H., Kisner, T. S., & Stompor, R. 2010, *ApJS*, 187, 212
- Cherchneff, I. & Tielens, A. G. G. M. 1994, in *Circumstellar Media in Late Stages of Stellar Evolution*, ed. R. E. S. Clegg, I. R. Stevens, & W. P. S. Meikle, 232
- Cox, N. L. J., Kerschbaum, F., van Marle, A.-J., et al. 2012, *A&A*, 537, A35
- Cutri, R. M., Skrutskie, M. F., van Dyk, S., et al. 2003, *VizieR Online Data Catalog*, 2246, 0
- de Graauw, T., Helmich, F. P., Phillips, T. G., et al. 2010, *A&A*, 518, L6
- Dominik, C., Sedlmayr, E., & Gail, H. 1993, *A&A*, 277, 578
- Draine, B. T. 1981, *ApJ*, 245, 880
- Engelke, C. W. 1992, *AJ*, 104, 1248
- Epchtein, N., de Batz, B., Copet, E., et al. 1994, *Ap&SS*, 217, 3

- Feast, M. W., Glass, I. S., Whitelock, P. A., & Catchpole, R. M. 1989, MNRAS, 241, 375
- Ferrarotti, A. S. & Gail, H. 2006, A&A, 447, 553
- Fox, M. W. & Wood, P. R. 1982, ApJ, 259, 198
- Fruchter, A. S. & Hook, R. N. 2002, PASP, 114, 144
- Gail, H. 2010, in Lecture Notes in Physics, Vol. 815, Astromineralogy, ed. T. Henning (Berlin, Heidelberg: Springer Berlin Heidelberg), 61–141
- Geise, K. M., Ueta, T., Speck, A. K., Izumiura, H., & Stencel, R. E. 2010, in Bulletin of the American Astronomical Society, Vol. 42, American Astronomical Society Meeting Abstracts #215, 431.14
- Gilman, R. C. 1969, ApJ, 155, L185
- González Delgado, D., Olofsson, H., Schwarz, H. E., Eriksson, K., & Gustafsson, B. 2001, A&A, 372, 885
- González Delgado, D., Olofsson, H., Schwarz, H. E., et al. 2003, A&A, 399, 1021
- Griffin, M. J., Abergel, A., Abreu, A., et al. 2010, A&A, 518, L3
- Groenewegen, M. A. T. & de Jong, T. 1994, A&A, 282, 115
- Groenewegen, M. A. T., Sevenster, M., Spoon, H. W. W., & Pérez, I. 2002, A&A, 390, 511
- Groenewegen, M. A. T., Waelkens, C., Barlow, M. J., et al. 2011, A&A, 526, 162
- Groenewegen, M. A. T. & Whitelock, P. A. 1996, MNRAS, 281, 1347
- Gustafsson, B. & Höfner, S. 2004, in Asymptotic Giant Branch Stars, ed. H. J. Habing & H. Olofsson, A&A Library (Springer), 149–245
- Habing, H. J. 1996, A&ARv, 7, 97
- Habing, H. J. & Olofsson, H., eds. 2004, Asymptotic giant branch stars, Astronomy and Astrophysics library (Springer)
- Habing, H. J., Tignon, J., & Tielens, A. G. G. M. 1994, A&A, 286, 523
- Hackos, W. 1974, PASP, 86, 78
- Herman, J. & Habing, H. J. 1985, A&AS, 59, 523
- Herwig, F. 2005, ARA&A, 43, 435
- Höfner, S. 2007, in Astronomical Society of the Pacific Conference Series, Vol. 378, Why Galaxies Care About AGB Stars: Their Importance as Actors and Probes, ed. F. Kerschbaum, C. Charbonnel, & R. F. Wing, 145

- Höfner, S. 2008, A&A, 491, L1
- Höfner, S. & Dorfi, E. A. 1997, A&A, 319, 648
- Iben, I. 1981, ApJ, 246, 278
- Iben, I. 1985, QJRAS, 26, 1
- Iben, I. & Renzini, A. 1983, ARA&A, 21, 271
- Ivezic, Z. & Elitzur, M. 1995, ApJ, 445, 415
- Ivezic, Z. & Elitzur, M. 1997, MNRAS, 287, 799
- Ivezic, Z., Nenkova, M., & Elitzur, M. 1999, User Manual for DUSTY
- Izumiura, H., Hashimoto, O., Kawara, K., Yamamura, I., & Waters, L. B. F. M. 1996, A&A, 315, L221
- Izumiura, H., Ueta, T., Yamamura, I., et al. 2011, A&A, 528, 29
- Jager, C., Mutschke, H., & Henning, T. 1998, A&A, 332, 291
- Jorissen, A., Mayer, A., van Eck, S., et al. 2011, A&A, 532, 135
- Karakas, A. I. 2011, in Astronomical Society of the Pacific Conference Series, Vol. 445, Why Galaxies Care about AGB Stars II: Shining Examples and Common Inhabitants, ed. F. Kerschbaum, T. Lebzelter, & R. F. Wing, 3
- Kerschbaum, F. & Hron, J. 1992, A&A, 263, 97
- Kerschbaum, F. & Hron, J. 1994, A&AS, 106, 397
- Kerschbaum, F., Ladjal, D., Ottensamer, R., et al. 2010, A&A, 518, L140
- Kerschbaum, F., Olofsson, H., & Hron, J. 1996, A&A, 311, 273
- Kessler, M. F., Steinz, J. A., Anderegg, M. E., et al. 1996, A&A, 315, L27
- Kim, S.-H., Martin, P. G., & Hendry, P. D. 1994, ApJ, 422, 164
- Knapp, G. R., Pourbaix, D., Platais, I., & Jorissen, A. 2003, A&A, 403, 993
- Lambert, D. L., Gustafsson, B., Eriksson, K., & Hinkle, K. H. 1986, ApJS, 62, 373
- Lebzelter, T., Kerschbaum, F., & Hron, J. 1995, A&A, 298, 159
- Lebzelter, T. & Obbrugger, M. 2009, Astronomische Nachrichten, 330, 390
- Lindqvist, M., Olofsson, H., Lucas, R., et al. 1999, A&A, 351, L1
- Longdon, N., ed. 1984, ESA Special Publication, Vol. 1070, European Space Science : Horizon 2000

- Loup, C., Forveille, T., Omont, A., & Paul, J. F. 1993, *A&AS*, 99, 291
- Maercker, M., Olofsson, H., Eriksson, K., Gustafsson, B., & Schöier, F. L. 2010, *A&A*, 511, 37
- Marengo, M., Busso, M., Silvestro, G., Persi, P., & Lagage, P. O. 1999, *A&A*, 348, 501
- Mathis, J. S., Rumpl, W., & Nordsieck, K. H. 1977, *ApJ*, 217, 425
- Mayer, A., Jorissen, A., Kerschbaum, F., et al. 2011, *A&A*, 531, L4
- Mecina, M., Kerschbaum, F., Ladjal, D., et al. 2011, in *Astronomical Society of the Pacific Conference Series*, Vol. 445, *Why Galaxies Care about AGB Stars II: Shining Examples and Common Inhabitants*, ed. F. Kerschbaum, T. Lebzelter, & R. F. Wing, 353
- Millar, T. J. 2004, in *Asymptotic Giant Branch Stars*, ed. H. J. Habing & H. Olofsson, *A&A Library* (Springer), 247–289
- Min, M., Hovenier, J. W., & de Koter, A. 2003, *A&A*, 404, 35
- Molster, F., Waters, L., & Kemper, F. 2010, in *Lecture Notes in Physics*, Vol. 815, *Astromineralogy*, ed. T. Henning (Berlin, Heidelberg: Springer Berlin Heidelberg), 143–201
- Murakami, H., Baba, H., Barthel, P., et al. 2007, *PASJ*, 59, 369
- Neugebauer, G., Habing, H. J., van Duinen, R., et al. 1984, *ApJ*, 278, L1
- Neugebauer, G. & Leighton, R. B. 1969, *NASA Special Publication*, 3047
- Nowotny, W., Aringer, B., Höfner, S., & Lederer, M. T. 2011, *A&A*, 529, A129
- Nowotny, W., Höfner, S., & Aringer, B. 2010, *A&A*, 514, A35
- Olofsson, H. 2004, in *Asymptotic Giant Branch Stars*, ed. H. J. Habing & H. Olofsson, *A&A Library* (Springer), 325–410
- Olofsson, H., Bergman, P., Eriksson, K., & Gustafsson, B. 1996, *A&A*, 311, 587
- Olofsson, H., Bergman, P., Lucas, R., et al. 1998, *A&A*, 330, L1
- Olofsson, H., Bergman, P., Lucas, R., et al. 2000, *A&A*, 353, 583
- Olofsson, H., Carlstrom, U., Eriksson, K., Gustafsson, B., & Willson, L. A. 1990, *A&A*, 230, L13
- Olofsson, H., Eriksson, K., & Gustafsson, B. 1987, *A&A*, 183, L13
- Olofsson, H., González Delgado, D., Kerschbaum, F., & Schöier, F. L. 2002, *A&A*, 391, 1053

- Olofsson, H., Maercker, M., Eriksson, K., Gustafsson, B., & Schöier, F. 2010, *A&A*, 515, 27
- Ottensamer, R. & Kerschbaum, F. 2008, in *Society of Photo-Optical Instrumentation Engineers (SPIE) Conference Series*, Vol. 7019, *Society of Photo-Optical Instrumentation Engineers (SPIE) Conference Series*
- PACS ICC. 2010, PACS photometer - Prime and Parallel scan mode release note v1.2, PICC-ME-TN-035
- PACS OM. 2011, PACS Observer's Manual v2.4, HERSCHEL-HSC-DOC-0832
- Paczynski, B. 1970, *Acta Astronomica*, 20, 47
- Paczynski, B. 1975, *ApJ*, 202, 558
- Perryman, M. A. C., Lindgren, L., Kovalevsky, J., et al. 1997, *A&A*, 323, L49
- Pilbratt, G. L., Riedinger, J. R., Passvogel, T., et al. 2010, *A&A*, 518, L1
- Poglitsch, A., Waelkens, C., Geis, N., et al. 2010, *A&A*, 518, L2
- Preibisch, T., Ossenkopf, V., Yorke, H. W., & Henning, T. 1993, *A&A*, 279, 577
- Roeser, S., Demleitner, M., & Schilbach, E. 2010, *AJ*, 139, 2440
- Roussel, H. 2011, *A&A*, submitted
- Rowan-Robinson, M. 1980, *ApJS*, 44, 403
- Salpeter, E. E. 1955, *ApJ*, 121, 161
- Salpeter, E. E. 1977, *ARA&A*, 15, 267
- Samus, N. N., Durlevich, O. V., & et al. 2009, *VizieR Online Data Catalog*, 1, 2025
- Schöier, F. L., Lindqvist, M., & Olofsson, H. 2005, *A&A*, 436, 633
- Schöier, F. L. & Olofsson, H. 2001, *A&A*, 368, 969
- Schwarzschild, M. & Härm, R. 1965, *ApJ*, 142, 855
- Secchi, A. 1868, *MNRAS*, 28, 196
- Sedlmayr, E. 1994, in *Lecture Notes in Physics*, Berlin Springer Verlag, Vol. 428, IAU Colloq. 146: *Molecules in the Stellar Environment*, ed. U. G. Jorgensen, 163
- Starck, J. L., Abergel, A., Aussel, H., et al. 1999, *A&AS*, 134, 135
- Udalski, A., Szymanski, M., Kaluzny, J., et al. 1993, *Acta Astronomica*, 43, 289
- van der Veen, W. E. C. J. & Habing, H. J. 1988, *A&A*, 194, 125
- van Dishoeck, E. F. & Black, J. H. 1988, *ApJ*, 334, 771

- van Leeuwen, F. 2007, *A&A*, 474, 653
- Vassiliadis, E. & Wood, P. R. 1993, *ApJ*, 413, 641
- Vetevnik, M. 1984, *Bulletin of the Astronomical Institutes of Czechoslovakia*, 35, 65
- Wachter, A., Schröder, K., Winters, J. M., Arndt, T. U., & Sedlmayr, E. 2002, *A&A*, 384, 452
- Wagenhuber, J. & Groenewegen, M. A. T. 1998, *A&A*, 340, 183
- Wallerstein, G. & Knapp, G. R. 1998, *ARA&A*, 36, 369
- Wareing, C. J., Zijlstra, A. A., Speck, A. K., et al. 2006, *MNRAS*, 372, L63
- Werner, M. W., Roellig, T. L., Low, F. J., et al. 2004, *ApJS*, 154, 1
- Willems, F. J. & de Jong, T. 1988, *A&A*, 196, 173
- Winters, J. M., Le Bertre, T., Jeong, K. S., Helling, C., & Sedlmayr, E. 2000, *A&A*, 361, 641
- Woitke, P. 2006, *A&A*, 460, L9
- Woitke, P. 2007, in *Astronomical Society of the Pacific Conference Series*, Vol. 378, *Why Galaxies Care About AGB Stars: Their Importance as Actors and Probes*, ed. F. Kerschbaum, C. Charbonnel, & R. F. Wing, 156
- Wood, P. R. 1990, in *From Miras to Planetary Nebulae: Which Path for Stellar Evolution?*, ed. M. O. Mennessier & A. Omont, 67–84
- Wood, P. R., Alcock, C., Allsman, R. A., et al. 1999, in *IAU Symposium*, Vol. 191, *Asymptotic Giant Branch Stars*, ed. T. Le Bertre, A. Lebre, & C. Waelkens, 151
- Young, K., Phillips, T. G., & Knapp, G. R. 1993, *ApJS*, 86, 517
- Zubko, V. G., Mennella, V., Colangeli, L., & Bussoletti, E. 1996, *MNRAS*, 282, 1321

Appendix A

HIPE & Python Scripts

A.1 Adapted PACS Pipeline

```
# 19 12 2011
# process level0 data to level1 step by step
# saves 'unedited' frames

if ("obs" in dir()) :
    obsid=obs
else :
    obsid=int(str(System.getProperty("SHELLCMD.OBS")))
if ("side" in dir()) :
    side=channel
else :
    side=str(System.getProperty("SHELLCMD.SIDE"))
if ("CTcorr" in dir()) :
    CTcorr=CTcorr
else :
    if (str(System.getProperty("SHELLCMD.CORR")) == "True") :
        CTcorr=True
    else :
        CTcorr=False

# fetch ObsData
obsCont = getObservation(obsid, poolLocation="/supp/mess/lstore/", verbose=
    True)

# HouseKeeping Data
hk = obsCont.level0.refs["HPPHK"].product.refs[0].product["HPPHKS"]

# Pointing Product
pointing = obsCont.auxiliary.refs["Pointing"].product

# Orbit Ephemeris
oem = obsCont.auxiliary.refs["OrbitEphemeris"].product
horizonsProduct = obsCont.auxiliary.horizons
timeCorr = obsCont.auxiliary.timeCorrelation

if side == 'green':
    if obsCont.meta['blue'].getString() == 'blue2':
        print 'green channel selected'
    else:
        print '>>> This obsid has no green channel <<<'
        obsCont = 0
```

```

elif side == 'blue':
    if obsCont.meta['blue'].getString() == 'blue1':
        print 'blue channel selected'
    else:
        print '>>> This obsid has no blue channel <<<'
        obsCont = 0
else:
    print 'red channel selected'

# load frames
if (side in ['blue', 'green']):
    frames = obsCont.level0.refs["HPPAVGB"].product.refs[0].product
else:
    frames = obsCont.level0.refs["HPPAVGR"].product.refs[0].product

calTree = getCalTree(time=frames.startDate)

frames = findBlocks(frames, calTree=calTree)
frames = detectCalibrationBlock(frames)
frames = removeCalBlocks(frames, useBbid=1)

frames = photFlagBadPixels(frames, calTree=calTree)
frames = photFlagSaturation(frames, calTree=calTree, hkdata=hk, check='full
    ')
frames = photConvDigit2Volts(frames, calTree=calTree)
frames = photAddNoisePerPixel(frames, method = "median", calTree=calTree)
frames = addUtc(frames, timeCorr)
frames = convertChopper2Angle(frames, calTree=calTree)

frames = photAddInstantPointing(frames, pointing, calTree=calTree,
    orbitEphem=oem, horizonsProduct=horizonsProduct)
# astrometry correction
deltaRA = 0
deltaDEC = 0
# UCAM old
if (obsid in [1342190307,1342190308]):
    deltaRA = 6.4467/3600.
    deltaDEC = 0.1311/3600.
# AQSGR old
if (obsid in [1342195702,1342195703]):
    deltaRA = 5.0099035434e-05
    deltaDEC = 0.000568000295893
# RZSGR old
if (obsid in [1342193532,1342193533]):
    deltaRA = -0.000496448174374
    deltaDEC = 0.000313943281277
# SSCT old
if (obsid in [1342219068,1342219069]):
    deltaRA = -0.000391466909662
    deltaDEC = 0.000730208317139
# STCAM old
if (obsid in [1342206044,1342206045]):
    deltaRA = 0.00337278055272
    deltaDEC = 0.000460594159421
# WOR1 old
if (obsid in [1342190965,1342190966]):

```

```

        deltaRA = 0.000230472851939
        deltaDEC = -0.000427566649436
    if (deltaRA or deltaDEC)!=0:
        frames["Status"]["RaArray"].data==deltaRA
        frames["Status"]["DecArray"].data==deltaDEC
        print 'coordinates shifted'

frames = photRespFlatfieldCorrection(frames, calTree=calTree)
System.gc()

frames = photAssignRaDec(frames, calTree=calTree)
frames = addQualityInformation(frames)

# mask additional bad pixels
if (side in ['blue', 'green']):
    b=frames.getMask("BADPIXELS")
    b[2,30,:]=1
    b[11,16:32,:]=1
    if obsid==1342204435:
        b[11,48:64,7681:9224]=1 # mask bad line in Betelgeuse obs.
    frames.setMask("BADPIXELS",b)

# mask columns affected by crosstalk
if CTcorr==1:
    frames = photMaskCrosstalk(frames)

    FitsArchive().save("/supp/mess/tmpframes/"+str(obsid) + "_" +side+
        _unedited_clean.fits",frames)
else:
    FitsArchive().save("/supp/mess/tmpframes/"+str(obsid) + "_" +side+
        _unedited.fits",frames)
System.gc()

```

A.2 Create a Radial Profile

```

execfile("/supp/mess/scripts/ellipse.py")
execfile("/supp/mess/scripts/ellipse_integrate.py")

def makeprofile(map, obj, channel, inner, outer, aspp, norm, spline, photo,
    bg, showplot):

    name=obj
    side=channel
    both=False
    aspp=aspp
    inner=inner/aspp # in pixels
    outer=outer/aspp
    sampling=aspp
    normalise=norm
    spline=spline

    photometry = photo
    bg = bg

    if both:
        side='blue'

```

```

map=map
d=Display (map)
xoff=0
yoff=0
fitbox=100/aspp
xcen=map.dimensions [1]/2
ycen=map.dimensions [0]/2

while fitbox*aspp<=125:
    try:
        parameters = sourceFitting (elongated=False , slope=False ,
            image=map,minX=xcen-fitbox /2,minY=ycen-fitbox /2,width=
            fitbox , height=fitbox )
        sf=1
        break
    except herchel.ia.toolbox.image.ImageTaskException:
        fitbox=fitbox*1.5
        print '>>> sourceFitting FAILED > increasing fitbox size ('
            +str(fitbox)+' pixels) <<<'
        sf=0

if sf:
    x0=parameters [1].data [1] + xoff
    y0=parameters [1].data [2] + yoff
else:
    x0=xcen
    y0=ycen
    print "
    _____"
    print "—— sourceFitting FAILED > using image center coordinates!
    ____"
    print "
    _____"

e=0
phi=0

tstart=0
tstop=360
incr=2500

alist=Double1d (range ((inner*sampling).__int__ (),(outer*sampling).
    __int__ ())/Double (sampling))

# compute profile
intlist=[]
stdvlist=[]
for a in alist:
    int = ellipse (map,y0,x0,a,e,phi,tstart,tstop,incr,display=False)
    intlist.append (int [0])
    stdvlist.append (int [1])

r=Double1d (alist)
r_e=0
if e!=0:
    r_e=r*SQRT (1-e**2)

```

```

i=Double1d(intlist)

# resample r to 1 arcsec
try:
    scalefactor=ROUND(Double1d([ABS(map.getWcs().getCdel1()*3600)]),2)
    [0]
except:
    scalefactor=1.
    print "no WCS found, setting value to",scalefactor
print '>>> image scale is '+ str(scalefactor) + ' arcsec/pix <<<'
rescale=False
if scalefactor!=1:
    r=scalefactor*r
    r_e=scalefactor*r_e
    rescale=True
    print 'rescaling x-axis to 1 arcsec'
# rescale flux
i=i/scalefactor**2

if normalise:
    if MIN(r)==0:
        peak=MAX(i)
    else:
        peak=parameters[1].data[0]
    i=i/Double(peak)

if showplot:
    pp=PlotXY(r,i)
    if e!=0:
        pp.addLayer(LayerXY(r_e,i))
    if spline:
        res=10
        cs=CubicSplineInterpolator(r,i,True)
        xdata=Double1d(range((MIN(r)*res)..int--(),(MAX(r)*res).
            ..int--()))/Double(res)
        kurve=cs(xdata)
        pp.removeLayer(0)
        pp.addLayer(LayerXY(xdata,kurve))
    if (rescale or scalefactor==1):
        scale=1

    if (round(scale) == 1):
        pp.xtitle='Distance [arcsec]'
        pp.ytitle='Flux [Jy/arcsec2]'
        if normalise:
            pp.ytitle='normalised flux'
    else:
        pp.xtitle='Distance [pixels]'
        pp.ytitle='Flux [Jy/pix]'
        if normalise:
            pp.ytitle='normalised flux'

pp.style.stroke=0.5
norm=''
if normalise:
    norm=' | normalised'

```

```

wl='70$\micro$'
if side=='red':
    wl='160$\micro$'
pp.titleText=name+' | '+str(wl)+norm
if both:
    side='red'

map2=fitsReader( file='/supp/mess/results/'+name+'_'+name+'_'+side+'_scanam.fits')

if side=='red':
    fitbox=50
else:
    fitbox=100
xcen=map2.dimensions[1]/2
ycen=map2.dimensions[0]/2
parameters2 = sourceFitting( elongated=False, slope=False, image=
    map2, minX=xcen-fitbox/2, minY=ycen-fitbox/2, width=fitbox,
    height=fitbox)

x0=parameters2[1].data[1] + xoff
y0=parameters2[1].data[2] + yoff

alist2=Double1d( range( (inner/2.*sampling).__int__(), (outer/2.*
    sampling).__int__() ) / Double(sampling)

# compute profile
intlist2=[]
stdvlist2=[]
for a in alist2:
    int = ellipse( map2, y0, x0, a, e, phi, tstart, tstop, incr, display=
        False)
    intlist2.append( int[0])
    stdvlist2.append( int[1])

r2=Double1d( alist2)
r_e2=0
if e!=0:
    r_e2=r2*SQRT(1-e**2)
i2=Double1d( intlist2)

# resample r to 1 arcsec
scalefactor=round( map2["image"].meta["cdelt2"].getDouble()
    *3600,4)
print '>>> image scale is '+ str(scalefactor) + ' arcsec/pix
<<<<'
rescale=False
if scalefactor!=1:
    r2=scalefactor*r2
    r_e2=scalefactor*r_e2
    rescale=True
    print 'rescaling x-axis to 1 arcsec'
# rescale flux
i2=i2/scalefactor**2

if normalise:

```

```

        if MIN(r2)==0:
            peak2=MAX(i2)
        else:
            peak2=parameters2 [1]. data [0]
            i2=i2/Double(peak2)
    pp.addLayer(LayerXY(r2 , i2))
    col=pp.getLayerXY(1).getStyle().setColor(java.awt.Color
        (255,0,0))
    pp.getLayerXY(1).setStyle(col)
    if e!=0:
        pp.addLayer(LayerXY(r_e2 , i2))
    if spline:
        res=10
        cs=CubicSplineInterpolator(r2 , i2 , True)
        xdata=Double1d(range((MIN(r)*res) ..int..() ,(MAX(r)*res).
            ..int..()))/Double(res)
        kurve=cs(xdata)
        pp.removeLayer(1)
        pp.addLayer(LayerXY(xdata , kurve))
        col1=pp.getLayerXY(0).getStyle().setColor(java.awt.Color
            (0,0,255))
        col2=pp.getLayerXY(1).getStyle().setColor(java.awt.Color
            (255,0,0))
        pp.getLayerXY(0).setStyle(col1)
        pp.getLayerXY(1).setStyle(col2)
    pp.titleText=name+norm
    pp.legend.setPosition(pp.legend.getPosition().TOPCENTER)
    pp[0].setName('70$\micro$')
    pp[1].setName('160$\micro$')
    pp.legend.visible=1

# integrate brightness
if photometry:
    totalandavg=ellipse_int(map,y0,x0,alist ,e,phi ,tstart ,tstop ,incr ,bg ,
        display=False)      #X & Y switched
else:
    totalandavg="NO PHOTOMETRY"

return([pp,r,i ,totalandavg])

# elliptical brightness profile
from java.lang.Math import *
def ellipse(map,x0,y0,a,e,phi ,tstart ,tstop ,incr ,display):
    def frange(start ,stop ,step):
        a=start
        l=[]
        while a<=stop:
            l.append(a)
            a+=step
        return(l)

    b=a*SQRT(1-e**2)
    psi=270-phi

```

```

step=PI/incr

tstart_rad=tstart*PI/180
tstop_rad=tstop*PI/180

t=frange(tstart_rad , tstop_rad , step)

xx=[]
yy=[]

for i in t:
    x=x0+a*cos(i)*cos(psi*PI/180)-b*sin(i)*sin(psi*PI/180)
    y=y0+a*cos(i)*sin(psi*PI/180)+b*sin(i)*cos(psi*PI/180)
    xx.append(x)
    yy.append(y)

xx=Double1d(xx)
yy=Double1d(yy)

xx=Int1d(ROUND(xx))
yy=Int1d(ROUND(yy))
im=map.getImage().copy()

intens=[]

if display:
    mapcopy=map.copy()
    overlay=mapcopy.getImage()
    for i in range(len(xx)):
        overlay[xx[i],yy[i]]=1
    d=Display(mapcopy)

for i in range(len(xx)):
    intens.append(im[xx[i],yy[i]])

avg=MEAN(intens)
stdv=STDDEV(intens)
return(avg , stdv)

```

A.3 Compare DUSTY Model to Observation

```

#compare model to observation
import os
import math
import numpy as np
import scipy
import pyfits
import matplotlib.pyplot as plt
execfile('azAv.py')
execfile('compare2d.py')

#open norm. PSF
psffits=pyfits.open('superpsf.fits')
psf=psffits[1].data

#open object

```

```

objfits=pyfits.open('/home/mess/mecina/TTCYG/TTCYG2_blue_scanam_v10_clean.
fits')
obj=objfits[1].data
xcen_obs=672.601
ycen_obs=649.962

#make object profile
r_nr,r_obs,i_obs=azimuthalAverage(obj,center=np.array([xcen_obs,ycen_obs]),
return_nr=True)

#object parameters
dist=390 #distance in parsec
Fobs=2.52e-10
Lsun=6300

#model list
moddirectory='/home/mess/mecina/DUSTY/ttmods/img/'
modlist=os.listdir(moddirectory)
modnr=len(modlist)
fitness=[]
mo=[]

# profile comparison range
bs=0.5
inner=0/bs
outer=100/bs

scaling=2
if scaling==1:
    save=open(moddirectory+'fitresults_scaling1','w')
elif scaling==2:
    save=open(moddirectory+'fitresults_scaling2','w')

r_reg,i_reg,scale=compare2d(modlist[0],moddirectory,scaling=scaling,imres
=2.,binsize=bs)
i_new=np.interp(r_reg,r_obs,i_obs)
r_obs=r_reg
i_obs=i_new
r_nr=r_obs**2*np.pi*(130./360.)
r_nr[r_nr==0]=1.

r_obs=r_obs[inner:outer]
i_obs=i_obs[inner:outer]
r_nr=r_nr[inner:outer]

count=1
for name in modlist:
    print name
    try:
        r_mod,i_mod,scale=compare2d(name,moddirectory,scaling=
scaling,imres=1.,binsize=bs)
        r_mod=r_mod[inner:outer]
        i_mod=i_mod[inner:outer]
        err=np.sum(((i_mod-i_obs)**2)/(r_nr**(-0.5)))
        mo.append(name)

```

```

        fitness.append(err)
    except:
        mo.append(name)
        err='ERR'
        fitness.append(err)
        scale='ERR'
    print count, ' of ', modnr, ' models compared'
    count+=1
    save.write(str(name)+' '+str(err)+' '+str(scale)+'\n')
    show=1
    if (name=='tt-det-2,1-51,2.i001.jy') and show==1:
        plt.semilogy(r_mod,i_mod,'g-')
        plt.show()
save.close()
print ' > > > DONE < < < '

def compare2d(name, moddirectory, scaling=2, imres=1., binsize=0.5):
    #read model output
    r,i=np.loadtxt(moddirectory+name,unpack=True)
    parameterfile=moddirectory[:-4]+name[:-7]+"out"
    #
    g=open(parameterfile)
    parameters=g.readlines()
    g.close()
    # get angular diameter theta or inner radius
    index=parameters.index('=====\n')+float(
        name[-6:-3])._int_()
    #scale1
    theta=float(parameters[index].split()[5])
    scale1=theta*0.5*((Fobs/1e-6)**0.5)
    #scale2
    r1=float(parameters[index].split()[3]) # inner radius r1
        in cm
    scale2 = np.arctan((r1*(Lsun/1e4)**0.5)/(dist*3.08568025e18))
        *180*3600/math.pi
    #
    if scaling==1:
        scale=scale1
    elif scaling==2:
        scale=scale2
    print " scale is "+str(scale)
    r*=scale
    iscale=(r[1]/imres)**2*math.pi
    #
    #interpolate 1d profile
    rr=np.array(range(300*10))/10.
    ii=np.interp(rr,r,i)
    ii[0]*=iscale
    #
    #make 2d img
    dim=300
    y,x=np.mgrid[0:dim,0:dim]
    xcen=(len(x))/2.
    ycen=(len(y))/2.
    z=np.sqrt((x-xcen)**2+(y-ycen)**2)
    #

```

```

zf=np.floor(z*10)
zf=np.array(zf,dtype=int)
zdelt=z*10-zf
#
tab=ii[zf]+(ii[zf+1]-ii[zf])*zdelt
#convolution
fpsf=np.fft.fft2(psf)
ftab=np.fft.fft2(tab)
#
convc=np.fft.ifft2(ftab*fpsf)
convc_shift=np.fft.ifftshift(convc)
conv=convc_shift.real
#make profile
r_conv,i_conv=azimuthalAverage(conv,returnradii=True,center=(xcen,
ycen))
return r_conv,i_conv,scale

```


Curriculum Vitae

Personal Details

Name Marko Mečina
Address Zennerstraße 14/3/18, 1140 Vienna, Austria
E-mail marko.mecina@univie.ac.at
Date & place of birth August 7, 1985 in Klagenfurt, Carinthia

Education

1996–2004 BG/BRG für Slowenen in Klagenfurt
2009 Bachelor’s Degree in Astronomy at the University of Vienna
“Eigenschaften und Anwendung astronomischer Instrumente:
DSS-7 Spektrograph”

2004–2005 military service

Publications

Kerschbaum, F., Ladjal, D., Ottensamer, R., et al. 2010, A&A, 518, L140
Mayer, A., Jorissen, A., Kerschbaum, F., et al. 2011, Why Galaxies Care about AGB Stars II, ASPCS, 445, 351
Mecina, M., Kerschbaum, F., Ladjal, D., et al. 2011, Why Galaxies Care about AGB Stars II, ASPCS, 445, 353
Kerschbaum, F., Mecina, M., Ottensamer, R., et al. 2011, Why Galaxies Care about AGB Stars II, ASPCS, 445, 589
Ottensamer, R., Luntzer, A., Mecina, M., et al. 2011, Why Galaxies Care about AGB Stars II, ASPCS, 445, 625
Cox, N. L. J., Kerschbaum, F., van Marle, A.-J., et al. 2012, A&A, 537, A35

Conferences

2010 “Why Galaxies Care About AGB Stars II”, Vienna, Austria
2011 “Physical and Chemical Aspects of Late Stages of Stellar Evolution”, Warsaw, Poland

Danksagung / Zahvala

Mein Dank gilt meinem Betreuer, Ao. Univ. Prof. Dr. Franz Kerschbaum, für die Anregungen und Ratschläge während des Verfassens dieser Arbeit, speziell aber auch für die Möglichkeit diese auf aktuellen Forschungsergebnissen aufzubauen. Besonders bedanken möchte ich mich auch bei Herrn Dr. Roland Ottensamer, der, vor allem in technischen Fragen, stets unterstützend zur Seite stand.

Posebno hvaležen sem mojima staršema, za vso podporo, ki sta mi jo dala na dosedanji življenski poti. Vajina pomoč mi je omogočila prijeten potek študija. Prisrčna hvala!